

**INTERFACIAL CHEMISTRY OF WATER
AT THE IONIC LIQUID – VAPOR
INTERFACE PROBED BY AMBIENT
PRESSURE X-RAY PHOTOELECTRON SPECTROSCOPY**

by

Alicia M. Broderick

A dissertation submitted to the Faculty of the University of Delaware in partial fulfillment of the requirements for the degree of Doctor of Philosophy in Chemistry and Biochemistry.

Summer 2018

© 2018 Alicia M. Broderick
All Rights Reserved

**INTERFACIAL CHEMISTRY OF WATER
AT THE IONIC LIQUID – VAPOR
INTERFACE PROBED BY AMBIENT
PRESSURE X-RAY PHOTOELECTRON SPECTROSCOPY**

by

Alicia M. Broderick

Approved: _____
Brian Bahnson, Ph.D.
Chair of the Department of Chemistry and Biochemistry

Approved: _____
George Watson, Ph.D.
Dean of the College of Arts and Sciences

Approved: _____
Douglas J. Doren, Ph.D.
Interim Vice Provost for Graduate and Professional Education

I certify that I have read this dissertation and that in my opinion it meets the academic and professional standard required by the University as a dissertation for the degree of Doctor of Philosophy.

Signed:

John T. Newberg, Ph.D.
Professor in charge of dissertation

I certify that I have read this dissertation and that in my opinion it meets the academic and professional standard required by the University as a dissertation for the degree of Doctor of Philosophy.

Signed:

Karl Booksh, Ph.D.
Member of dissertation committee

I certify that I have read this dissertation and that in my opinion it meets the academic and professional standard required by the University as a dissertation for the degree of Doctor of Philosophy.

Signed:

Murray Johnston, Ph.D.
Member of dissertation committee

I certify that I have read this dissertation and that in my opinion it meets the academic and professional standard required by the University as a dissertation for the degree of Doctor of Philosophy.

Signed:

Chaoying Ni, Ph.D.
Member of dissertation committee

ACKNOWLEDGMENTS

I would like to thank my family and friends for their love and support throughout the years. I have had friends far and near provide encouragement and well wishes that have helped me continue towards my dreams. The conversations and visits from our large family has made the years go by fast. While there are too many of you to name, I will always appreciate the things you have done for me through my life.

I'd like to thank my advisor, John T. Newberg, for providing me with funding, endless opportunities to attend conferences all over the country, and the ability to conduct experiments at multiple synchrotrons. Your knowledge as helped me grow into the scientist I am today. I would also like to thank my group members for helping me get through the long hours and stressful times. Your humor and endless conversations have made a difference through the years. I can not forget about the lifetime friends I have made at the University of Delaware. The countless nights of grading and studying for our classes will never be forgotten. I will miss our trips to main street, especially happy hour at Margaritas.

A special thank you to my grandparents, Jim and Marie McGuire. You have taught me to never give up on my dreams and that a little hard-work and dedication can go a long way. Thank you for helping me grade lab reports and problem sets during the beginning of my studies and listening to me practice my talks towards the end. I am so grateful for the times you two took the drive to visit us at Delaware and then opening your doors to us for several years. You two will forever be our favorite roommates.

I'd finally like to thank my husband, Paul Broderick. We have been through so much over the years. I can not believe we were married, bought our first home, and had our first baby all within the last five years. You have encouraged me to never give up and have been very patience through this unexpected journey. I will cherish our memories in our first apartment in Delaware. We always made the best dinners. I will also never forget the sacrifices you made, from changing jobs to moving back home. I will always cherish our long commute together during my last three years. We never had a dull car ride from crazy drivers on the road to the weird conversations. I truly believe you are the reason I was able to get through! I love the life we have built together and look forward to a lifetime of love with you. To my son, Paul Jr., I hope your worries stay small and your dreams stay big. You have the most amazing family that will do everything to help you succeed in life. You are the real reason we have accomplished all that we have and will.

TABLE OF CONTENTS

LIST OF TABLES	ix
LIST OF FIGURES	x
ABSTRACT	xvi

Chapter

1	AMBIENT PRESSURE X-RAY PHOTOELECTRON SPECTROSCOPY.....	1
1.1	Introduction	1
1.2	Lab-based AP-XPS System.....	8
1.3	Sample to Aperture Distance.....	11
1.4	Angle-Resolved XPS of an Ionic Liquid.....	14
1.5	Mass Spectrometer on Different Stages	24
2	WATER AT IONIC LIQUID INTERFACES	30
2.1	Water at Ionic Liquid Interfaces.....	30
2.1.1	Introduction	30
2.1.2	Ionic Liquid-Vacuum Interface	32
2.1.3	Ionic Liquid-Gas Interface	36
2.1.4	Ionic Liquid-Solid Interface	39
2.1.5	Molecular Dynamic Simulation Studies of IL Interfaces.....	42
2.1.6	Summary and Future Outlook	44
2.2	Interfacial Water Uptake at the Ionic Liquid-Gas Interface of 1-Butyl-3-Methylimidazolium Acetate.....	48
2.2.1	Introduction	48
2.2.2	Experimental Details	49
2.2.3	Quantitative Assessment of Interfacial Water Uptake	51
2.2.4	Binding Energy Shifts Due to Interfacial Water Sorption.....	57
2.2.5	Growth in Carbon Species due to Interfacial Water Sorption.....	62
2.2.6	Kinetics of Interfacial Versus Bulk Water Sorption.....	65

2.3	Interfacial Water Uptake at the Ionic Liquid-Gas Interface of 1-Ethyl-3-Methylimidazolium Borofluorate	68
2.3.1	Experimental Details	68
2.3.2	High Resolution XPS Characterization Prior to Water Exposure	69
2.3.3	Quantitative Assessment of Interfacial Water Uptake	71
3	ENERGETICS OF INTERFACIAL WATER INTO ILS.....	75
3.1	Introduction	75
3.2	Experimental.....	77
3.3	Energetics of Water Sorption at the 1-Butyl-3-Methylimidazolium Acetate-Gas Interface	81
3.3.1	Relative Humidity Dependent Interfacial Water Uptake	81
3.3.2	Water Induced Changes in the Electronic Environment	86
3.3.3	Water Induced Structural Changes	89
3.3.4	Energetics of Interfacial Water Uptake	92
3.3.5	Interfacial Versus Bulk Energetics of Water Sorption	94
3.4	Energetics of Water at the 1-Butyl-3-Methylimidazolium Chloride-Gas Interface.....	107
4	DELIQUESCENT OF IONIC LIQUIDS	114
4.1	Introduction	114
4.2	Deliquescence using Lab Air and Salt Solutions	116
4.2.1	Experimental Details	116
4.2.2	Qualitative Assessment of IL Deliquescence	118
4.3	Deliquescence of 1-Butyl-3-Methylimidazolium Chloride via AP-XPS.....	121
4.3.1	Experimental.....	121
4.3.2	Isotherm of Interfacial Water Sorption.....	123
4.3.3	Chemical Shifts due to Charge Dissipation.....	130
4.3.4	Chemical Shifts due to Interfacial Water Sorption.....	132
4.3.5	Changes in the C 1s Spectra	136
5	SUMMARY AND FUTURE OUTLOOK.....	140
	REFERENCES	146

Appendix

A PERMISSION FOR JOURNAL ARTICLE REPRINT..... 164

LIST OF TABLES

Table 1.1 Different Anode Materials used for X-ray Source	4
Table 1.2: Ratios of IL Species at Different Collection Angles in the Presence of 0.8 Torr	22
Table 2.1. Experimental Studies Probing IL Interfaces in the Presence of Water	47
Table 2.2. Molecular Dynamics Studies of IL Interfaces in the Presence of Water	48
Table 3.1: Longevity of Each Gravimetric Data Point for Isotherm at 21.7 °C	95
Table 4.1: Ionic Liquid Deliquescence Summary	121

LIST OF FIGURES

- Figure 1.1: Diagram showing XPS analysis where x-rays (gray) penetrate a sample exciting a core level electron (blue) with some kinetic energy that is measured by the detector. 2
- Figure 1.2: XPS survey spectrum of 1-ethyl-imidazoilium acetate collected at 8.9×10^{-8} Torr showing the peaks of C 1s, N 1s, O 1s, and F 1s. 5
- Figure 1.3: High resolution C 1s spectrum of [C₂mim][Ace] collected at 8.9×10^{-8} Torr 6
- Figure 1.4: Diagram showing AP-XPS analysis where sample is in a high pressure zone (red) while the x-ray source and detector are still under high vacuum with use of a window and small aperture, respectively. 7
- Figure 1.5: Lab-based AP-XPS system showing key components as well as different pumping stages from high pressure stage up to 4th pumping stage. 10
- Figure 1.6: High resolution Ag 3d collected in acceleration collection mode and picture of sample on sample holder prior to pump down. 11
- Figure 1.7: Sample analysis geometry indicating the X-ray illumination spot (brown) and XPS analysis spot size (green). The z-axis is the energy axis of the analyzer, d is the closest sample-to-aperture distance, and N is the sample normal with the X-rays at 55° and analyzer at 20° 12
- Figure 1.8: Normalized Ag 3d(5/2) area as a function of sample-to-aperture distance (d) for all three analyzer modes under vacuum. The maximum area for each mode is normalized to 1.0 and an offset of 0.3 is used for clarity. 14
- Figure 1.9: Three types of experimental set-ups where spectra are collected in angular mode (a), spectra are collected in acceleration mode while tilting the sample (b) and spectra are collected in acceleration mode on a bent foil while tilting the sample (c). 15
- Figure 1.10: O 1s spectra at a water vapor pressure of 0.8 Torr using angular collection mode. 16

Figure 1.11: Pictures taken of sample while changing the collection angle in acceleration collection mode. The key components ratios at each angle are also shown.	17
Figure 1.12: AP-XPS spectra for O 1s (a), C 1s (b), and N 1s (c) at 1.0 Torr of water vapor and two angles: $\Theta = 20^\circ$ (orange) and 35° (blue).....	19
Figure 1.13: Experimental set-up of bent foil on sample holding, showing the capability to collect angle resolved XPS data at $\Theta \sim 56^\circ$	20
Figure 1.14: Images of the sampling position in the AP-XPS chamber where the aperture is position at the tip of the Au foil at a collection angle of $\Theta = 56^\circ$ (a) and the same collection position captured through a window on the AP-XPS chamber (b).....	21
Figure 1.15: XPS spectrum comparing data collected at $\Theta = 20^\circ$ (orange) and $\Theta = 64^\circ$ for O 1s (a), C 1s (b), and N 1s (c).	23
Figure 1.16: Schematic of the different pumping stages of our lab-based AP-XPS system and the two M/S positions explored.....	25
Figure 1.17: Mass spectrometer signal as a function of water vapor exposure while mass spectrometer is on Stage 0.....	26
Figure 1.18: The mass spectrometer pressure at Position #1 as a function of water vapor pressure at Stage 0.....	27
Figure 1.19: Mass spectrometer signal as a function of water vapor exposure while mass spectrometer is on Stage 2.....	28
Figure 1.20: The mass spectrometer pressure at Position #2 as a function of water vapor pressure at Stage 0.....	28
Figure 2.1: Three different interfaces of interest including ionic liquid -vacuum (a), ionic liquid-gas (b), and ionic liquid-solid (c).	31
Figure 2.2: Survey spectrum (a) of [C ₄ mim][Ace] along with chemical structure. Initial [C ₄ mim][Ace] spectra in the (b) O 1s, (c) N 1s and (d) C 1s regions. Colors of peak fits correspond to elemental species in IL chemical structure.....	52
Figure 2.3: Spectra of C 1s (left) and N 1s (right) from 1.2×10^{-7} to 5.0 Torr. Spectral attenuation is apparent after 0.01 Torr, which is where water vapor and interfacial water is seen in the O1s spectrum.	54

Figure 2.4: O 1s AP-XPS spectra as a function of increasing water vapor pressure. Top spectra taken shortly after water vapor pumped out of the chamber.	55
Figure 2.5: AP-XPS isotherm of water mole fraction (x_w) at the IL-vapor interface with water vapor pressure on a log scale (green) and linear scale (black).....	57
Figure 2.6: Relative binding energy shifts (ΔBE) referenced to the C_{alkyl} BE as a function of (a) water vapor pressure and (b) water mole fraction.	59
Figure 2.7: Ratio of C_{alkyl} to total C 1s XPS intensity as a function of the number of waters per IL pair (n_w/n_{IL} ; black data) and water mole fraction (x_w ; blue data).	63
Figure 2.8: Two O 1s spectra collected consecutively at 0.4 Torr are shown in black and orange, respectively.	66
Figure 2.9: Gravimetric analysis of water absorption showing x_w (black) and water vapor pressure (green) as a function of time.	67
Figure 2.10: Survey spectrum of $[C_2mim][BF_4]$ collected at 2.1×10^{-8} Torr along with chemical structure.	70
Figure 2.11: High resolution spectra of C 1s (a), N 1s (b), F 1s (c), and B 1s (d) for $[C_2mim][BF_4]$	71
Figure 2.12: AP-XPS isotherm of water mole fraction (x_w) at the IL-vapor interface with water vapor pressure for $[C_4mim][Ace]$ (blue) and $[C_2mim][BF_4]$ (red).	73
Figure 3.1: Images of $[C_4mim][Ace]$ (a) and $[C_4mim][Cl]$ (b) deposited on Au foil in the AP-XPS chamber under vacuum conditions at 10 °C prior to water exposure.....	78
Figure 3.2: O 1s at (a) vacuum and (b) 2.5 Torr from 0-42 °C, where O_{gas} and O_w shift to higher binding energy as a function of decreasing temperature. Inset shows zoomed-in spectra collected at 5.0 Torr from 10-42 °C. Color Code: purple - 42 °C, green - 32 °C, blue - 22 °C, red - 10 °C, and black - 0 °C.....	82
Figure 3.3: Isotherms from 0 - 42 °C of water uptake into $[C_4mim][Ace]$ as a function of pressure (a) and relative humidity (b).....	84

Figure 3.4:	Binding energy shifts relative to C _{alkyl} for all components as a function of pressure at 0 °C (closed circles) and 42 °C (open circles). All components follow same shifting trend at both temperatures.....	87
Figure 3.5:	Binding energy shift relative to C _{alkyl} for all components and temperature. Color Code: blue=O _w , green=C _{ox} , black=O _{Ac} , red=C _{ring} , gray=N _{ring} ; Symbol Code: diamond= 0 °C, triangle= 10 °C, circle= 22 °C, square= 32 °C, square with cross= 42 °C.	88
Figure 3.6:	C 1s at (a) vacuum and (b) 2.5 Torr from 0 - 42 °C, normalized to C _{ring} component and calibrated to C _{alkyl} at 285 eV. Color Code: purple – 42 °C, green – 32 °C, blue – 22 °C, red – 10 °C, and black – 0 °C.	89
Figure 3.7:	Ratio of C _{alkyl} intensity to total C 1s intensity as a function of water mole fraction (x _w) for each isotherm.....	91
Figure 3.8:	Enthalpy of interfacial water uptake from 0.4 < x _w < 0.75.	94
Figure 3.9:	Isotherm of bulk water uptake into [C ₄ mim][Ace] using gravimetric analysis on a linear scale (a) and log scale (b).	97
Figure 3.10:	Relative humidity plot of water uptake into the interfacial region (circles) and bulk region (crosses).....	98
Figure 3.11:	Clausius-Clapeyron relation plots from 0.4 < x _w < 0.75 for both the interfacial (a) and bulk (b) regions.	102
Figure 3.12:	Entropy plots from 0.4 < x _w < 0.75 for both the interfacial (a) and bulk (b) regions.....	103
Figure 3.13:	The enthalpy (a) and entropy (b) of water uptake from 0.4 < x _w < 0.75 for both the interfacial and bulk regions. Dashed line represent the enthalpy (a) and entropy (b) of vaporization for bulk water at 25 °C. Error bars represent 1σ.	104
Figure 3.14:	Gibbs Free Energy (ΔG°) of water sorption into [C ₄ mim][Ace] at both the interfacial (black) and bulk (gray) regions at 20 °C. Error bars represent 1σ.	106
Figure 3.15:	Isotherm of bulk water uptake into [C ₄ mim][Cl] using AP-XPS on a linear scale (a) and log scale (b).	109
Figure 3.16:	Water mole fraction vs. relative humidity (%) plot for all four isotherms showing one uptake curve.....	110

Figure 3.17: The enthalpy (a) and entropy (c) of water uptake from $0.4 < x_w < 0.60$ for [C ₄ mim][Cl] using AP-XPS. The dashed line represent the enthalpy (a) of vaporization for bulk water at 25 °C. Error bars represent 1σ.	111
Figure 3.18: Clausius-Clapeyron relation (a) and entropy (b) plots from $0.4 < x_w < 0.6$ for interfacial water uptake into [C ₄ mim][Cl].	112
Figure 3.19: Gibbs Free Energy (ΔG°) of water sorption into [C ₄ mim][Cl] at the interfacial region at 20 °C. Error bars represent 1σ.	113
Figure 4.1: Deliquescence process of NaCl where initial water vapor adsorption occurs on the solid-gas interface and then over time will be absorbed to form an aqueous salt solution.	114
Figure 4.2: Experimental set-up for studying the deliquescence of ionic liquids with saturated salt solutions in a closed container (b) and in lab air (a).	117
Figure 4.3: Images of deliquescence of [MP][Ace] versus time (sec) using a saturated solution of potassium iodide (RH = 69%) captured via light microscope.	119
Figure 4.4: Images of deliquescence of [MA] ₂ [Mal] versus time (min) under lab air (RH = 48%) captured via light microscope.	120
Figure 4.5: Images captured when [C ₄ mim][Cl] was first pumped down in AP-XPS chamber at 22 °C (a) and after pumping in AP-XPS chamber overnight at -5 °C (b).	123
Figure 4.6: Survey spectrum of solid [C ₄ mim][Cl] collected at -5.0 °C and 4.5×10^{-8} Torr along with the chemical structure.	124
Figure 4.7: [C ₄ mim][Cl] high resolution spectra of C 1s (a), N 1s (b), and Cl 2p (c).	125
Figure 4.8: Isotherm of water uptake into [C ₄ mim][Cl] quantifying the initial O 1s spectrum (red) and the final O 1s spectrum (blue) at -5 °C.	126
Figure 4.9: Images captured of [C ₄ mim][Cl] -water system as a solid in the lab-based AP-XPS at 0.25 Torr (a) and liquid at 0.50 Torr (b).	128
Figure 4.10: Vacuum O 1s spectrum before water exposure (gray) and after water exposure (black) of [C ₄ mim][Cl] at -5 °C.	129

Figure 4.11: C 1s spectra of [C ₄ mim][Cl] showing chemical shift in the presence of water due to charge compensation.	130
Figure 4.12: Binding energy shifts (Δ BE) relative to high vacuum spectrum of [C ₄ mim][Cl] as a function of water vapor pressure.	131
Figure 4.13: Cl 2p spectrum of [C ₄ mim][Cl] showing chemical shift due to interfacial water uptake.	133
Figure 4.14: Binding energy shifts (Δ BE) of species in [C ₄ mim][Cl] relative to the spectrum collected at 0.25 Torr as a function of water vapor pressure.	134
Figure 4.15: C 1s spectrum of [C ₄ mim][Cl] as a function of water vapor pressure. .	137
Figure 4.16: Ratio of C _{alkyl} /C _{Tot} as a function of n _w /n _{IL} for [C ₄ mim][Cl].	138

ABSTRACT

Ionic liquids (ILs) are molten salts that are highly hygroscopic, so they absorb water over time. The sorption of water into IL has been heavily studied for bulk absorption while very little data has been collected of surface sorption. It is believed the sorption into these two different regions of the IL will have different water interactions. Using ambient pressure X-ray photoelectron spectroscopy (AP-XPS), the interaction of water with multiple ionic liquids was studied. After installation of a lab-based AP-XPS and conducting experiments to show the capabilities of the system, studies of water with IL were conducted.

For the first time, AP-XPS was used to quantitatively assess the chemical changes of the top few nm of the ionic liquid (IL)-gas interface of 1-butyl-3-methylimidazolium acetate, [C₄mim][Ace], in the presence of water vapor at room temperature. Above 10⁻³ Torr the uptake of water into the interfacial region was observed and increases up to a maximum water mole fraction (x_w) of 0.85 at 5 Torr. Comparing AP-XPS to gravimetric analysis measurements, the kinetics of interfacial uptake are rapid compared to bulk water absorption. Increasing interfacial water gives rise to relative binding energy (Δ BE) shifts in O 1s, C 1s and N 1s regions which increase with x_w . The binding energy shifts are due to a change in electronic environment for specific moiety. For $x_w > 0.6$ there is a sudden increase in

hydrophobic C_{alkyl} signal at the IL-vapor interface. In light of recent small angle neutron scattering and molecular dynamic simulations, this observed increase in interfacial carbon is attributed to a water induced phase change that gives rise to nanometer sized, segregated polar and non-polar regions. This heterogeneous restructuring leads to an enhancement in hydrophobic nanostructures at the IL-vapor interface.

Both AP-XPS and gravimetric analysis were used to quantitatively assess the effect of temperature on the water uptake into 1-butyl-3-methylimidazolium acetate, [C₄mim][Ace], at the interfacial and bulk regions. It was found that water uptake into the interfacial and bulk increased with decreasing temperature or increasing relative humidity. Additionally, there is more water present in the interfacial region compared to bulk within $0.4 < x_w < 0.75$ at 0 - 42 °C. The thermodynamics [enthalpy (ΔH°), entropy (ΔS°), and Gibbs free energy (ΔG°)] of water sorption into both the interfacial and bulk region of [C₄mim][Ace] were determined. The ΔH° of water sorption into the ionic liquid (IL) at both interfaces approached the enthalpy of vaporization for bulk water as more water was introduced to the system. The ΔS° was similar at both interfaces at $x_w < 0.6$ and showed favorability within the interfacial region at $x_w > 0.6$. At 20 °C, concurrently the ΔG° was more favorable in the interfacial region. This implies there is a difference in water sorption at the interface and bulk regions, where an energy barrier is present for the water to travel from the interface to the bulk.

The deliquescence of a solid IL, [C₄mim][Cl], was studied using AP-XPS at -5 °C. The deliquescence point is between $7.9 < \%RH < 15.8$. At the maximum water vapor of 1.1 Torr, [C₄mim][Cl] has a maximum $x_w \sim 0.77$. Changes in the C 1s spectra as a function of water vapor pressure were also noted. The initial changes in the carbon spectra while the IL is a solid is believed to be due to carbon contamination desorbing from the surface. After the IL deliquesces, increases in the aliphatic carbon species may be due to restructuring of the interface where the hydrophilic carbon chain is at the surface and the hydrophilic species (anion, imidazolium ring, and water molecules) are clustered at the inner layer of the interfacial region. To confirm this restructuring, MD of the interface and/or depth profiling using a synchrotron AP-XPS system are needed.

Chapter 1

AMBIENT PRESSURE X-RAY PHOTOELECTRON SPECTROSCOPY

1.1 Introduction

X-ray photoelectron spectroscopy (XPS), also known as electron spectroscopy for chemical analysis (ESCA), is a powerful analytical tool that is widely used today due to its user-friendly instrumentation and easy data interpretation. This is a vacuum-based spectroscopy used to investigate the surface structure of various materials including inorganic compounds, semiconductors, polymers, and even liquids. It is a surface sensitive instrument that provides information about the sample's elemental composition, surface contaminations, and chemical and electronic state of the elements present in the interfacial region. XPS analysis is also a quantitative surface technique that provides an atomic level picture of the sample surface with a probing depth of several nanometers (nm).¹ XPS can detect every element with atomic number of 3 and above. The detection limit for this technique is in the parts per thousand range and operates in high vacuum (10^{-8} Torr) or ultrahigh vacuum (10^{-9} Torr).

The theory of XPS is based off of Einstein's photoelectric effect, which won the Nobel Prize in 1921.¹ In XPS, monochromatic X-rays irradiate the sample surface leading to the emission of core level photoelectrons (Figure 1.1). The kinetic energy (KE) of the emitted photoelectrons is measured and the binding energy (BE) of these core shell electrons are determined. Since the energy of the x-rays ($h\nu$) is known and the KE is measured, the BE of the emitted photoelectrons can be determined by the following equation:

$$KE = h\nu - BE - \phi \quad (\text{Eqn 1.1})$$

Where ϕ is the work function of the spectrometric used to measure the kinetic energy. The work function is different for every XPS instrument and is an adjustable correction factor that accounts for the change in KE given up by the emitted photoelectron as it is absorbed by the detector. In 1954, Kai Seighban and colleagues collected the first high resolution spectra of NaCl.¹ Soon after, Seighban and several engineers produced the first commercial monochromatic XPS instrument in 1969.² In 1981, Kai Seighban was recongized for his development of XPS with a nobel prize in 1981.¹ Since then, XPS has been established as a very useful analytical tool used in various applications including catalysis, semiconductors, and many other material science fields.

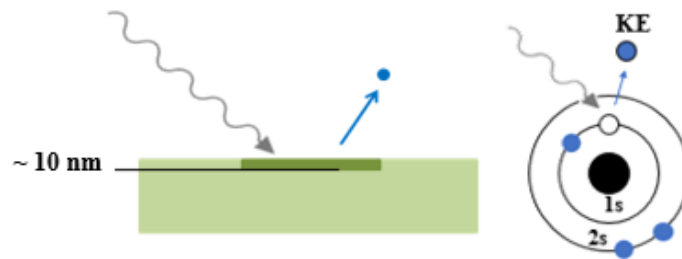


Figure 1.1: Diagram showing XPS analysis where x-rays (gray) penetrate a sample exciting a core level electron (blue) with some kinetic energy that is measured by the detector.

Today, XPS has been developed to included many state of the art measurements including imagining the surface of a sample, depth profiling, and angle-resolved (AR)-XPS. To image the sample surface, elemental mapping or parallel imaging can be used to look at surface chemistry, contaminations, and sample

thickness. In elemental mapping, the energy of the X-ray beam as well as the analysis position is fixed and images are generated using a two-dimensional rectangular array of XPS analysis.³ A faster approach with better resolution to imaging is called parallel imaging where the field of view is imaged entirely without scanning voltages.³ Depth profiling is also a popular sampling technique that provides information the subsurface layers of the sample as well as a quantitative analysis of layer thickness. In this technique, an ion beam is used to etch the surface of the sample, revealing the sublayers underneath. By performing cycles of etching following by XPS analysis, the layer thickness as well as composition can be determined. Depth profiling has also been used to remove surface contaminations, that are present in most samples.⁴ For a more nondestructive way to determine layer thickness as well as chemical state information, users utilize AR-XPS. In this technique, the sample is tilted at various angles and XPS spectra is acquired as a function of the sample angle. A steep sample angle, leads to a more surface sensitive analysis. More recently, XPS systems are equipped with a parallel collection mode, where XPS spectra can be collected over a range of 60° with resolution up to 1° without tilting the sample.³

Today, most XPS systems use monochromatic X-ray sources. To generate monochromatic X-rays, a metallic anode is bombarded with high energy electrons. The incident X-rays are then diffracted at a quartz crystal. With use multiple crystals with different curvature, the X-rays are focused on the sample. The two most common metallic anodes are Mg K α (photon energy = 1253.6 eV) and Al K α (1486.6 eV).⁵ However, metallic anodes including Zr L α (2042.4 eV), Ag L α (2984.3 eV), Ti K α (4510.9 eV), and Cr K α (5417 eV) have also been used.³ Different x-ray sources will provide different photon energies (as listed) and line widths as shown in Table 1.1.

Table 1.1 Different Anode Materials used for X-ray Source

Anode	Radiation	Photon Energy (ev)	Line Width (eV)
Mg	K α	1253.6	0.7
Al	K α	1486.6	0.85
Zr	L α	2042.4	1.6
Ag	L α	2984.3	2.6
Ti	K α	4510.9	2.0
Cr	K α	5417	2.1

X-ray induced beam damage of a sample is a major concern with XPS analysis and care should be taken to limit the amount of X-ray exposure on the sample.⁴ To do so, some XPS systems use a shutter to close off the direct line between the X-rays and sample when spectra is not collected. Other systems have an automatic shut off that turns the X-ray irradiation off at the end of XPS spectra collection. As an example, X-ray induced beam damage is apparent in the XPS spectra, where it's been shown as a secondary peak in the N 1s spectrum of an ionic liquid.⁶

XPS can collect two types of spectra including a qualitative survey spectrum over a large range of binding energies and a quantitative high-resolution spectrum of specific elements collected over several eVs. An example survey spectrum of 1-ethyl-3-methylimidazolium acetate, [C₂mim][Ace], collected at 8.9×10^{-8} Torr along with the chemical structure are shown in Figure 1.2. In the survey spectra, there are four elements present: C 1s, N 1s, O 1s, and F 1s. From the chemical structure, we can confirm that the F 1s peak is a contamination on the surface. A few characteristics can be noted in a survey spectrum. The first is the element that appears as a peak along with a small peak a few eV away due to emitted photoelectrons with energy loss (labelled energy loss). Also, at higher binding energy an O KLL Auger peak is seen. An X-ray induced Auger peak occurs when an electron from a higher orbital fills the

hole formed from an emitted photoelectron. This transition causes the ejection of an Auger electron.

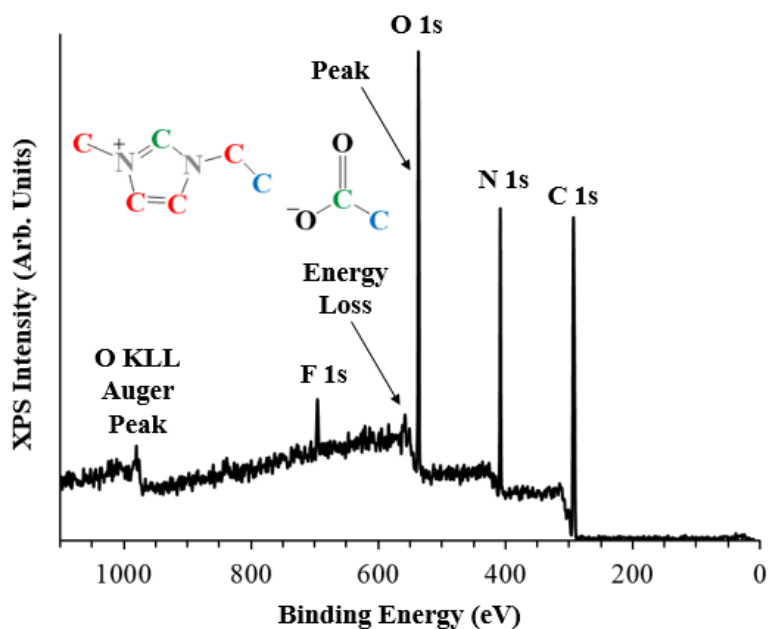


Figure 1.2: XPS survey spectrum of 1-ethyl-imidazoilium acetate collected at 8.9×10^{-8} Torr showing the peaks of C 1s, N 1s, O 1s, and F 1s.

After collecting a qualitative survey spectrum, high resolution spectra of all the elements is collected. An example high resolution spectra of the C 1s for [C₂mim][Ace] is shown in Figure 1.3. In this spectrum, there are three different components present that are color coded to match the chemical structure. The binding energy difference in the components is due to the electronic environment that each carbon species experiences. The more oxidized carbon species will shift to the higher binding energy (green), while the more reduced species (blue) will appear at lower binding energy.

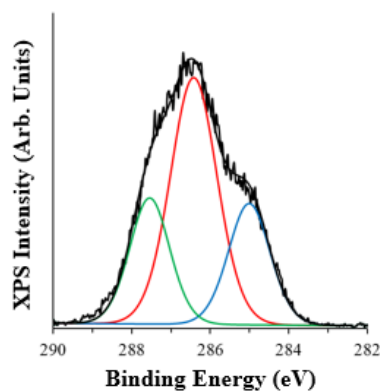


Figure 1.3: High resolution C 1s spectrum of [C₂mim][Ace] collected at 8.9×10^{-8} Torr

Traditional XPS is performed under high vacuum conditions; however, there has been a need to study more environmentally relevant systems. This desire led to the development of ambient pressure (AP) XPS, where up to Torr level gases are introduced into the sample chamber while simultaneously collecting XPS spectrum. In doing so, the components of the XPS system (X-rays and detector) still need to maintain high vacuum conditions while the sample is placed in a high-pressure regime. AP-XPS is now used in synchrotrons and laboratories around the world.

A diagram of an AP-XPS system is shown in Figure 1.4. The components required to perform traditional XPS are still shown (x-ray source and detector) and held under high vacuum conditions ($\sim 10^{-8}$ Torr). The sample is in a high-pressure region, where various gases (H₂O, N₂, H₂, O₂, etc) can be introduced up to Torr level. The X-ray source is held under high vacuum with use of a window that is transparent to X-rays and capable of holding a high vacuum on one side and high pressure on the other. Typical window types include silicon nitrile, aluminum, and graphene.⁷ The emitted photoelectrons travel through a small space of gas before reaching the

aperture, in hopes to limit the amount of collisions of electrons with gas molecules. Once reaching the aperture, these electrons are differential pumped up to the CCD detector, which is under high vacuum.

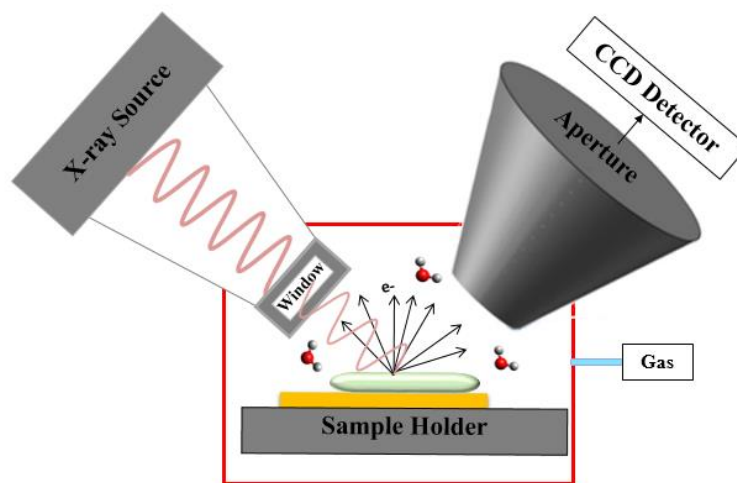


Figure 1.4: Diagram showing AP-XPS analysis where sample is in a high pressure zone (red) while the x-ray source and detector are still under high vacuum with use of a window and small aperture, respectively.

AP-XPS systems are utilized in synchrotrons around the world. In the United States, there are three synchrotron-based AP-XPS systems at the following facilities: National Synchrotron Light Source (Brookhaven, NY), Advanced Light Source (Berkeley, CA), and Stanford Synchrotron Radiation Light Source (Stanford, CA). The main advantages to synchrotron AP-XPS systems is the high intensity flux and tunable X-ray source.⁴ With a tunable X-ray source, depth profiling of the substrate can be done to show the different layers of the sample. The high intensity flux, which is orders of magnitude higher than a lab-based system, is also very useful for

collecting shorter data acquisition times, where a spectrum can be collected much faster than one using a lab-based system.² One must take care to watch for x-ray damage of the sample with such high flux.

Today, lab-based AP-XPS are growing in demand. Lab-based AP-XPS systems eliminate the need to apply for competitive beam time and travel. Although data collection is longer, lab-based system can provide quantitative assessments of surface gas interactions with different substrates. With a fixed x-ray source, lab-based systems utilize the ability to tilt the sample or collect data in angular mode to obtain depth profiling of the substrate. Lab-based systems have also collected data at a maximum gas pressure of 25 Torr.⁸ A comprehensive review of the advancements of lab-based AP-XPS system has recently been published by our group.⁷

In this chapter, the details of our lab-based AP-XPS system are described. In addition, the optimized distance between the sample and aperture is determined. In addition, results from an attempt at angle-resolved AP-XPS with an ionic liquid and water using the angular collection mode are provided. Finally, the effect of mass spectrometer position on the AP-XPS system and recommendations for proper position for optimal use is discussed. Some of this work has been recently published.¹³

1.2 Lab-based AP-XPS System

The lab-based AP-XPS system is a Scienta HIP-2, shown in Figure 1.5. The system uses eight oil free turbo pumps: one on the monochromator (X-ray source), one on Stage 0, two on Stage 1, two on Stage 2, 1 on Stage 3, and one on Stage 4 (Hemisphere). The turbo pumps are back by two dry scroll pumps with a base pressure of 1×10^{-3} Torr that are continuously purged with nitrogen. The gas line is plumbed with a dry scroll pump that is continuously purged with nitrogen. Seven pressure

gauges are monitored on one controller include the gas line, a cold cathode on the high pressure chamber, two ion gauges on the monochromator and Stage 3, two convection enhanced thermal gauges to measure the forline pressures of the scroll pumps. Absolute pressures $> 10^{-3}$ Torr in the high pressure chamber are measured by a capacitance manometer.

The sample sits in the high pressure zone at Stage 0. The sample sits horizontally relative to the floor with allows the study of solid as well as liquid samples. The sample can rotate $\sim 30^\circ$ relative to the sample normal with the most sensitive angle of 50° . This is a custom built exchangeable chamber. It also has several ports where different attachments (mass spectrometer, leak valves for gases, camera, and sputter gun) can be used. The high pressure zone, which can operate up to 20 Torr depending on the gas, is separated from the high vacuum X-ray source (base pressure of 1×10^{-9} Torr) with use of a silicon nitride window (Norcada). This window is 1.0 μm thick which allows for a pressure differential > 1 atm to high vacuum.

The monochromatic X-ray source is a Scienta MX650 consisting of a 200 W Al $K\alpha$ anode and an X-ray monochromator with seven toroidal α -quartz crystals arranged in a close-packed array on a 650 mm Rowland circle. The crystals are held at 55°C to ensure temperature variations in the lab does not affect the quartz crystal lattice spacing. X-ray exposure is minimized with use of a feedback loop incorporated in the SES XPS collection software. At the end of collection, the software will trigger the anode high voltage power supply to shut off while the electron source filament remains on.

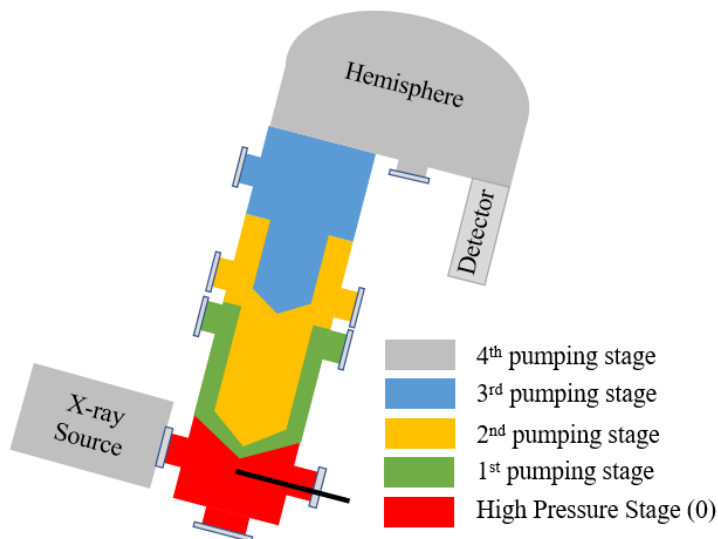


Figure 1.5: Lab-based AP-XPS system showing key components as well as different pumping stages from high pressure stage up to 4th pumping stage.

The analyzer (hemisphere) is equipped with nine interchangeable slits from 0.2 mm to 4 mm in the energy dispersive direction and operates at three pass energies: 50, 100, 200 eV. The MCP/CCD electron detector includes a 40 mm diameter MCP with phosphor plates and 70 frames per second camera. The analyzer can operate in three different collection modes: Angular, Transmission, and Acceleration. The angular collection mode can be used to perform angle-resolved XPS without rotating the sample. In this collection mode, the photoelectrons are emitted at different angles and then refocused onto different spots on the CCD detector.⁹ Transmission mode is the spatially resolving mode and the standard lens mode. Acceleration mode applies a bias right behind the first aperture in the first pumping stage which leads to higher electron collection.

1.3 Sample to Aperture Distance

Initial experiments were conducted on the lab-based AP-XPS system using Ag foil (Alfa Aesar, 99.998%, 0.25 mm thick). Prior to analysis, the silver foil was scraped with a black to exposure a fresh silver surface and eliminate any surface contaminations. For this experiment, the Ag 3d (5/2) peak at 368.3 eV was monitored.¹⁰ The data was fit using CasaXPS software. The silver 3d (5/2) was fit using a Shirley background with no other constraints. Shown in Figure 1.6 is the high-resolution Ag 3d (5/2) peak collected in acceleration mode along with a picture of the Ag foil on the sample holder prior to analysis.

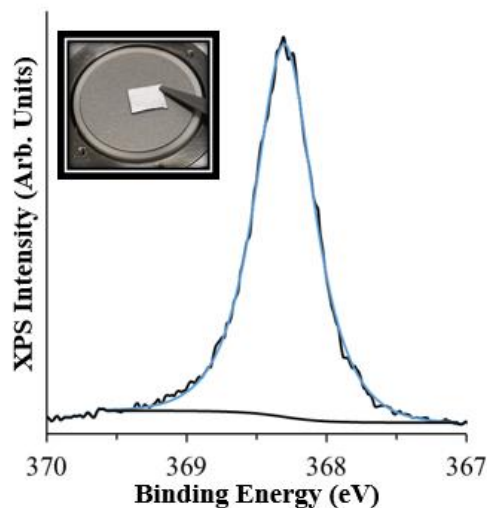


Figure 1.6: High resolution Ag 3d collected in acceleration collection mode and picture of sample on sample holder prior to pump down.

The sample holder is attached to a manipulator that can move in the x, y, and z direction shown in Figure 1.7. X-rays ($h\nu$) penetrate the sample surface at a 55° incidence and the aperture collects the emitted photoelectrons at 20° relative to the

sample normal. This system is equipped with a monochromatic X-ray source from VG Scienta (MX650) and it has been estimated that the X-ray irradiation spot size for this source is 3.8 x 1.4 mm. Initial experiments of system on our system have shown that the estimated electron capture spot size for this lab-based AP-XPS system is 0.9 ± 0.1 mm. A smaller spot size is expected due to the aperture and collection optics.

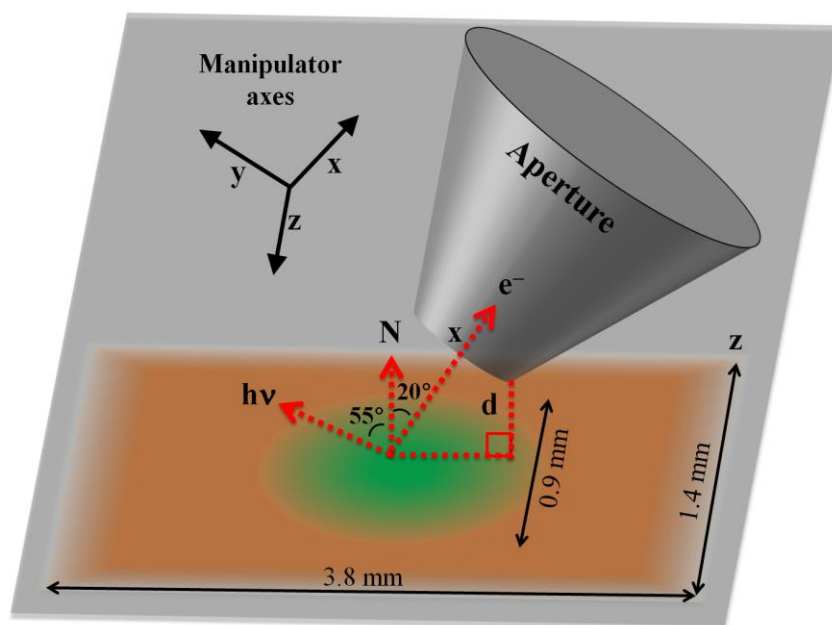


Figure 1.7: Sample analysis geometry indicating the X-ray illumination spot (brown) and XPS analysis spot size (green). The z-axis is the energy axis of the analyzer, d is the closest sample-to-aperture distance, and N is the sample normal with the X-rays at 55° and analyzer at 20°

To determine the optimized position of the sample relative to the aperture, experiments were conducted assessing the XPS intensity versus the sample-to-aperture distance (d) defined in Figure 1.7. At the beginning of the experiment the Ag foil was brought into contact with the aperture ($d = 0$), monitored using a camera mounted on

the analysis chamber. Throughout the experiment d was increased by moving the sample along the x-axis of the manipulator which moves along the spectrometer axis. Each micrometer measurement along the x-axis was then converted to $d = x \cos(20^\circ)$.

Figure 1.8 shows results of XPS peak area versus sample-to-aperture distance for angular (red), transmission (green) and acceleration (blue) modes. Because of the 20° tilt, counts were observed while the sample is in contact with the aperture at $d = 0$. For all three experiments XPS Ag 3d(5/2) areas are normalized to the maximum value and then offset for clarity. As the sample is moved away from the aperture the intensity initially increases, followed by a decrease as the sample moves away from the analyzer focal position. The data were fit to a second order polynomial with $R^2 > 0.992$ for all fits. The derivative gives maxima located at 570, 570, and 560 μm for angular, transmission and acceleration modes, respectively. These results show that all three collection modes have similar optimized positions for the sample-to-aperture distance.

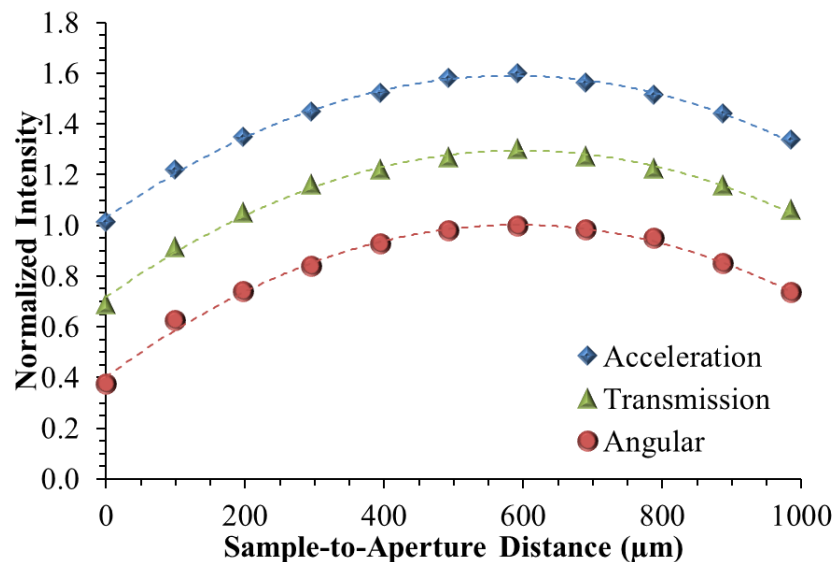


Figure 1.8: Normalized Ag 3d(5/2) area as a function of sample-to-aperture distance (d) for all three analyzer modes under vacuum. The maximum area for each mode is normalized to 1.0 and an offset of 0.3 is used for clarity.

This is an important measurement to obtain for all future experiments on our lab-based AP-XPS system. When working with solid samples, user may gently touch the aperture to the surface of the sample and then set distance to 560 μm . For liquid samples (ionic liquids), user can carefully approach the sample in the x direction about 50 μm at a time while monitoring the area counts of one of the elements present in the sample. When the area counts start to decrease, the user should retract the sample 5 μm and record the final area counts along with the x, y, and z coordinates.

1.4 Angle-Resolved XPS of an Ionic Liquid

Obtaining depth profile data for samples using our system was attempted and the results are shown below. With lab-based AP-XPS systems, depth profiling can be obtained by collecting data in angular mode or rotating the sample manipulator and

collecting XPS spectra in acceleration mode. Our sample manipulator has the ability to rotate $\Theta \sim 30^\circ$ relative to the sample normal with the most sensitive angle of 50° .

Figure 1.9 shows the three types of experimental set-ups performed in our lab-based system to obtain angle resolved XPS data of water vapor at 0.8 Torr with an ionic liquid, 1-butyl-3-methylimidazolium acetate [C₄mim][Ace]. The first attempt was collecting spectra of [C₄mim][Ace] on a flat Au foil in the angular collection mode (a). The second was collected the same sample in acceleration mode while manually tilting the sample from 20° to 35° in increments of 5° (b). The last experiment was manually bending the Au foil with the ionic liquid deposited on the bend leading to a collection angle of 64° (most surface sensitive) while collecting spectra in acceleration mode.

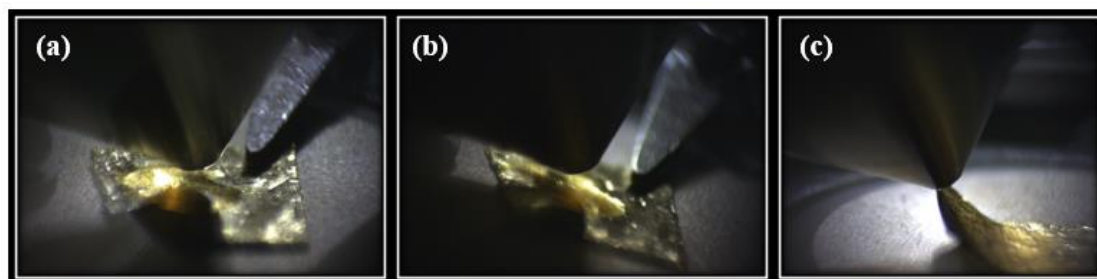


Figure 1.9: Three types of experimental set-ups where spectra are collected in angular mode (a), spectra are collected in acceleration mode while tilting the sample (b) and spectra are collected in acceleration mode on a bent foil while tilting the sample (c).

Angular collection mode allows one to collect angle resolved data without tilting the sample. The two-dimensional detector of our AP-XPS instrument has an angular resolved range of 14° .⁹ Figure 1.10 shows the angle resolved XPS O 1s spectrum collected of [C₄mim][Ace] in the presence of 0.8 Torr. An overlap of two

different portions of the one spectrum (Slice 2 and Slice 1+3) shows a similar structure. This shows that there is no noticeable difference of water interactions at the surface sensitive angle and bulk angle in this collection mode.

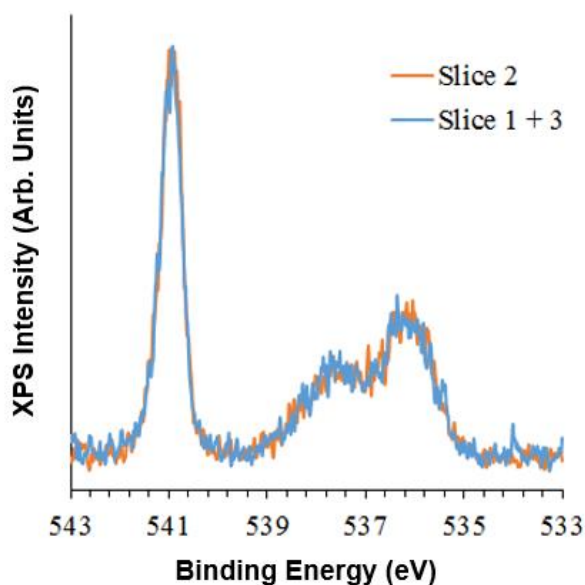


Figure 1.10: O 1s spectra at a water vapor pressure of 0.8 Torr using angular collection mode.

The next experiment was collecting spectra of [C₄mim][Ace] in the presence of 0.8 Torr using acceleration mode, shown in Figure 1.11. To obtain angle resolved data using acceleration collection mode, the sample manipulator needs to be tilted where a larger angle will lead to a more sensitive spectrum while a smaller angle will lead to deeper penetration into the sample and will produce a more bulk spectrum. Initially, spectra were collected at the steepest angle of $\Theta = 35^\circ$ (most surface sensitive). The sample was rotated 5° less until the sample holder was “flat” at $\Theta = 20^\circ$. The inelastic

mean free path (λ) of electrons from the O 1s with a value of 3.0 nm has been calculated using the NIST software.¹¹ At a $\Theta = 20^\circ$ rotation, the calculated probing depth ($3\lambda\cos(20)$) is 8.5 nm. If the angle is then rotated to 35° , the calculated probing depth is 7.4 nm. The image taken of the sample in the AP-XPS chamber shows the sample position at all four angles, where the most surface sensitive angle is at $\Theta = 35^\circ$ and the least surface sensitive is at $\Theta = 20^\circ$. Also, it is noted that the $\Theta = 35^\circ$ position is as surface sensitive as one can obtain with a flat gold foil. Any more rotation would lead to the aperture hitting the IL droplet or sample holder. Also note, rotating the sample $\Theta > 20^\circ$ would lead to the other side of the sample holder (right) hitting the x-ray window. Due to both of these reasons, the only experimental angles that can be tested for an ionic liquid sample in acceleration mode is between $\Theta = 20^\circ$ and 35° .

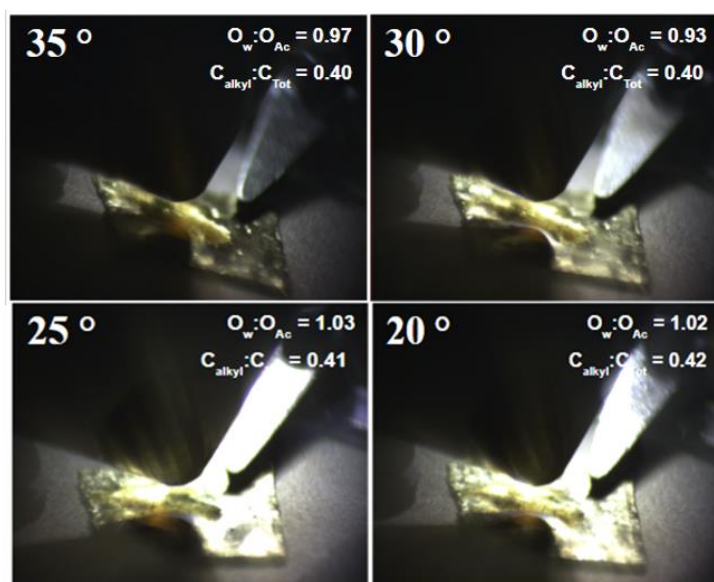


Figure 1.11: Pictures taken of sample while changing the collection angle in acceleration collection mode. The key components ratios at each angle are also shown.

Peak area ratios between different elements were also calculated in order to see if one element was more prevalent at the surface (i.e. more concentrated at the steeper angles). Results of these calculations for the enhancement of water ($O_w:O_{Ac}$) and aliphatic carbon ($C_{alkyl}:C_{Tot}$) are also shown in Figure 1.11. As the angle is increased from $\Theta = 20^\circ$ to 35° in increments of 5° the $O_w:O_{Ac}$ ratio is the following: 1.02, 1.03, 0.93, 0.97. At each angle, the ratio is relative unchanged, which means there is no enhancement of water at the most surface sensitive angle of $\Theta = 35^\circ$. In a similar manner, the $C_{alkyl}:C_{Tot}$ ratio from $\Theta = 20^\circ$ to 35° in increments of 5° is the following: 0.42, 0.41, 0.40, and 0.40. This also says there is no enhancement in the aliphatic carbon chain when angled at $\Theta = 35^\circ$.

A qualitative assessment of water enhancement is shown in an overlay of the XPS spectra at $\Theta = 20^\circ$ (orange) and $\Theta = 35^\circ$ (blue) for O 1s (a), C 1s (b), and N 1s (c) at 0.8 Torr in Figure 1.12. In the O 1s spectra, the first peak at lower BE of 530.5 eV is the O_{Ac} component while the second peak at 532.5 is the O_w component. Increasing the angle does not lead to a visible enhancement of the O_w peak. In the C 1s spectrum (b), the aliphatic carbon chain (C_{alkyl}) is seen at 285 eV. An overlap of these two spectra shows no change or C_{alkyl} enhancement. Finally, an overlap of the N_{ring} component also does not show any enhancement.

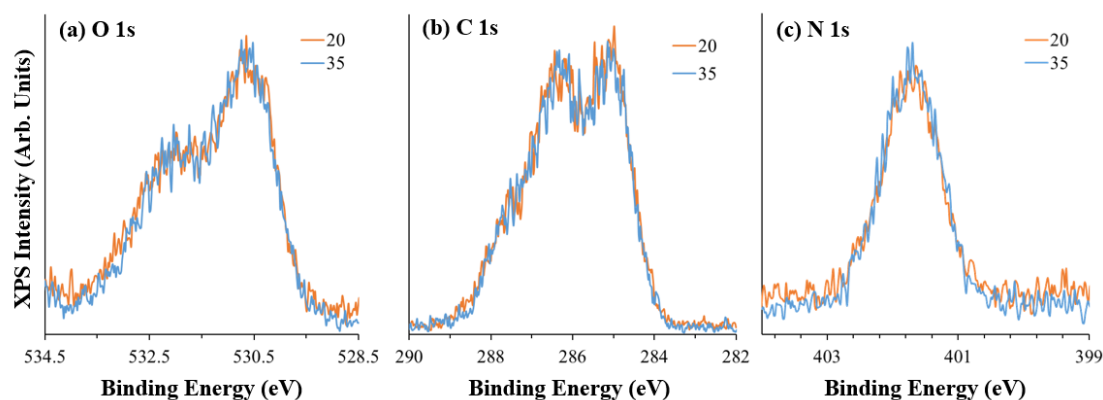


Figure 1.12: AP-XPS spectra for O 1s (a), C 1s (b), and N 1s (c) at 1.0 Torr of water vapor and two angles: $\Theta = 20^\circ$ (orange) and 35° (blue).

It is not surprising that there is no enhancement of water or aliphatic carbon at a $\Theta = 35^\circ$ collection versus a $\Theta = 20^\circ$ collection. AR-XPS experiments are usually done at grazing angle ($\Theta > 70^\circ$) and normal emission angle ($\Theta = 0^\circ$). In most angle resolved studies of ionic liquids, the angle comparison is $\Theta = 0^\circ$ to 80° .¹² Using our equation for probing depth, an angle of 0° will give a probing depth of 9 nm while $\Theta = 80^\circ$ has a probing depth of 1.5 nm. As one can see, comparing these two angles, leads to major differences in probing depth. On the other hand, the two extreme angles in this study ($\Theta = 20^\circ$ and 35°) only have a probing depth difference of 1.1 nm.

In order to obtain a more surface sensitive angle within our AP-XPS chamber, the [C₄mim][Ace] droplet was deposited on a folded Au foil. This deposition was placed as a very thin film at the top of the tilted foil and added to the foil all the way down to the crease. In doing so, the whole area of the Au foil that is folded up is covered with a thin film of IL. It is expected that overtime, some of that IL droplet will drip down the film (due to gravity) leaving a large amount of the droplet at the crease. Our hope was that depositing across the whole folded section of the Au foil would

allow some IL to remain at the tip of the Au foil, allowing for a more surface sensitive XPS analysis.

The folded Au foil on the sample holder is shown in Figure 1.13. The black lines represent a 90° angle between the sample holder surface and the crease of the Au foil. In addition, the first red dashed line represents a $\Theta = 20^\circ$ angle from the 90° black line of at the crease. To determine the angle obtained by bending the Au foil, a line was drawn from the crease and the top of the Au foil, represented by the second red dashed line. At this point, the angle was determined to be $\Theta = 36^\circ$. Finally, the image shows that the Au foil from the sample holder as an angle of $\Theta = 34^\circ$. By visibly determining these angles, the collection angle for angle-resolved XPS was calculated to be $\Theta \sim 56^\circ$ ($20^\circ + 36^\circ$).

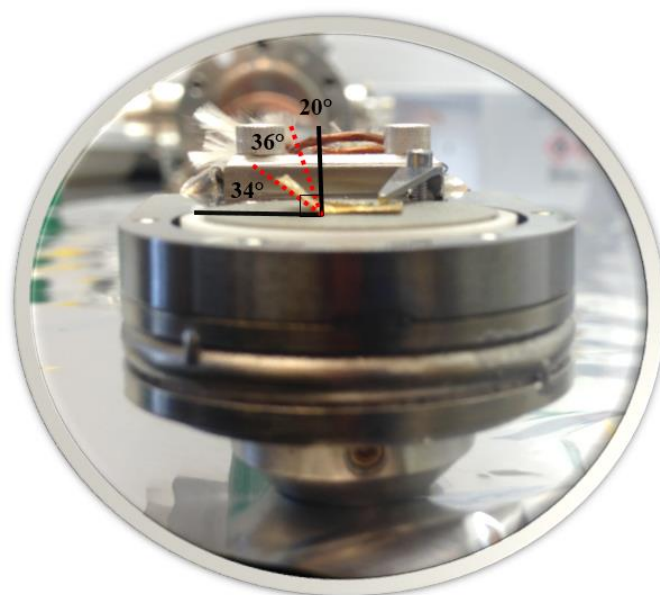


Figure 1.13: Experimental set-up of bent foil on sample holding, showing the capability to collect angle resolved XPS data at $\Theta \sim 56^\circ$.

Images of the sample within the AP-XPS chamber are shown in Figure 1.14. In the first image (a), one can see the position of the aperture to the IL sample, showing that the aperture is positioned at the top of the folded Au foil that has a thin layer of IL. Also in this image, one can see a collection of IL at the crease of the Au foil. While this was expected, XPS analysis could show that a thin layer of IL was still present at the top of the Au foil. In addition, the survey spectrum did not show Au at this sampling position, furthering confirming the thin layer of IL that remained. The second image (b) was captured through a window attached on the chamber to show the x-ray window. In this image, one can see the silicon window that the x-rays penetrate through as well as the aperture position at the tip of the folded Au foil.

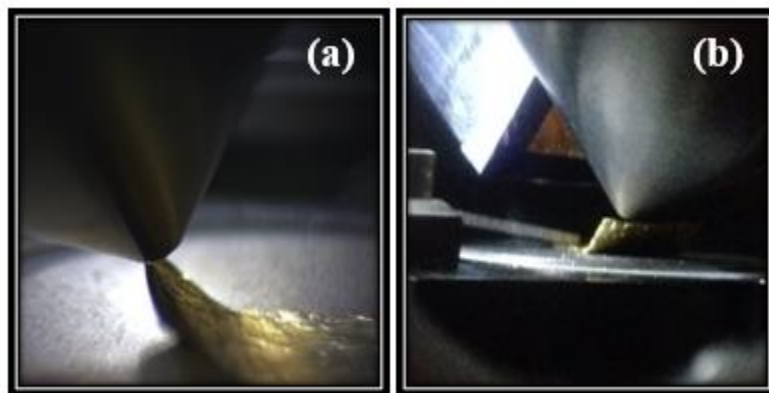


Figure 1.14: Images of the sampling position in the AP-XPS chamber where the aperture is position at the tip of the Au foil at a collection angle of $\Theta = 56^\circ$ (a) and the same collection position captured through a window on the AP-XPS chamber (b).

Once 0.8 Torr of water vapor was introduced into the chamber, the O 1s and C 1s spectra were collected. Then, the sample holder was tilted an additional $\Theta = 8^\circ$, so

the Au foil was closer to the aperture leading to a more sensitive angle collection of $\Theta = 64^\circ$. Similarly, the C 1s and O 1s spectra were collected at this angle. A summary of the ratios of $O_w:O_{Ac}$ and $C_{alkyl}:C_{Tot}$ species in the presence of 0.8 Torr water vapor is shown in Table 1.4.1. The initial experiment of a flat Au foil at $\Theta = 35^\circ$ is also present to compare to the other two surface sensitive angles of $\Theta = 56^\circ$ and 64° obtained by using a bent foil.

As one can see, there is relative no change in the ratio of $C_{alkyl}:C_{Tot}$ at all three collection angles of $\Theta = 35^\circ$, 56° , and 64° . This may be due to a small (or relatively no) clustering of the aliphatic carbon species of the imidazolium chain at 0.8 Torr. This shows that the largest collection angle at 64° is not surface sensitive enough to show clustering of the carbon species. However, when comparing the ratio of $O_w:O_{Ac}$, one can see a slight change in the ratio when the collection angle is changed from $\Theta = 35^\circ$ to the more surface sensitive angle of $\Theta = 56^\circ$, where the ratio changes from 0.97 to 0.84, indicating slightly less water on the surface. By changing the collection angle from $\Theta = 56^\circ$ to 64° , the $O_w:O_{Ac}$ ratio remains relatively unchanged with ratios of 0.84 and 0.82, respectively. This shows that a much more surface sensitive collection angle (e.g. 80°) is needed to confirm whether water is enhancement within the first few nanometers of the interface.

Table 1.2: Ratios of IL Species at Different Collection Angles in the Presence of 0.8 Torr

Au Foil	Collection Angle ($^\circ$)	$O_w:O_{Ac}$	$C_{alkyl}:C_{Tot}$
Flat	35	0.97	0.40
Bent	56	0.84	0.41
Bent	64	0.82	0.43

In addition, XPS spectra of the O 1s (a), C 1s (b), and N 1s (c) species at the standard collection angle of $\Theta = 20^\circ$ (orange) and the most surface sensitive angle of 64° (blue) of [C₄mim][Ace] in the presence of 0.8 Torr of water vapor are shown in Figure 1.15. The overlap of these two spectra does not show any noticeable change in any of the species. This qualitative assessment further confirms that a more surface sensitive collection angle may be necessary to see any species enhancements of ionic liquids in the presence of water.

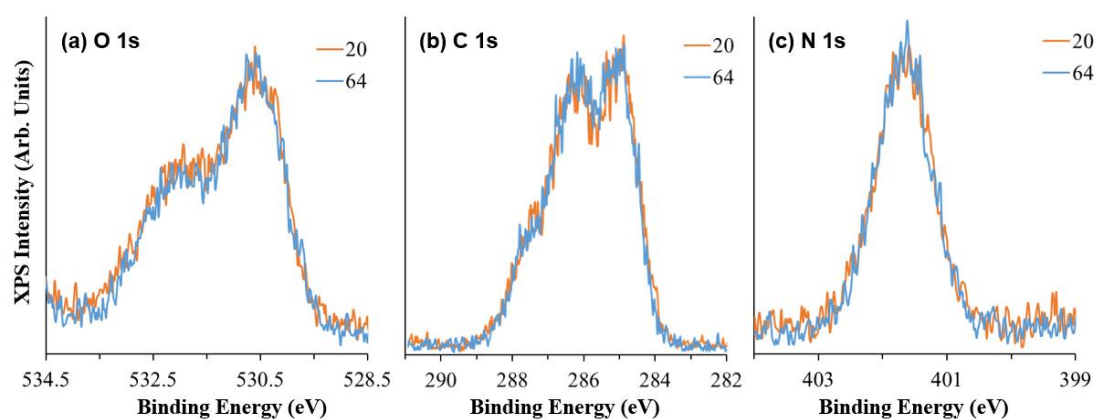


Figure 1.15: XPS spectrum comparing data collected at $\Theta = 20^\circ$ (orange) and $\Theta = 64^\circ$ for O 1s (a), C 1s (b), and N 1s (c).

While we have yet to establish an experimental set-up necessary to conduct surface sensitive studies via our lab-based AP-XPS system, we do believe it is necessary to conduct these studies to confirm the position of water and aliphatic carbon within the interfacial region that we currently probe (~ 8 nm). In order to confirm the position of these species within the interfacial region, one could conduct a depth profile experiment using an AP-XPS system at a synchrotron facility. As

discussed in the introduction, these systems can vary the X-ray energy, ultimately changing the probing depth. In doing so, a high X-ray energy will probe deeper into the sample while a lower X-ray energy will probe at the outmost interface. By changing the X-ray energy, a depth profile from one nanometer up to several nanometers could be created and would show a complete picture of where each species resides within our probing depth. By comparing the ratio of species like O_w and C_{alkyl} conducted with our instrument, one would be able to determine if the O_w and C_{alkyl} species within the IL are enhanced within the first few nanometers of the interface. One thing to note is that AP-XPS systems at synchrotron facilities have samples that are completely vertical, which could lead to the IL dripping off of the substrate. One could attempt to fold the bottom edge of the Au foil in attempts to catch the dripping IL and conduct the experiment on the remaining IL on the middle of the foil.

1.5 Mass Spectrometer on Different Stages

An e-Vision quadrupole mass spectrometer (QMS) is used in various experiments to monitor gas phase products as well as background gases present within our AP-XPS chamber. This QMS can measure m/z from 1-100 amu with a maximum operating pressure of 7.6×10^{-5} Torr. Most AP-XPS experiments performed in the chamber operate up to Torr level gases well above the maximum pressure of the QMS. For this reason, the position of the QMS on the AP-XPS chamber was assessed in the presence of water vapor, due to it being the most common gas used in our studies.

A schematic of the different pumping stages in the lab-based AP-XPS system is shown in Figure 1.16. The lab-based system has 5 different stages. The system is differentially pumped with turbo pumps, where Stage 1 uses two pumps, Stage 2 uses two pumps, Stage 3 uses 1 pump, and Stage 4 uses 1 pump. This technique of

differential pumping allows Torr level gas exposure in Stage 0, while still maintaining high vacuum in Stage 4. The sample is exposed to Torr level gases in the high pressure stage or Stage 0. Once the emitted photoelectrons enter the next stage (Stage 1), they are differential pumped through the stages until they reach the hemisphere under high vacuum of 1×10^{-8} Torr at Stage 4. The pressure changes in orders of magnitude with each stage, so while Stage 0 is exposed to 20 Torr of N_2 gas, Stage 3 only experiences 8×10^{-7} Torr.¹³ In addition, the largest pumping load is experienced at Stage 1, due to it being the stage immediately following the high gas exposure.

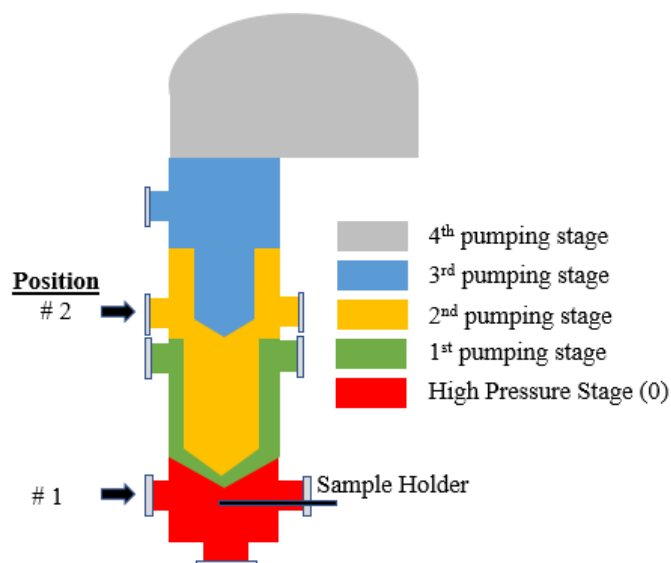


Figure 1.16: Schematic of the different pumping stages of our lab-based AP-XPS system and the two M/S positions explored.

In this experiment, we tested the mass spectrometer position in the present of water vapor up to 5.0 Torr at two different pumping stages: Stage 0 (Position #1) and Stage 2 (Position #2). The water vapor ($m/z=18$) was monitored as a function of increasing pressure from high vacuum of 10^{-8} Torr up to 5.0 Torr. The mass spectrum

collected 5 scans with an accuracy of 3 and a m/z range of 0 – 50 amu at each water vapor pressure. The chamber temperature was 21 °C.

The mass spectrometer plumbed to Position #1 was explored and the experimental results are shown in Figure 1.17. There is a small increase in the M/S response pressure from water vapor pressure exposure of 3.8×10^{-8} to 1.0×10^{-6} Torr. At a water vapor pressure of 1.0×10^{-5} Torr, the M/S response pressure (orange) drastically increases to 3.5×10^{-5} Torr. When 1.0×10^{-4} Torr of water vapor is present, the M/S response (red) reaches its maximum response of 8.7×10^{-5} Torr.

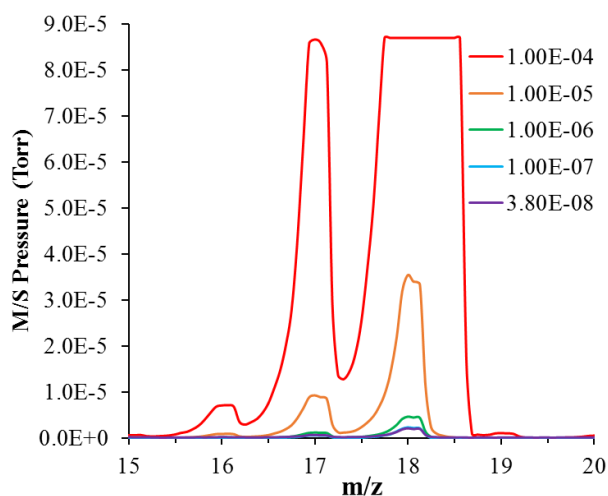


Figure 1.17: Mass spectrometer signal as a function of water vapor exposure while mass spectrometer is on Stage 0.

The M/S response was further analysis from a plot of M/S pressure vs. water vapor pressure present in Stage 0 shown in Figure 1.18. At water vapor pressures $< 1.0 \times 10^{-6}$ Torr, the M/S pressure response change is relatively small. At water vapor

pressures $> 1.0 \times 10^{-6}$ Torr, the mass spectrometer response drastically increases linearly until it reaches its maximum response.

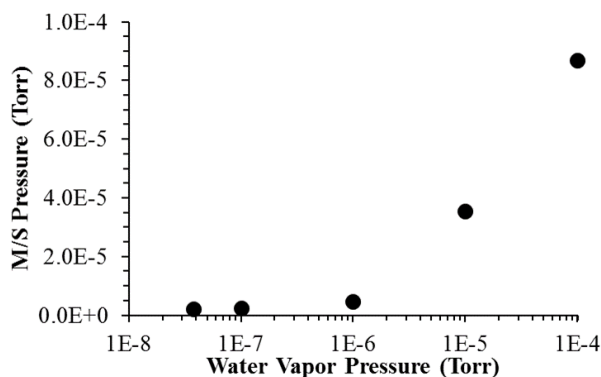


Figure 1.18: The mass spectrometer pressure at Position #1 as a function of water vapor pressure at Stage 0.

The mass spectrometer was then removed from Stage 0 and plumbed to Position #2 on the 2nd pumping stage. The initial M/S response was monitored at larger water vapor pressures starting at 0.8 Torr. The M/S spectra collected from water vapor pressures of 0.8 to 5.0 Torr is shown in Figure 1.19. The maximum exposure of 5.0 Torr was chosen due to it being the maximum water vapor pressure most samples are exposed to within our chamber. At the initial water vapor of 0.8 Torr, the pressure of the mass spectrometer at $m/z = 17.94$ is 2.89×10^{-7} Torr. The mass spectrometer pressure continues to increase, with the maximum pressure observed by the mass spectrometer of 2.64×10^{-6} Torr when there is 5.0 Torr of water vapor in Stage 0.

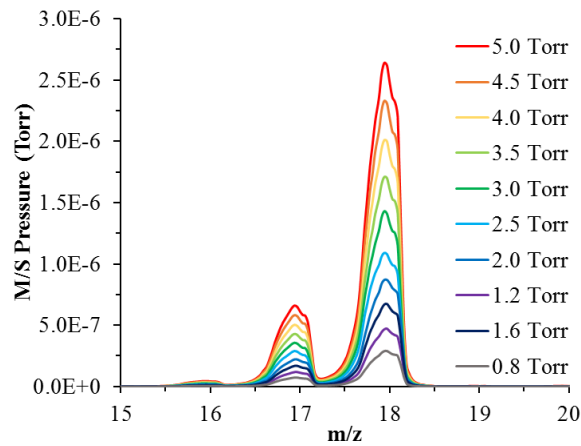


Figure 1.19: Mass spectrometer signal as a function of water vapor exposure while mass spectrometer is on Stage 2.

The mass spectrometer pressure at $m/z = 17.94$ as a function of water vapor pressure present in Stage 0 is shown in Figure 1.20. There is a linear relationship between the mass spectrometer pressure at Stage 2 and the water vapor pressure at Stage 0, with $R^2 = 0.9967$. While the mass spectrometer pressure is increasing, it is an order of magnitude below the maximum operating pressure of the QMS.

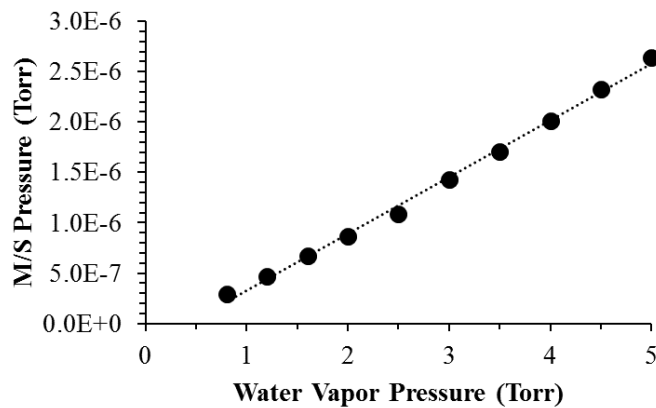


Figure 1.20: The mass spectrometer pressure at Position #2 as a function of water vapor pressure at Stage 0.

The position of the mass spectrometer on the lab-based AP-XPS system is critical. The mass spectrometer can not operate on Stage 0 at water vapor pressures $> 5 \times 10^{-5}$ Torr due to the MS signal flooding. However, when the mass spectrometer is placed on Stage 2, it can safely operate up to a water vapor pressure of 5.0 Torr. The mass spectrometer pressure and water vapor pressure have a linear relationship. The effect of other gases, including oxygen and nitrogen, on the mass spectrometer pressure will also need to be tested prior to any high pressure experiments.

Chapter 2

WATER AT IONIC LIQUID INTERFACES

2.1 Water at Ionic Liquid Interfaces

2.1.1 Introduction

With tunable properties, ionic liquids (ILs) are sparking interest in a variety of fields including catalysis, gas separation, and electrochemistry. Hydrophilicity in ILs has been heavily studied and experiments have emphasized that even the most hydrophobic ILs will absorb small amounts of water over time. For this reason, water is viewed as an impurity that can affect IL bulk physical properties including density, viscosity, conductivity, and gas absorption.

The density and viscosity of ionic liquid has been shown to decrease as the water mole fraction increases from 0 to 0.1 for both hydrophilic and hydrophobic ionic liquids.¹⁴ On the contrary, ionic conductivity increases with increasing water mole fraction.¹⁵ Water also affects surface properties including surface tension and gas absorption through an interface for CO₂. The surface tension of acetate imidazolium ionic liquids of various chain lengths ($n = 2 - 6$) has been shown to increase with increasing water mole fraction.¹⁶ In large quantities, water has been shown to decrease the CO₂ capacity in hydrophilic ILs.¹⁷

Understanding ionic liquid interfaces is important for tailoring ionic liquid with specific properties. There are three interfaces (or phases in contact with the *interfacial layer*) of interest, shown in Figure 2.1) for IL-water systems: vacuum-IL,

gas-IL, and solid-IL. Due to ionic liquid low vapor pressures, the vacuum-IL interface is the most studied, both experimentally and theoretically, with emphasize on imidazolium ILs.¹⁸ Few experimental studies have look at the IL-vacuum interface for IL-water mixtures due to the high vapor pressure of water and water loss from the sample over time. On the other hand, most theoretical studies heavily emphasize this interface due water condensing within the ionic liquid. The IL-gas interface is of importance for ILs as potential gas absorbent of CO₂ from flue gas. At this interface, there are no theoretical studies due to water condensing within the interfacial layer. The IL-solid interface has been studied experimentally at mica, gold, and silica interfaces and one theoretical study at an electrified gold interface. The IL structure is significantly impacted when an electric potential is applied to the interface which has significant implications in electrochemistry and electrocatalysis

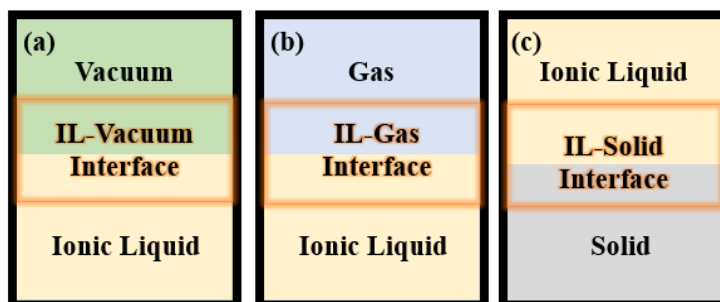


Figure 2.1: Three different interfaces of interest including ionic liquid -vacuum (a), ionic liquid-gas (b), and ionic liquid-solid (c).

This section will focus heavily on three interfaces (vacuum, gas, solid) and waters effect on the ionic liquid structure at these interfaces. There are a few reviews¹⁹⁻²³ and books¹⁸ that have focused on the interaction between ILs and water

emphasizing the importance of computational studies²², solute-solvent interactions,^{19,21} and water induced changes in surface structure^{20,23} The goal of this Chapter is to give an up to date overview of the surface sensitive analytical techniques and theoretical studies utilized to probe the IL-vacuum, IL-gas and IL-solid interfaces in the presence of water. The focus herein will be on the use of microscopy, spectroscopy, mass spectrometry and scattering techniques (Table 2.1), as well as molecular dynamic simulations (Table 2.2). As will be shown in this section, some published experiments are performed by depositing water onto a frozen IL at the start of experiments, while others perform studies with the IL remaining a liquid throughout the entire experiment. We will refer to the former condition as water “adsorption” onto a solid surface. In some cases, water is found to be enhanced at the IL interface while it is in a liquid state. Interestingly, this suggests that water can act as a surfactant in an IL, but we will refrain from the use of the term “adsorbed” water as a point of clarity when the system is completely liquid, using instead water “uptake” at the interface when the system is fully liquid.

2.1.2 Ionic Liquid-Vacuum Interface

The low vapor pressures of ILs make them amenable to probing by vacuum based surface spectroscopy techniques. As shown in Table 2.1, techniques that have been utilized to examine the IL-vacuum interface include Neutral impact collision ion scattering spectroscopy (NICISS)^{24,25}, ultra-high vacuum X-ray photoelectron spectroscopy (UHV XPS)⁶ and line of sight mass spectroscopy (LOSMS).²⁶ All three of these surface techniques are traditionally vacuum based given the inbound probes aimed at the sample (ions for NICISS) and outbound probes coming off the sample (ions for LOSMS, electrons for XPS and neutrals for NICISS) are significantly

scattered in the presence of a gas phase. Experiments performed with these techniques were done at pressures of 150 μ Torr or lower.

Neutral impact collision ion scattering spectroscopy (NICISS) is a low energy scattering vacuum-based technique. Experiments were performed by introducing an IL-water mixture into the sample chamber. Water evaporated as a function of time from the IL-water mixture while the interface was probed in a background of water vapor. This technique provides atomic information for these mixtures and a probing depth up to 20 nm with a resolution of a few tenths of a nm near the surface.²⁵ NICISS allows for the examination of the IL interfacial atoms as a function of depth into the sample. However, IL-water mixtures are difficult to probe due to the rapid desorption of water during measurements and signal loss due to water vapor collisions with the He⁺ ions above the sample. There have been two studies that have investigated the surface structure of hydrophilic [HMIM][Cl]-water mixtures at low²⁵ and high²⁴ water mole fractions (x_w) in the range of 0.0025 to 0.71.

In the first study, Reichelt et al.²⁴ investigated [HMIM][Cl]-water x_w from 0.43 to 0.71. Depth profiles of the carbon, oxygen, and chlorine could show that when water is added to the ionic liquid, a distinct layering at the surface occurs where the cation, depicted from the carbon depth profile, remains at the outmost layer and the water, the oxygen depth profile, adsorbs at the inner layer. The presence of water gives rise to a migration of the anion, represented by the chlorine depth profile, deeper into the bulk. As the water concentration increases, the cation remains unchanged at the outmost surface while the anion shifts deeper into the bulk. As the anion shifts (~ 1 nm) closer to the bulk as a function of increasing water concentration, there is a

surface enhancement of the imidazolium cation (~ 0.4 nm) and water (~ 0.7 nm) relative to the bulk beyond 35 nm.

In the second NICISS study, Ridings et al²⁵ also investigated the same IL-water mixture at lower water concentrations concluding the cation shows a strong presence at the surface while the anion is closer to the bulk. Similar to the previous study by Reichelt and colleagues²⁴, it was concluded that water influences the composition and charge distribution at the ionic liquid-vacuum interface. However, the concentration profiles of the anion and cation showed different trends. The chloride anion is enhanced at the surface at larger water concentrations while the imidazolium cation is closer to the bulk. This trend was attributed to a stronger interaction between the cation and anion at $x_w < 0.025$.

X-ray photoelectron spectroscopy (XPS) is a surface sensitive vacuum-based spectroscopy that has been used to investigate the surface structure of ionic liquid at the IL-vacuum interface.²³ X-ray photons (Al or Mg $K\alpha$) are used to probe the surface while chemical and elemental information about the sample surface is obtained.²⁷ This technique provides an atomic level picture of the surface with a probing depth of 10 nm. On the contrary, IL-H₂O mixtures are relatively difficult to study due to rapid desorption of water into the vacuum and X-ray induced damage at the surface of ionic liquid has been reported after long X-ray exposure times.²³

Only one XPS study has investigated water at the ionic liquid surface.⁶ In this experiment, the probing depth was calculated to be 10 nm. To prepare the sample surface, multilayers of water were adsorbed on the surface of a solid ionic liquid, [OMIM][BF₄] at 175K, using a capillary doser. The obtained UHV XPS survey spectra before and after dosing was able to show a large O 1s peak due to water

adsorption after dosing. The high resolution F 1s, N 1s, C 1s, and B 1s spectra showed damping of all peaks which was further evidence that there was an over layer of water on top of [OMIM][BF₄] after dosing. The sample was then heated which led to the desorption of water from the ionic liquid surface, and XPS spectra was recorded over at temperature range of 175-300K. By monitoring the decrease in O 1s intensity and assuming first order desorption kinetics, the heat of adsorption of water onto [OMIM][BF₄] was estimated to be 76 kJ mol⁻¹. Additionally, the N 1s spectra showed the growth of a second peak at lower binding energy which is attributed to X-ray induced damage of the [OMIM] imidazolium ring.

There has also only been on study using Line of Sight Mass Spectroscopy (LOSMS) to examine water at the IL-vacuum interface. LOSMS is an analytical technique that provides mass to charge ratio of different ionized fragments at rapid speeds. In this technique, only species that are ionized on the surface are detected while all other gases are pumped away with a cyropump. One disadvantage to this method is that it does not provide structural information at the surface and is not suitable for non-volatile samples. For ionic liquids, it has been used to measure the surface kinetics by sticking probability (S) and it has been coupled with temperature programmed desorption (TPD) experiments to determine adsorption enthalpies of water into the ionic liquid at the IL-gas interface as well as the ionic liquid underlayer.

Using LOSMS coupled with TPD, the desorption of water from the ionic liquid surface was investigated. The sticking probability measurements were carried out by monitoring the [OH]⁺ fragment while adjusting the sample temperature from 113 to 295K or water vapor pressure above the solid IL. For the TPD experiments, solid [HMIM][BF₄] was dosed with water vapor at 100K. The sample was then heated

while monitoring the mass to charge ratio of the $[\text{OH}]^+$ fragment. The results were analyzed to generate a potential energy diagram of enthalpy versus distance from the IL-gas interface for $[\text{HMIM}][\text{BF}_4]$. The TPD experiments determined the physisorption energy of water from the solid ionic liquid surface to be 41 kJ mol^{-1} . The graph also shows the enthalpy of adsorption of water (34 kJ mol^{-1}) into the bulk as previously determined with TPD XPS. These results ultimately show that water prefers to reside in the ionic underlayer while the imidazolium alkyl chain is at the IL-vacuum interface.

2.1.3 Ionic Liquid-Gas Interface

The influence of water at the IL-gas interface has been predominantly investigated by Sum Frequency Generation (SFG)²⁸⁻³⁵, with additional studies utilizing X-ray Reflectivity (XR)³⁶, Neutron Reflectometry (NR), Flowing Jet Sheet Beam (FJSB) and Ambient Pressure XPS (AP-XPS)³⁷. In ambient air, water vapor is present at Torr level pressures. For these IL-gas studies the total pressures ranged from 5 Torr (AP-XPS) up to atmospheric pressure (SFG, XR, NR). In some cases the IL was exposed to pure gas phase water within a vacuum chamber (SFG, AP-XPS, FJSB), or IL mixtures with liquid water were examined in lab air or N_2 (SFG, XR, NR).

Sum Frequency Generation (SFG) is a surface sensitive, nonlinear vibrational spectroscopy technique. This technique uses two beams (visible laser at a fixed frequency and variable infrared laser) that overlap at the interface to generate a third beam that is the sum of the two incident beams.²⁷ SFG detects the molecular vibrations of molecules at the interface.²⁷ One of the main advantages of SFG is the ability to probe surfaces in-situ with gases and liquids. To date, SFG has been the most common

technique used for studying IL-gas interfaces (see Table 2.1).²⁸⁻³⁵ One major disadvantage to these studies is that it only probes the top layer of the surface, so the interaction between the anion and water is not revealed. A variety of imidazolium ILs have been studied with different alkyl chain lengths and anions, shown in Table 2.1. A common observation was the effect of water on the cation orientation for hydrophilic and hydrophobic ionic liquids.

One of the first SFG studies of IL-water at the IL-gas interface was investigated by Rivera et al.²⁹ In this study, the cation orientation for hydrophilic, [C₄mim][BF₄], and hydrophobic, [C₄mim][imide], was investigated in the presence of water vapor at 5×10^{-5} and 20 Torr. Using SFG, spectra of ssp polarization was generated for both ionic liquids, [C₄mim][imide] and [C₄mim][BF₄], at the two water vapor pressures. For both the hydrophobic and hydrophilic ionic liquid the SFG spectra show notable features of aliphatic C-H modes of a butyl chain indicating the imidazolium ring is parallel to the surface plane. When the water vapor is increased to 20 Torr, the spectra for the hydrophilic [C₄mim][BF₄] does not change indicating no orientation change from the addition of water. However, the hydrophobic ionic liquid, [C₄mim][imide], shows two new distinct vibrations assigned to the anti-symmetric and symmetric stretch of the H-C(4)C(5)-H within the imidazolium ring. It is suggested that the cation reorients for hydrophobic ILs to help solvate the water molecules.

X-ray reflectivity (XR) is a surface sensitive technique used to characterize the composition of rough surfaces and interface structures. This technique uses x-rays to probe a surface and detects the change in electron density. It is a powerful method to investigate liquid surfaces on the tens of nanometers scale with sub-nanometer resolution. However, XR does have a loss of phase information (which can lead to

data misinterpretations), so it should be complimented with simulations to reach conclusions about the X-ray reflectivity curves.³⁸

Lauw et al. used XR to study the IL-gas interface of [Bmpyr][Tf₂N]-water mixtures in a N₂ environment. The surface structure was probed up to 8 nm and X-ray scattering length density (SLD) profiles were generated. The SLD profile shows that in the presence of water, the interface consists of an outer layer composed of the cation alkyl chain pointing towards the gas phase (region A) with the underlying imidazolium ring cation interacting with water (region B). Underneath are anions followed by a mixture of cations, anions and water (region C) which extends into the bulk. A snapshot of the ionic liquid and water from an MD simulation of the SLD profile was able confirm the three different regions of the interface. The MD snapshot further confirmed a clear interfacial enhancement of water in region B.

Neutron reflectometry (NR) is a neutron diffraction technique that shines a beam of neutrons onto a flat surface and measures the intensity of the reflected beam. Advantages to using neutrons over x-rays is that neutron scattering amplitudes vary randomly between elements and it is sensitive to lighter elements.³⁹ This technique is also non-destructive. One disadvantage when studying ionic liquid-water systems, is that surface contamination is a concern for water studies since it leads to a rise in incoherent background during a typical experiment. At the ionic liquid- gas interface, NR has been utilized once to study [C₈mim][Br] and water at various water concentrations.⁴⁰ The results suggests a change in the surface structure where a depletion of the [C₈mim][Br] is seen at critical micelle concentrations (cmc) greater than $0.15 \pm 0.05 \text{ mol dm}^{-3}$.

Flowing Jet Sheet Beam (FJSB) King and Wells (K-W) method has been used to study [BMIN][Tf₂N] and water.⁴¹ In this type of experiment, a FJSB of [BMIN][Tf₂N] is generated in a vacuum. A pulsed beam of D₂O is exposed to the IL chamber and the dissolution analysis is measured by a quadrupole mass spectrometer (QMS). FJSB K-W method has been used to study [BMIN][Tf₂N] and water has a function of temperature and collision energy to determine energetics. Figure 6 shows the initial dissolution probability (S) as a function of temperature and collision energy. The dissolution probability decreases as a function of increasing pressure and the initial dissolution decreases with increasing collision energy. For the first time, energetics (ΔH and ΔS) were extracted from a plot of the dissolution probability vs $1/T$ and determined to be $\Delta H = -53 \pm 8 \text{ kJ mol}^{-1}$ and $\Delta S = -210 \pm 30 \text{ J mol}^{-1} \text{ K}^{-1}$.⁴¹

Ambient Pressure XPS (AP-XPS) has been used to study the IL-gas interface. This technique has the same advantages as XPS along with the ability to investigate the IL water interaction at more environmental relevant conditions. AP-XPS provides information at the top few nanometers of the IL-gas interface and information about the electronic environment. AP-XPS provides elemental information about core-shell electrons as well as elemental changes from binding energy shifts. The interaction of water vapor with [C₄mim][Ace] was recently investigated and will be discussed in Section 2.2.

2.1.4 Ionic Liquid-Solid Interface

The influence of water at the IL-solid interface has been investigated using Atomic Force Microscopy (AFM)⁴²⁻⁴⁹ and Surface Enhanced Infrared Absorption Spectroscopy (SEIRAS)⁵⁰. AFM studies of ionic liquids and water are typically performed in lab air, allowing experimental conditions of ionic liquid studies to

include vapor or liquid phase water. AFM has been used to study the effect on water at different IL-solid interfaces including mica, silica, and Au electrode, see Table 1.

Most AFM studies have focused on the IL-mica interface.^{42,44,46-48} SEIRAS, a vibrational spectroscopy, has been used to investigate the IL-Au electrode interface in vacuum and water-saturated argon gas.⁵⁰

Atomic Force Microscopy (AFM) is a type of scanning force microscopy (SFM) that measures the force between a sharp tip and the sample surface to obtain topographic information about the sample. It operates in two modes: constant force (sample is adjusted vertical during measurements) or constant height (sample position is constant and cantilever tip deflection is recorded). AFM is highly sensitive with the ability to probe single atoms. This technique is not quantitative or destructive. It is typically performed in lab air, allowing experimental conditions of ionic liquid studies to include vapor or liquid phase water.

AFM has been used to study the effect on water at different IL-solid interfaces including mica, silica, and Au electrode, see Table 1. Most AFM studies have focused on the IL-mica interface.^{42,44,46-48} The interface of [C₆mim][EtSO₄]-mica was studied in dry (< 5% RH) and wet (~45%RH) conditions.⁴⁶ The generated force isotherms were collected with a sharp silicon tip at the IL-solid interface. The dry sample (< 5% RH) showed two film thickness transitions with an average size of $\Delta \sim 0.7$ nm and $\Delta \sim 1.1$ nm due to mixed layer (composed of cation and anion) and single cation, respectively. In the dry sample, the cation layer ($\Delta \sim 1.1$ nm) was closest to the solid mica surface. When the sample is wet (RH ~ 45%), an additional film-thickness transition appears with an average size of $\Delta \sim 0.31$ nm closest to the mica solid surface, followed by a transition of $\Delta \sim 1.1$ nm and $\Delta \sim 0.75$ nm. The first transition (size $\Delta \sim 0.31$ nm) is

attributed to a monolayer of water closet at the IL-solid interface. Interestingly, a slight expansion ($\Delta \sim 0.05$ nm) is noted in the third film-thickness transition of 0.75 nm, which is due to some water interacting with the [EtSO₄] anions. This study gave insight to the effect of water at solid-IL interfaces and the precaution needed when collecting AFM measurements of ionic liquid interfaces in open lab air.

Surface enhanced infrared absorption spectroscopy (SEIRAS) is a vibrational spectroscopy used to probe electrode surfaces.⁵¹ In this technique, IR photons are used to probe the surface and provides vibrational information. The spectral resolution is 4 cm⁻¹. SEIRAS operates under vacuum conditions and is nondestructive. It has been used to successfully probe the vicinity of an electrode surface within the top 5 nm.⁵² Although this technique has been used study the IL-solid interface for multiple systems⁵³, there has only been one SEIRAS publication of gas phase water at the IL-solid interface.⁵⁰

SEIRAS has been used to investigate the IL-Au electrode interface in vacuum and water-saturated argon gas.⁵⁰ The humid environment contained water at 700 ppm. The study monitored changes in the C-F vibration (describes the anion) and O-H vibration (water) when the sample was dry and under humid conditions with potentials from - 0.5 V to + 0.9 V. The data obtained suggested that water condensation is potential dependent and interacts stronger with the anion than cation. Water condensation was also significant at higher potentials, due to anions being more abundant at the Au electrode interface. Although this is the only publication to date utilizing SEIRAS to study the IL-solid interface, this study explored the potential-dependent structure at the IL-solid interface and observed water condensation on a positively charge gold electrode for the first time.

2.1.5 Molecular Dynamic Simulation Studies of IL Interfaces

Molecular Dynamic (MD) simulation studies have been utilized to study the IL-vacuum and IL-solid interface in the presence of water. In studies of the IL-vacuum interface, an IL is surrounded by a vacuum component and usually the water is introduced as water vapor which ends up predominantly within the condensed phase IL throughout the simulations. The IL-vacuum interface has been studied under different environments including water, water and CO₂, and flue gas that consists of water, N₂, CO₂, and O₂. MD studies that examine the influence of water on the IL-solid interface are scarce (see Table 2.2).

The IL-vacuum interface in the presence of water has been studied on hydrophilic⁵⁴⁻⁵⁷ and hydrophobic^{55,58} ILs. The IL-vacuum interface was studied for a two phase system containing 368 IL pairs of [C₄mim][NTf₂] in the liquid phase and 96 water vapor molecules using MD.⁵⁸ The simulation ran for 12 ns at 350 K. Three different density profiles consisting of the anion, cation, and water molecules, carbon atoms of the alkyl chain and water, and anion atoms and water were generated and compared. In the density profile of the anion, cation, and water, the water molecules dissolved in the interior of the slab, showing a phase change from vapor to condensed water. The density profile of the carbon atoms of the alkyl chain and water show the alkyl chain populated at the IL-vacuum interface with the water molecules at the interior layer of the ionic liquid. In the last density profile of the anion atoms and water, a small water peak is seen just below the density of the oxygen on the anion. This indicates a stronger interaction between the anion and water due to the negatively charged oxygen species on the acetate anion. A comparison of all three density profiles concluded that water avoids the outermost interfacial region that is populated with the imidazolium alkyl chain and rather presides in the underlayer at the interface

that consists of the anion. This location preference is due to strong hydrogen bonding between water and the negatively charged oxygen atoms of the [NTf₂]⁻ anion.

The IL-vacuum interface has also been studied in the presence of CO₂⁵⁸ and flue gas containing CO₂, H₂O, N₂, and O₂.⁵⁹⁻⁶¹ Piperazinium ionic liquids have been studied in the presence of flue gas.⁶⁰ The simulation cell contained 125 ionic liquid pairs, 20 CO₂ molecules, 20 H₂O molecules, 10 O₂ molecules, and 150 N₂ molecules with a production run of 10 ns at 350K. At the end of the simulation, density profiles and occupancy profiles of the IL-flue gas system were generated. The density profiles for all three ILs, [MP][LA], [MP][PR], and [EP][LA], show similar results. The CO₂ molecules are adsorbed at the interface while the H₂O molecules cross the interface ~0.4-0.5 nm below the CO₂ layer. The N₂ shows small affinity to adsorb at the surface, but has a weaker affinity than the CO₂ molecules. The O₂ does not show any affinity for the IL surface. Similarly, the occupancy profile also shows the affinity of the molecules at the IL surface, where H₂O resides at the interlayer below the surface and CO₂ adsorbs at the surface. This study obtained results about the interfacial behavior of gas molecules (CO₂ and H₂O) at the IL-vacuum interface that are important for understanding the mechanism of CO₂ capture in environmental conditions where other gases are present. Understanding these gas interactions is highly important if CO₂ will be used as an alternative for flue gas treatment.

MD has also been utilized to explore water's effect at the IL-solid interface.⁶² In this study, the mixture of IL and water was enclosed between two electrified interfaces. Two hydrophobic ionic liquids were studied: [C₄mim][PF₆] and [C₄mim][BF₄]. The system contained 656 IL pairs and 12 water molecules between. The structure of double layers in humid [C₄mim][PF₆] were generated to show the

water and ion density profiles and the space charge density by the cation and anion. At negative potential, $\sigma = -0.16 \text{ C/m}^2$, the cation shows a greater density to the electrode than the anion. At positive potential, $\sigma = 0.16 \text{ C/m}^2$, the anion has a greater space charge density at the electrode. Water resides near the electrode regardless of the potential applied, but has a larger accumulation around the positive electrode. This is due to its strong interaction with the anion, which is accumulated more at the positive electrode than the cation. These initial MD results are awaiting experimental confirmation, but provide insight to water molecules near polarized and nonpolarized electrodes.

2.1.6 Summary and Future Outlook

Many studies have explored the ionic liquid structure at the vacuum, and gas, and solid interface. Although progress has been made on understanding the influence of water on these interfaces both experimentally and theoretically, more progress needs to be made to paint a clear picture. Surface layering is seen at all ionic liquid interfaces and consists of three regions: interfacial layer, transition zone, and bulk liquid. Water, as liquid or gas, has an influence on this surface layering as well as the electronic structure of the ionic liquid. Of the studies that explore the ionic-water systems, most have only concluded findings about surface layering in the presence of water. Studies utilizing AP-XPS to correlate water mole fraction with change in electronic structure of an imidazolium ionic liquid are scarce; however, these studies could be beneficial to the community to understand IL-gas interactions on a molecular level.

Water appears to absorb at the inner layer just below the alkyl chain and has a stronger interaction with the anion than the cation. At the ionic liquid-gas interface,

SFG has shown that water sits at the inner layer, just below the alkyl chain of the imidazolium cation, while AP-XPS shows water forms a strong bond with the anion. At the ionic liquid-vacuum interface, UHV XPS and LOSMS have been used to determine adsorption enthalpies of water vapor by studying water desorption on a solid ionic liquid surface. At the ionic liquid-solid interface, AFM has shown a strong layering at the surface in the presence of water. MD studies at the ionic liquid-vacuum interface conclude that water adsorbs at the inner layer just below the alkyl chain and forms strong interactions with the anion while the ionic liquid-solid interface shows water manifests near the positive electrode where the anion is present.

While some studies have focused on the structure of ionic liquids in the presence of water, most studies of the IL-water system have focused on bulk properties using IR and NMR. A lot more information needs to be obtained to determine the effect of water on the ionic liquid interfaces for hydrophobic and hydrophilic ionic liquids. Experimentally, studies on the chemistry between ionic liquids and water at these interfaces needs to be built upon. Most experimental studies have focused on where the water resides at the interface, instead of how it interacts with the ionic liquid at that interface. To the best of our knowledge, AP-XPS studies are scarce and could provide insight onto the chemical interaction of water with ionic liquids. Theoretically, the ionic liquid interfaces are hardly explored due to long computational times and more complex systems. In particular, the IL-solid interface in the presence of water has only been studied once. The IL-vacuum interface simulation studies are scarce when compared to simulations on ionic liquid bulk simulations.

In order to gain a clear understanding of water at the ionic liquid interfaces, efforts should be made to address the conditions above. Using multiple techniques at

these interfaces will also provide a more concise, fundamental understanding of IL-water systems. These systems should also be investigated at all water mole fractions ($0 < x_w < 1$) for hydrophobic and hydrophilic ionic liquids.

Table 2.1. Experimental Studies Probing IL Interfaces in the Presence of Water

Interface	Technique	H2O Phase ^a	Ionic Liquid	P _{max} (Torr) ^b	Refs
IL/Vac	NICISS	l	[C ₆ mim][Cl]	1.5 x 10 ⁻⁴	24
	NICISS	l	[C ₆ mim][Cl]	7.5x10 ⁻⁶	25
	UHV XPS	g	[C ₈ mim][BF ₄]	3 x 10 ⁻⁶	6
	LOSMS	g	[C ₈ mim][BF ₄], [C ₂ mim][NTf ₂]	4 x 10 ⁻⁸	26
IL/Gas ^c	SFG	g	[C ₄ mim][imide]	200	28
	SFG	g	[C ₄ mim][BF ₄], [C ₄ mim][imide]	20	29
	SFG	l	[C ₄ mim][BF ₄]	Air	30
	SFG	g,l	[C ₄ mim][BF ₄]	24 Torr	31
	SFG	l	[C ₄ mim][BF ₄]	Air	32
	SFG	g	[C ₄ mim][PF ₆]	Air	33
	SFG	l	[C ₄ mim][FAP]	Air	34
	SFG	l	[C ₄ mim][O ₃ SOC1]	Air	35
	XR	l	[C ₄ mpyr][NTf ₂]	N ₂	36
	NR	l	[C ₈ mim][Br]		40
	FJSB	l	[C ₄ mim][NTf ₂]	Air	41
	AP-XPS	g	[C ₄ mim][Ace]	5 Torr	37
				Interface	
IL/Solid	AFM	g	[C ₄ mim][FAP]	Mica	42
	AFM	l	[C ₂ mim][OTf]	Au (111)	43
	AFM	l	[C _n mim][NTf ₂]	Mica	44
	AFM	l	[C ₂ mim][NTf ₂]	Mica, Au electrode	45
	AFM	g	[C ₆ mim][O ₃ SOC ₂]	Mica	46
	AFM	g,l	[C _n mim][NTf ₂]	Mica	47
	AFM	l	[C ₄ mim][BF ₄], [C ₂ mim][NTf ₂]	Mica/Silica	48
	IRAS	g	[C ₄ mim][NTf ₂]	Au electrode	50
	AFM	l	[C ₂ mim][dca], [C ₄ mpyr][dca]	HOPG	49

a. IL exposed to gas phase water (g) and/or mixed with liquid water (l).

b. Approximate maximum pressures (P_{max}) during in situ probing of IL interface. Experiments under atmospheric pressure either exposed to ambient air or N₂.

Table 2.2. Molecular Dynamics Studies of IL Interfaces in the Presence of Water

Interface	Species Other Than Water	Ionic Liquids	Refs
IL/Vac	None	[C ₁ mim][Cl]	57
	None	[C ₄ mim][BF ₄], [C ₄ mim][PF ₆]	55
	None	[C ₄ mim][BF ₄]	56
	None	[C ₁ mim][Cl]	54
	None	[C ₄ mim][BF ₄], [C ₄ mim][PF ₆]	63
	None	[C ₄ mim][BF ₄], [NTf ₂], [PF ₆]	64
	Air	[C ₄ mpyr][NTf ₂]	36
	CO ₂	[C ₄ mim][NTf ₂]	58
	CO ₂ , N ₂ , O ₂ , CH ₄ , C ₂ H ₆ , C ₂ H ₄	[C ₄ mim][PF ₆]	59
	CO ₂ , N ₂ , O ₂	[C ₂ mim][Gly]	17
	CO ₂ , N ₂ , O ₂	[MP][PR], [EP][lac]	60
IL/Solid	None	[C ₄ mim][PF ₆], [C ₄ mim][NTf ₂]	62

2.2 Interfacial Water Uptake at the Ionic Liquid-Gas Interface of 1-Butyl-3-Methylimidazolium Acetate

2.2.1 Introduction

Imidazolium-based ILs using acetate as the anion are hydrophilic, biodegradable, and have low viscosities relative to other conventional ILs.⁶⁵ Acetate-based ILs are widely used in the dissolution of biomass including cellulose and chitin.⁶⁶ It has been shown that a small amount of water can be used to regenerate chitin and limit the dissolution of cellulose into ILs.⁶⁷ Water has also been shown to affect CO₂ absorption into acetate-based ILs and its mixtures with biopolymers.⁶⁸ Molecular dynamic (MD) simulations of imidazolium acetate ILs suggest that the presence of water leads to a decrease in CO₂ absorption as both water and CO₂ compete for the same solvation sites of the acetate IL.⁶⁹

As discussed heavily in Section 2.1, processes including gas absorption, gas separation, heterogeneous catalysis, and heterogeneous electrocatalysis involve a gas crossing the IL-vapor interface. Throughout the years, a number of surface analysis tools have been utilized to understand the IL-vapor interface in the presence of water including SFG²⁸, XPS⁶, and LOSMS²⁶. While surface science studies have provided valuable molecular level information for the interaction of water with IL-vapor and IL-vacuum interfaces, a quantitative assessment of water in the interfacial region and the impact of water on the electronic environment of the IL-water system as a function of water vapor pressure under near ambient conditions is still lacking.

The vacuum-IL interface has been studied extensively using UHV XPS since 2005,⁴ although few UHV XPS studies have examined ILs with an acetate anion.⁷⁰ Herein we examine 1-butyl-3-methylimidazolium acetate, [C₄mim][Ace], under adsorption-desorption conditions at room temperature and Torr level water vapor pressures up to a maximum pressure of 5 Torr using AP-XPS to probe the top few nm of the IL-gas interface. We present for the first time a quantitative assessment of water uptake using XPS under Torr level pressures and the significant impact water has on the moiety specific electronic environment of the IL-vapor interface as a function of water mole fraction.

2.2.2 Experimental Details

AP-XPS experiments of the IL-water vapor interface were conducted using a lab-based system with a monochromatic Al anode X-ray source (Scienta MX650) operating at 20 mA and 10 kV and an electron energy analyzer with a differentially pumped electrostatic lens (Scienta, HiPP-2). The details for this system have been described previously.¹³ Experiments were performed using a 0.5 mm aperture and the

swift acceleration electron capture lens mode.⁷¹ The collection angle of the electrons was 20° relative to the sample normal. Survey spectra were captured at 200 eV pass energy while C 1s, N 1s and O 1s were captured at 100 eV pass energy.

[C₄mim][Ace] (Iolitec, 98%) has a melting point of -20 °C with a bulk density of 1.06 g cm⁻³.⁷² The commercial IL was used as received without further purification and stored at room temperature in a vacuum desiccator. Samples were prepared for entry into the AP-XPS vacuum chamber by placing a thin film (< 0.3 mm thick, ~7 mm dia.) onto a 10 x 10 mm flame annealed Au foil (Alfa Aesar, 99.9975%, 0.25 mm thick). The sample holder was mounted and the AP-XPS spectroscopy chamber was pumped down overnight to a base pressure of 1 x 10⁻⁷ Torr prior to the start of experiments.

Water vapor was introduced into the AP-XPS analysis chamber using a variable leak valve, behind which was a glass bulb containing 18.2 MΩ-cm water. Prior to the start of AP-XPS experiments the water was degassed via three freeze-pump-thaw cycles. The sample temperature was monitored using a type-K thermocouple near the Au foil. AP-XPS spectra were collected with the sample temperature held at 21.7 ± 0.1°C and constant water vapor pressures ranging from 10⁻⁶ to 5 Torr.

XPS spectra were analyzed using peak fitting software (CasaXPS, v2.3.16) with linear background subtraction and Gaussian-Lorentzian (70%-30%) peak fits. All XPS spectra were charge referenced to the C 1s alkyl peak with a binding energy (BE) of 285.0 eV.^{73,74} The C 1s alkyl peak as an internal reference for water-IL interactions was chosen for several reasons including it is the most common reference in the UHV XPS IL literature, it was used in a previous UHV XPS study of an acetate-based

imidazolium IL,⁷⁰ the alkyl chain is hydrophobic and expected to be the least sensitive to water induced BE shifts, and an analysis of all the components in the system confirmed all other peaks shift to higher BEs relative to the C 1s alkyl upon introduction to water vapor. A description of individual peak fits will be discussed in Section 2.2.3.

2.2.3 Quantitative Assessment of Interfacial Water Uptake

A survey spectrum in Figure 2.2 (a) was collected prior to water exposure at a base pressure of 1.2×10^{-7} Torr. There are three major XPS peaks in the C 1s, N 1s and O 1s regions due to the carbon, nitrogen, and oxygen species in the [C₄mim][Ace] molecular structure. The feature at 977 eV representing oxygen KLL. There is no additional evidence of any other elements present, indicating that our IL sample is devoid of any measurable contamination at the IL-vacuum interface. This remains true throughout the duration of the experiment.

Figure 2.2 also shows high resolution spectra of the C 1s, N 1s and O 1s regions prior to the start of water vapor exposures. The O 1s (Figure 2.2 (b) and N 1s (Figure 2.2 (c)) regions give single peaks associated with the oxygen in the acetate anion (O_{Ac}) and nitrogen in the imidazolium ring cation (N_{ring}), respectively. The O_{Ac} and N_{ring} components are at 530.4 and 401.7 eV, respectively. As an example, the two oxygen atoms on the anion are in resonance, so they have the same electron density resulting in one XPS peak. The C 1s region (Figure 2.2 (d)) is fit with three different components at 285.0, 286.2 and 287.3 eV. These species are colored according to the chemical structure in Figure 2.2 (a) and named the following: C_{alkyl} (blue), C_{ring} (red), and C_{ox} (green), respectively. Both the 285.0 (C_{alkyl}) and 287.3 eV (C_{ox}) peaks are present on the anion and cation, while the 286.2 eV (C_{ring}) peak is associated only with

the imidazolium cation. To further confirm the purity of the ionic liquids, the peak areas of the C 1s species are compared. The stoichiometric ratio of the peak areas is 4:4:2 for the blue:red:green carbon atoms, respectively. This ratio matches the ratio of the chemical structure and further confirms the correct C 1s peak fittings.

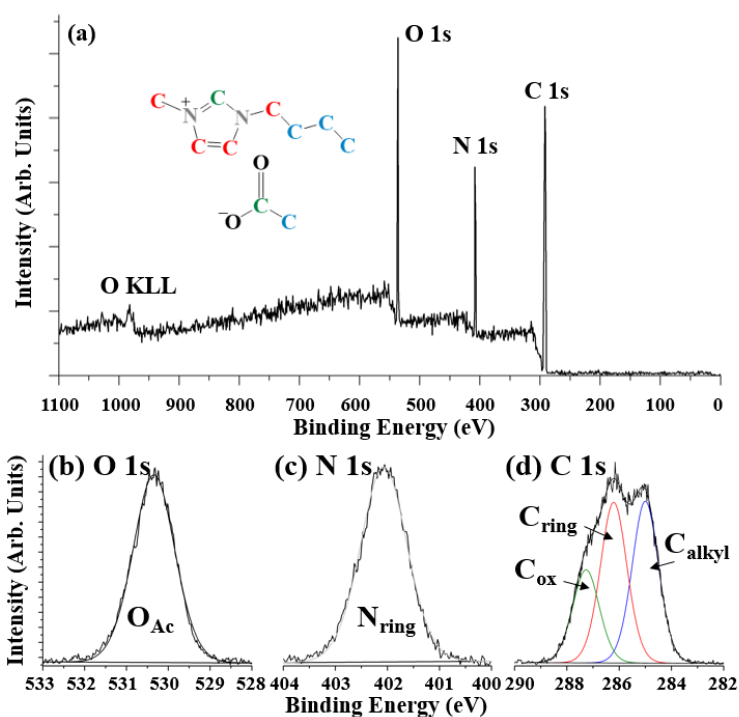


Figure 2.2: Survey spectrum (a) of [C₄mim][Ace] along with chemical structure. Initial [C₄mim][Ace] spectra in the (b) O 1s, (c) N 1s and (d) C 1s regions. Colors of peak fits correspond to elemental species in IL chemical structure.

AP-XPS experiments of [C₄mim][Ace] were conducted by exposing the IL to water vapor as a function of increasing pressure up to 5.0 Torr. A subset of the C 1s (a) and N 1s (b) spectra from 1.2×10^{-7} to 5.0 Torr are shown in Figure 2.3. From 10^{-6}

Torr to 10^{-2} Torr, the C 1s and N 1s spectrum remains unchanged. At 0.1 Torr, water vapor and interfacial water peaks are apparent in the O 1s spectra (discussed in detail in the latter paragraph). For the C 1s and N 1s spectra at 0.1 Torr, slight attenuation (decrease in the peak intensity) is seen when comparing to the first water exposure at 10^{-6} Torr. After 0.1 Torr, where water adsorption is rapid up to 5.0 Torr, attenuation is more apparent in both the C 1s and N 1s components. This attenuation as a function of water vapor is due to water absorption into the interfacial region and diluting the ionic liquid and an increase in the gas phase water above the sample. There is a visible shift to higher binding energy in the C_{ring} , C_{ox} , and N_{ring} components which will be discussed in Section 2.2.4. When looking at the C 1s spectra, there is an obvious growth in the C_{alkyl} component as water vapor pressure increases. A detailed description of this growth will be discussed in Section 2.2.5. There are no other changes in the N 1s spectra as a function of water vapor pressure. The top spectra in both the C 1s and N 1s shows the high resolution spectra collected immediately after water is pumped out of the chamber. As one can see, the attenuation is not present in either spectra. Additionally, the growth in the C 1s spectra is not apparent after water vapor is pumped out of the chamber. This shows the reversibility of the interfacial water uptake into $[\text{C}_4\text{mim}][\text{Ace}]$.

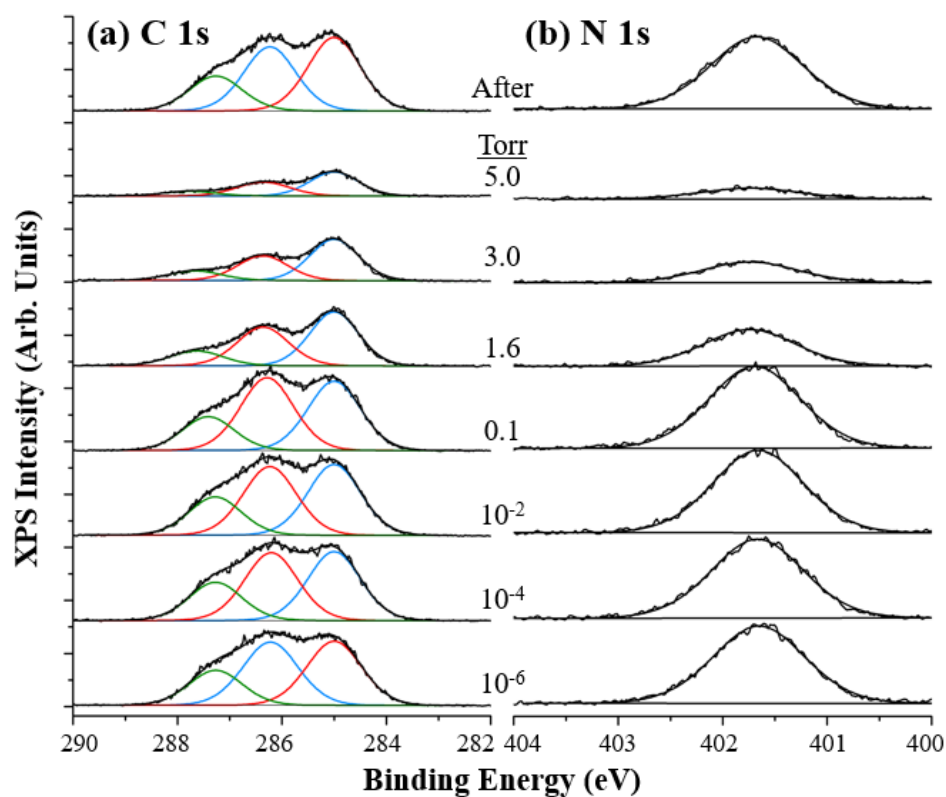


Figure 2.3: Spectra of C 1s (left) and N 1s (right) from 1.2×10^{-7} to 5.0 Torr. Spectral attenuation is apparent after 0.01 Torr, which is where water vapor and interfacial water is seen in the O 1s spectrum.

The O 1s high resolution spectra was also collected as a function of water vapor pressure. Figure 2.4 shows representative O 1s spectra during the room temperature isotherm. From 10^{-6} to 10^{-3} Torr the acetate ion (O_{Ac}) is the only oxygen species observed at the IL-vapor interface. This shows that water is not being absorbed within the interfacial region at these low vapor pressures. At 10^{-2} Torr, a small shoulder forms on the high BE side of O_{Ac} . This peak is due to the uptake of water (O_w) at the IL-vapor interface and is initially seen at 531.6 eV. At 0.1 Torr, gas phase water (O_{gas}) between the IL surface and the entrance aperture to spectrometer becomes

detectable at 535.6 eV. As the pressure increases from 10^{-2} to 5.0 Torr, the O_{Ac} peak decreases. This is due to two contributing factors: the gas phase attenuation of the XPS signal by the increasing water vapor pressure above the sample, and the dilution of the acetate signal due to an increase in the uptake of water in the interfacial region as evidenced by an increase in the O_w/O_{Ac} ratio with water vapor pressure. Upon pumping out the water vapor by opening the AP-XPS chamber to a turbo pump and immediately taking an O 1s spectrum (top spectrum), water rapidly depletes from the interface evidence by the disappearance of the O_w and O_{gas} components.

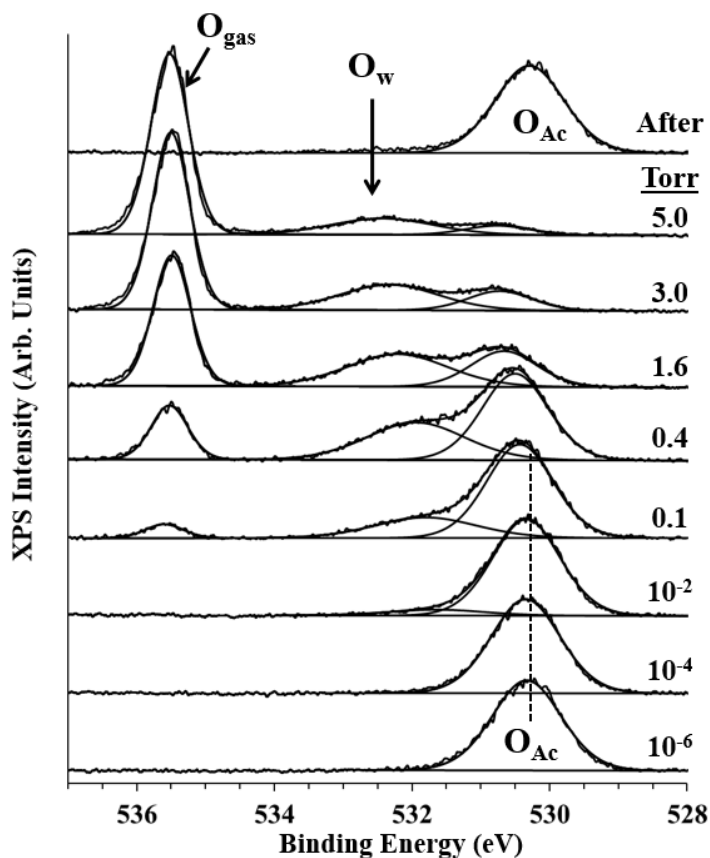


Figure 2.4: O 1s AP-XPS spectra as a function of increasing water vapor pressure. Top spectra taken shortly after water vapor pumped out of the chamber.

To quantitatively assess the amount of water in the interfacial region, the water mole fraction (x_w) was calculated from O 1s integrated peak areas (I) of O_w and O_{Ac} using Equation 2.1. The kinetic energy of electrons from an O 1s orbital using the Al K_{α} X-ray source is ~ 950 eV. This corresponds to an inelastic mean free path (λ) of 3.0 nm for electrons escaping from the IL surface, calculated using NIST software¹¹ with the Gries predictive formula and a bulk density (ρ) of 1.06 g cm^{-3} for $[C_4mim][Ace]$. The thickness of one monolayer of IL is approximated using⁷⁵ $\rho^{-1/3}$, which is 0.68 nm for $[C_4mim][Ace]$. Defining the sampling depth to be $3\lambda\cos(20^\circ)$, the calculated sample depth is 8.46 nm, which accounts for 95% of the signal from unscattered photoelectrons.⁷⁶ We can then calculate that our AP-XPS experiments are probing ~ 12 layers of IL. Assuming water is homogeneously mixed within the 8.5 nm probing depth, the water mole fraction (x_w) can be calculated from O 1s integrated peak areas (I) using:

$$x_w = \frac{n_w}{n_w + n_{IL}} = \frac{I_w}{I_w + \frac{I_{IL}}{2}} \quad (\text{Eqn 2.1})$$

where n_w and n_{IL} are the moles of water and IL, respectively. Thus, $I_w \propto n_w$ (one mole of oxygen per water) and $I_{IL} \propto 2n_{IL}$ (two moles of oxygen per acetate anion).

We were able to obtain the first quantitative assessment of water uptake in the interfacial region of an ionic liquid using Equation (2.1). A room temperature AP-XPS isotherm of water mole fraction versus pressure is shown in Figure 2.5 using linear (black) and log (green) x-axes. First assessment of the log scale plot shows there is no measurable amount of water in the interfacial region from 10^{-7} to 10^{-3} Torr. At 10^{-2} Torr, there is a sudden onset of water uptake that continues to increase up to the maximum water vapor pressure of 5.0 Torr. The water uptake at higher water vapor

pressures is more apparent on a linear scale. From 10^{-2} to 0.1 Torr there is a steep onset of detectible interfacial water with a mole fraction of 40 % at 0.1 Torr. At pressures > 0.8 Torr, water uptake into the interfacial region continues to increase with increasing water vapor pressure up to a maximum of 85 % mole fraction at 5.0 Torr. This maximum water vapor pressure corresponding to ~ 6 waters per IL pair and a relative humidity of 25.5%.

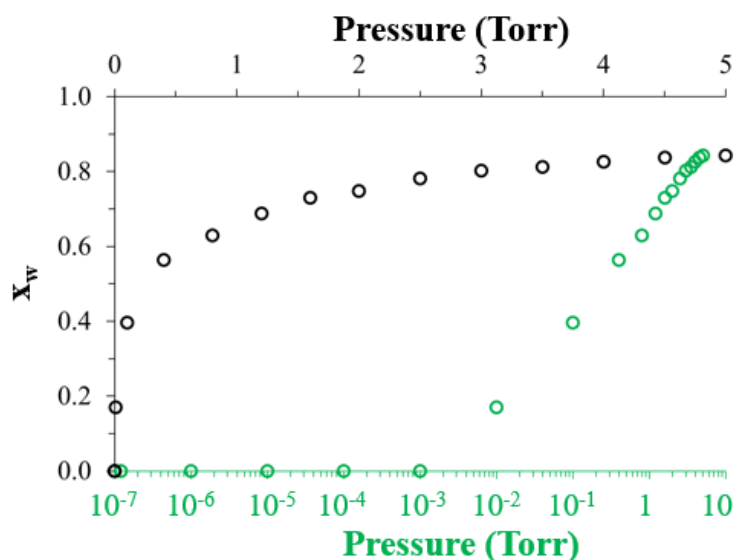


Figure 2.5: AP-XPS isotherm of water mole fraction (x_w) at the IL-vapor interface with water vapor pressure on a log scale (green) and linear scale (black).

2.2.4 Binding Energy Shifts Due to Interfacial Water Sorption

As the water vapor pressure increases above 10^{-1} Torr, all measured interfacial species were observed to shift to higher BEs relative to the C_{alkyl} component. To assess the shift in BE, Figure 2.6 shows the BE change (ΔBE) of O_w , C_{ox} , O_{Ac} , C_{ring} and N_{ring} relative to its original BE under high vacuum as a function of water vapor pressure (a)

and water mole fraction (b). All binding energies are referenced to the C_{alkyl} (blue) component, so the shift for this component remains at a BE = 0 from high vacuum to 5.0 Torr. In Figure 2.6 (a) the Δ BE shifts are negligible below 0.1 Torr for all components. At these low water vapor pressures, the average shift for C_{ox} , O_{Ac} , C_{ring} and N_{ring} are 0, 6.8×10^{-14} , 6.0×10^{-14} , and 1.1×10^{-14} , respectively. This negligible shift along with the lack of O_{w} in the XPS spectra confirms that the BE shift is not a consequence of x-ray exposure, but may be due to the presence of water vapor. From 0.01 to 5.0 Torr where interfacial water is present, an increase in Δ BE is seen for all components as a function of increasing pressure and therefore increasing water at the interface. The binding energy of the O_{Ac} (black) and C_{ox} (green) components shift to the most to the higher BE, with a final BE shift of ~ 0.43 and ~ 0.45 eV at 5.0 Torr, respectively. Also at 5.0 Torr, the N_{ring} (gray) and C_{ring} (red) components shift ~ 0.07 eV and 0.14 eV to higher binding energy, respectively. As stated before, the C_{ox} component is a representation of the most oxidized carbon species on the acetate anion and imidazolium ring (see chemical structure in Figure 2.2). The O_{Ac} component is a clear representation of the oxygen on the acetate anion, or the species that is expected to interact the most with water. On the other hand, C_{ring} and N_{ring} represent the carbon and nitrogen species on the imidazolium ring, respectively. These species would have the least interaction with the interfacial water molecules. A breakdown of the chemical species and the effect of water on the IL molecules leads us to believe that the binding energy shift observed is due to interfacial water uptake, which will be discussed in detail within this section.

Figure 2.6 (b) shows that Δ BE increases roughly linearly with an increase in the water mole fraction, where the magnitude of the shifts increases in the order: $O_{\text{w}} >$

$O_{Ac} \approx C_{ox} > C_{ring} > N_{ring}$. The initial BE shift for all components starts at 0.1 Torr with $x_w = 0.4$. At this pressure, there are about 1.0 water molecules per ionic liquid pair. As the water vapor pressure increases, the number of water molecules per ionic liquid pair increases. Also, there is a clear separation of the ΔBE for each component in the ionic liquid as well as water. At the maximum water vapor pressure of 5.0 Torr and maximum ΔBE , the calculated $x_w = 0.85$. At this maximum water exposure, there is a clear difference in the shifting of each component in the IL-H₂O system.

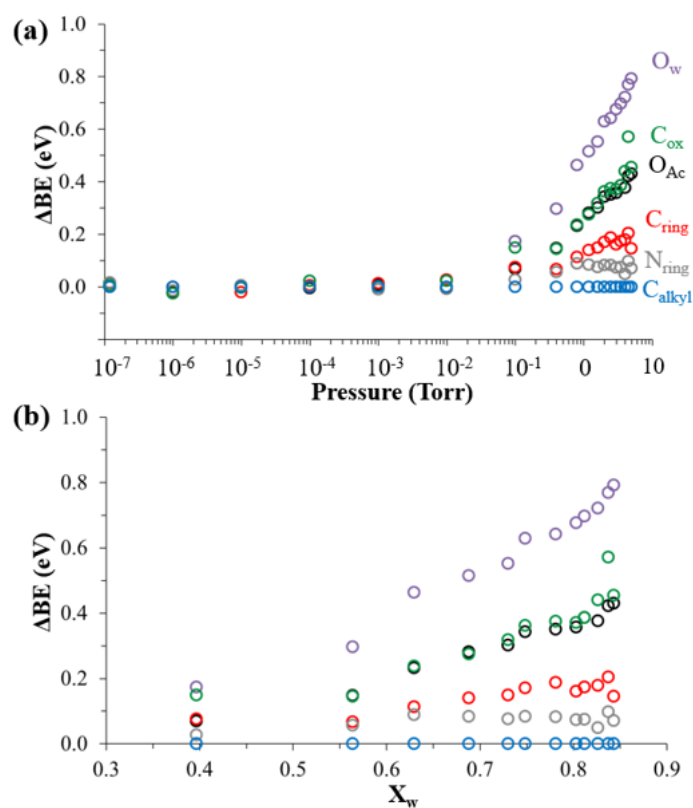


Figure 2.6: Relative binding energy shifts (ΔBE) referenced to the C_{alkyl} BE as a function of (a) water vapor pressure and (b) water mole fraction.

The observed ΔBE shifts are due to a change in the electronic environment of the chemical moiety being probed. The larger ΔBE values for O_{Ac} compared to C_{ring} and N_{ring} shifts are attributed to stronger water-acetate interactions when compared to water interaction with the imidazolium cation. The change in ΔBE for C_{ox} is due to the interaction of water with the acetate carbon and the C=N carbon of the imidazolium ring, and is therefore a combination of interaction with both the anion and cation. Water itself undergoes the largest BE shift, suggesting the electronic environment is strongly influenced mainly through the interaction with the anion.

DFT studies, which focus on electronic structure changes, of acetate based ionic liquids and water were used to better understand the shifts in the components as a function of water vapor pressure. Using ab initio calculations, in the presence of one water molecule, it was shown that water forms two points of hydrogen bonding with the acetate ion and only one with the imidazolium cation.⁷⁷ These results, as well as more recent DFT studies, showed a stronger electrostatic interaction between acetate-water than cation-water.⁷⁷ The ion-water interaction has also been studied in the presence of one and two waters where one water interactions with both the cation and anion (stronger interaction with the acetate anion) and two waters leads to an increase in the interaction energy implying a more favorable interaction between $[C_2mim][Ace]$ and water.⁷⁸ Roohi et al. used DFT to study the imidazolium acetate interaction with one to four water molecules finding the acetate anion has a greater solvation enthalpy than the imidazolium cation and is stabilized by the addition of water molecules.⁷⁹ The strong

interaction between the acetate and water molecules suggests that the large shift in the O_{Ac} is due to a strong interaction between the anion and water.

Molecular simulations have been used to investigate imidazolium-based cations and acetate anion interactions with water finding a strong interaction between the acetate and water.⁷⁷ MD study of [C₂mim][Ace] and water showed at water concentrations $x_w < 0.7$, water-anion interaction is stronger than the water-water and water-cation interactions.⁷⁷ Similarly, radial distribution functions (RDF) of anion-anion pairs at different water mole fractions show the addition of water leads to a splitting of a single peak indicating formation of solvation shells around both anions.⁸⁰ In comparison, the RDF of the cation-anion interaction shows that an increase of water concentration leads to a decrease in two peaks implying a disengagement of the cation-anion interaction with increase water concentration. Another MD study calculated the RDF of the cation-water, anion-water, and water-water interactions finding that water interacts with all three regions through short range interactions and the strongest interaction is with the acetate anion.⁸¹ Additionally, an MD study of water concentrations between $0.05 < x_w < 0.9$ showed a strong anion-water interaction up to $x_w = 0.7$ where higher x_w signify a more homogeneous distribution of the water within the system.⁸² Within the calculated RDFs, a sharp peak in the acetate-water RDF indicates a strong interaction between the acetate anion rather than the [C₄mim] cation. These MD studies give further support for the water molecules interacting stronger with the acetate anion rather than the imidazolium cation which is shown in

our data as large binding energy shift in the O_{Ac} and O_w components as a function of water vapor pressure.

2.2.5 Growth in Carbon Species due to Interfacial Water Sorption

Analysis of the C 1s and N 1s spectra (Figure 2.3) shows that the overall signal decreases with increasing vapor pressure due to gas phase attenuation, like what was observed for the O_{Ac} peak in O 1s spectra. As the water vapor pressure increases, the C 1s spectra show evidence of an increase in C_{alkyl} intensity. Figure 2.7 shows the ratio of C_{alkyl}/C_{tot} as a function x_w (blue) and n_w/n_{IL} (black). The initial ratio of $C_{alkyl}/C_{tot} = 0.3 \pm 0.01$ at $x_w < 0.6$. The initial onset of C_{alkyl} growth occurs at $x_w = 0.6$ or 1.0 water molecule per ionic liquid pair. The ratio increases with the number of water molecules, until it levels off at ~ 4.0 water molecules per ionic liquid pair, with the C_{alkyl}/C_{tot} ratio $= 0.56 \pm 0.01$. The ratio then remains constant up to $n_w/n_{IL}=5.5$. This growth in C_{alkyl} as a function of water mole fraction may suggest a restructuring IL upon interacting with water at the interface or adventitious carbon absorbing within the ionic liquid.

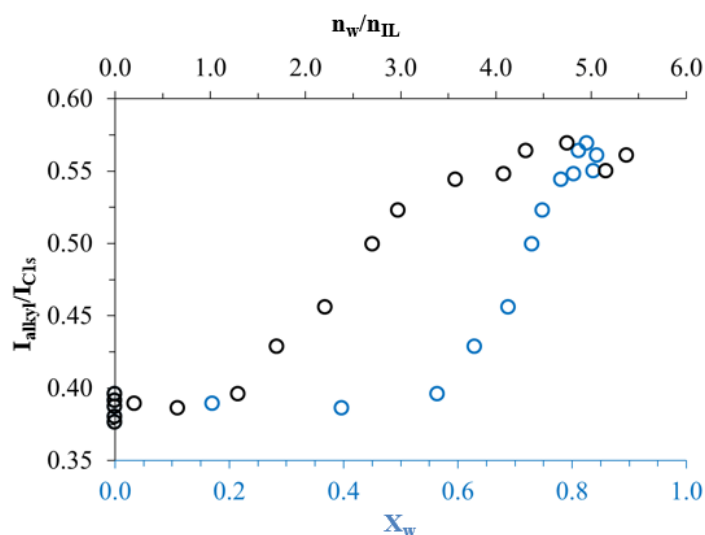


Figure 2.7: Ratio of C_{alkyl} to total C 1s XPS intensity as a function of the number of waters per IL pair (n_w/n_{IL} ; black data) and water mole fraction (x_w ; blue data).

An increase in adventitious carbon with increasing water vapor may be a contribution to the growth of the C_{alkyl} component. However, the bulk solubility of hydrocarbons into ionic liquids is relatively low. It has been shown that the bulk solubility of hydrocarbons into ILs requires high pressures where 760 Torr leads to a solubility of $x < 0.01$.²¹ With this being the case, under AP-XPS experimental conditions of partial pressures well below atmospheres, the solubility of hydrocarbons would be much lower than $x < 0.01$, which is below the XPS detection limit. This is true even if the uptake was enhanced at the interface relative to the bulk. Hence, we believe the C_{alkyl} growth is not likely due to adventitious carbon.

Our observation of growth in the C_{alkyl} component above $x_w = 0.6$ is consistent with experimental studies of IL-water systems that observe a structure change at the interfacial region. Neutron scattering has been used to studied ionic liquid-water

mixtures at a complete range of x_w . Using small angle neutron scattering (SANS), the nanoscale structure of [C₄mim][BF₄]- H₂O mixtures over a full x_w range has been investigated for the first time experimentally.⁸³ Initially at $x_w < 0.7$, water dissolves into the ionic liquid forming a homogenous mixture that does not change the microstructure of the solution. At $x_w > 0.7$, water forms nanometer-sized clusters that grow with the addition of water. The results of these experiments were a confirmation of previous molecular dynamic (MD) simulations of the same [C₄mim][BF₄]/water system.⁸⁴ This type of nanostructuring can be used to explain the sharp increase of C_{alkyl} signal at $x_w > 0.6$.

In addition, recent MD simulation studies have examined imidazolium acetate-water mixtures as a function of x_w .⁸² For long chain imidazolium cations ($n = 4, 6$) a sudden change in IL density is seen at $x_w \approx 0.7$. This change is due to nanostructuring of the IL-water mixture that contains networks of polar regions (water, acetate, and imidazolium ring) and nonpolar regions (imidazolium alkyl chain). This unique onset in nanostructuring at $x_w \approx 0.7$ for [C₄mim][Ace]-water mixtures is consistent with the AP-XPS results herein where a sudden onset of C_{alkyl} intensity is observed. These results suggest that water induced nanostructuring leads to enhanced hydrophobic nanostructures near the IL-vapor interface and our consistent with the previously mentioned [C₄mim][BF₄]-water systems.^{83,84}

Based on the above experimental results of structuring in the ionic liquid bulk⁸²⁻⁸⁴, we suggest the sudden onset of C_{alkyl} at $x_w > 0.6$ is due to nanostructuring of hydrophobic and hydrophilic regions where the hydrophobic nanometer size structures are enhanced at the interfacial region. To further confirmation this observation, MD simulation studies at the IL-vacuum interface for [C₄mim][Ace] as a function of water

mole fraction (x_w) are needed. Such results of nanostructuring at the ionic liquid interface have significant implications for the uptake of other gas phase molecules (such as CO_2). The structural and chemical environment of the interfacial regime is strongly influenced by ambient water vapor which in turn can significantly impact gas phase molecules crossing the IL-gas interface during the process of bulk absorption.

2.2.6 Kinetics of Interfacial Versus Bulk Water Sorption

To assess whether water in the interfacial region is changing as a function of time, AP-XPS spectra were captured back-to-back. Figure 2.8 shows example two overlaid O 1s spectra, where the first one (black) was collected right after reaching 0.4 Torr (RH = 2.0 %), and the second one (orange) collected immediately following the first spectrum. The two spectra overlap each other indicating that the oxygen content in the interfacial region does not change within the time frame of collecting an O 1s spectrum (11.0 minutes). Thus, the amount of interfacial water is constant with time and the system is under adsorption-desorption equilibrium conditions.

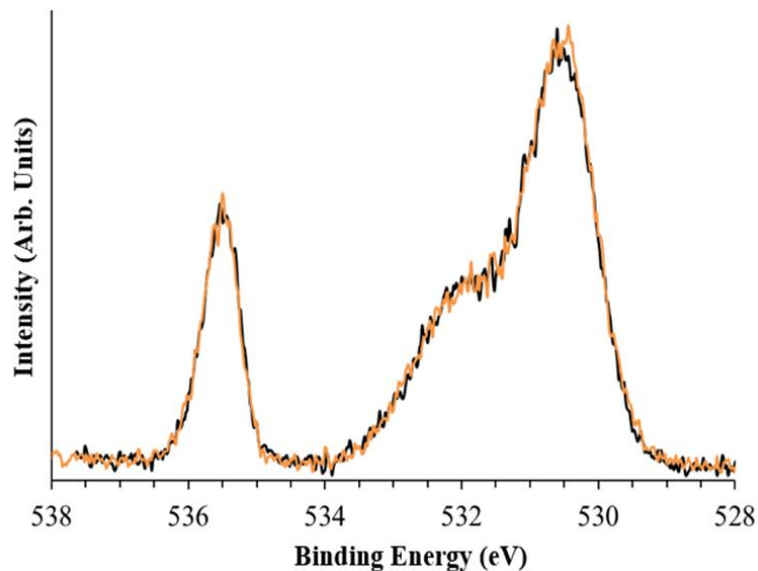


Figure 2.8: Two O 1s spectra collected consecutively at 0.4 Torr are shown in black and orange, respectively.

By contrast, uptake of water into the IL bulk can take many hours.⁸⁵ Figure 2.9 shows results of bulk water uptake into [C₄mim][Ace] measured gravimetrically as a function of time. The uptake was measured by incrementally increasing the RH by 1 % every five hours up to a maximum of 10 %. The mass increased by 13 % with water uptake still steadily increasing, indicating that bulk uptake of water is still far from saturation after 50 hours of absorption. These results further confirm that bulk and interfacial water uptake into [C₄mim][Ace] have different kinetics. The bulk water uptake is slow (on the order of many hours for milligrams of sample) while the interfacial water concentration rapidly approaches a steady state (on the order of minutes or less). These results suggest that the kinetics for uptake into the interfacial region is reversible and much more rapid than uptake into the bulk.

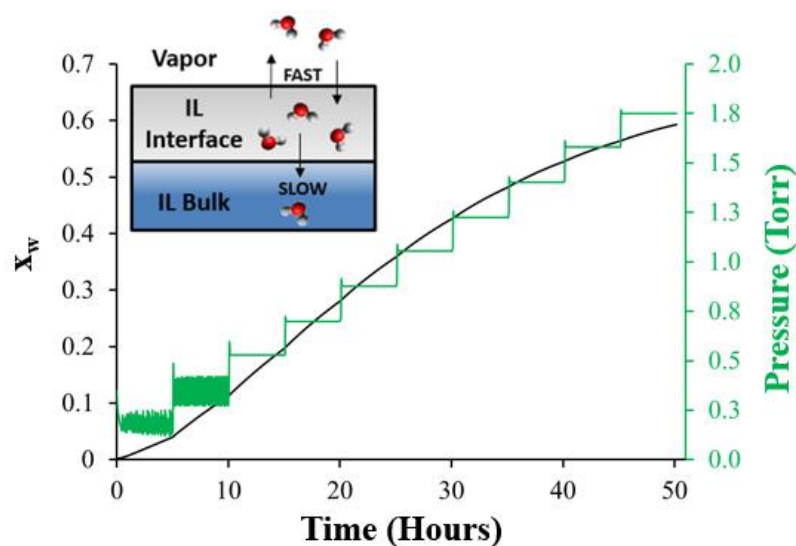


Figure 2.9: Gravimetric analysis of water absorption showing x_w (black) and water vapor pressure (green) as a function of time.

Experiments have focused on water sorption into ionic liquids and whether water sorption is into the bulk, onto the surface, or a combination of both. Deyko et al developed potential energy diagrams of water sorption into ionic liquids and showed an energy barrier for physisorbed surface water to adsorb within the ionic liquid underlayer (beyond the alkyl chain on the imidazolium cation) that is smaller than the rate of desorption into the gas phase.²⁶ Over time, the ionic liquid will diffuse into the bulk of the ionic liquid. Cao et al. studied bulk water sorption in several imidazolium cation ionic liquids and found the water sorption equilibrium into the bulk ionic liquid took several hours for hydrophilic ionic liquids and longer for more hydrophobic ionic liquids.⁸⁵ Similarly, Di Francesco et al studied water sorption of four hydrophobic ionic liquids and found water sorption equilibrium was not reached until several hours of exposure.⁸⁶ Recently, Chen et al used ATR-IR to describe the process of water

absorbed in [C₄mim][Ace] with bulk sorption on the order of hours followed by surface sorption.⁸⁷ Comparing the AP-XPS and gravimetric data, we have direct experimental evidence that the kinetics for water uptake into the interfacial region is reversible and much more rapid than uptake into the bulk as illustrated in the inset of Figure 2.9.

2.3 Interfacial Water Uptake at the Ionic Liquid-Gas Interface of 1-Ethyl-3-Methylimidazolium Borofluorate

2.3.1 Experimental Details

The AP-XPS experimental details are the same as Section 2.2.2. [C₂mim][BF₄] (Iolitec, 98%) has a melting point of 15 °C with a bulk density of 1.24 g cm⁻³.⁸⁸ The commercial IL was used as received without further purification and stored at room temperature in a vacuum desiccator. Samples were prepared for entry into the AP-XPS vacuum chamber by placing a thin film (< 0.3 mm thick, ~7 mm dia.) onto a 10 x 10 mm flame annealed Au foil (Alfa Aesar, 99.9975%, 0.25 mm thick). The sample holder was mounted and the AP-XPS spectroscopy chamber was pumped down overnight to a base pressure of 5 x 10⁻⁸ Torr prior to the start of the experiment.

Water vapor was introduced into the AP-XPS analysis chamber using a variable leak valve, behind which was a glass bulb containing 18.2 MΩ-cm water. Prior to the start of AP-XPS experiments the water was degassed via three freeze-pump-thaw cycles. The sample temperature was monitored using a type-K thermocouple near the Au foil. AP-XPS spectra were collected with the sample temperature held at 21.7 ± 0.1°C and constant water vapor pressures ranging from 10⁻⁶ to 2.5 Torr.

XPS spectra were analyzed using peak fitting software (CasaXPS, v2.3.16) with linear background subtraction and Gaussian-Lorentzian (70%-30%) peak fits. All XPS spectra were charge referenced to the C 1s alkyl peak with a binding energy (BE) of 285.0 eV.^{73,74} The C 1s alkyl peak was used as an internal reference for water-IL interactions due to it being the most common reference in literature. A description of individual peak fits will be discussed in Section 2.3.2.

2.3.2 High Resolution XPS Characterization Prior to Water Exposure

Prior to water exposure, XPS characterization of [C₂mim][BF₄] was performed. The survey spectrum, shown in Figure 2.10, was collected at 2.0x10⁻⁸ Torr. The spectrum contains B 1s, C 1s, N 1s, and F 1s which are all present in the chemical structure of the IL. One may also note that O 1s along with the O KLL auger peak are also present in the survey spectrum. The present oxygen is a contamination within the IL. As previously discussed, all ILs are hygroscopic meaning they will absorb even small amounts of water over time. For this reason, an oxygen contamination is not surprising. Attempts to remove this contamination were made including heating the sample up to 40 °C for several hours and pumping on the sample in high vacuum for several days. None of the attempts lead to a decrease in the amount of oxygen in the sample and the experiment progressed.

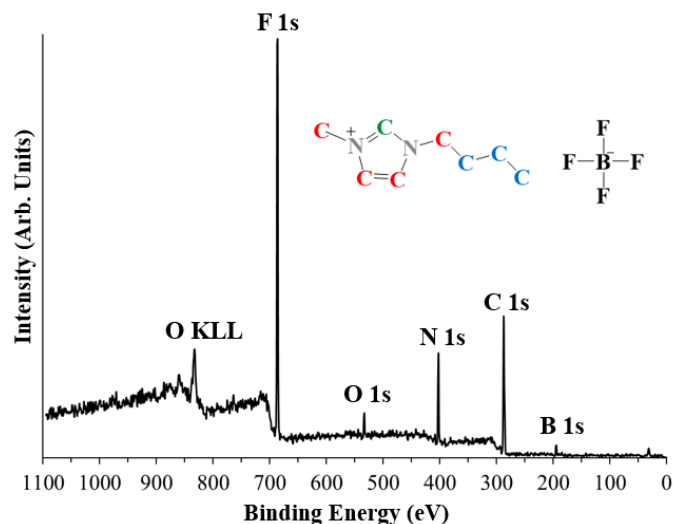


Figure 2.10: Survey spectrum of $[C_2mim][BF_4]$ collected at 2.1×10^{-8} Torr along with chemical structure.

The purity of the sample was also assessed by collecting high resolution spectra of all the elements present in the survey spectrum, shown in Figure 2.11. The C 1s spectrum (a) is fit with three components color coded to match the chemical structure in Figure 2.10. The C_{alkyl} , C_{ring} , and C_{ox} components are seen at 285.0, 286.5, and 287.3 eV. The peak area ratio of the C 1s components is 3:4:1 which matches the ratio in the chemical structure. The N 1s (b) and F 1s (c) spectra are both fit with one component and represent the nitrogen (401.9 eV) species on the imidazolium ring and the fluorine (686.0 eV) species on the anion, respectively. The B 1s, represents the boron on the anion, (d) is seen at 194.2 eV and is also fit with one component. The O 1s contamination is seen at 533.0 eV.

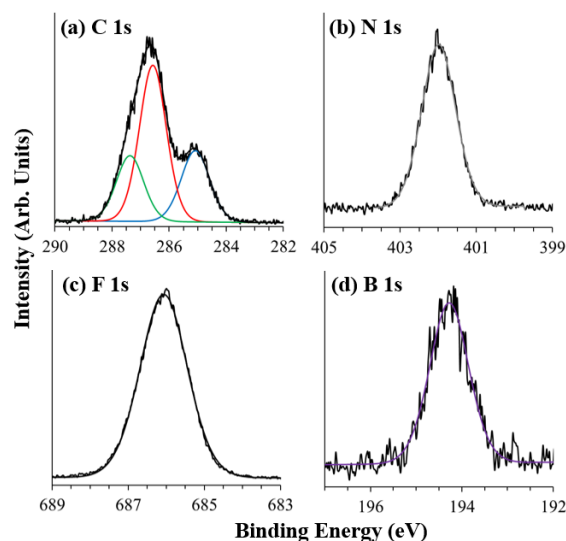


Figure 2.11: High resolution spectra of C 1s (a), N 1s (b), F 1s (c), and B 1s (d) for $[\text{C}_2\text{mim}][\text{BF}_4]$.

Analysis of the O 1s high resolution spectrum shows one oxygen species present at high vacuum. Again, it is believed that this contamination may be due to physisorbed water within the IL. Also, upon exposure to water vapor, the O 1s spectra did not show the addition of another interfacial water peak, showing that the initial peak in the high vacuum spectra is evidence of physisorbed water that does grow in the presence of increasing water vapor in the AP-XPS chamber.

2.3.3 Quantitative Assessment of Interfacial Water Uptake

Once the purity of $[\text{C}_2\text{mim}][\text{BF}_4]$ is confirmed, water is introduced into the chamber at an initial pressure of 1×10^{-6} Torr. Spectra is collected for all elements present in the IL in the following order: O 1s, C 1s, N 1s, F 1s, and B 1s. The water vapor pressure is continuously increased until the maximum water vapor pressure of 2.5 Torr is reached. At the end of the experiment, water is pumped out of the chamber

and spectra is collected in the same order to confirm the reversibility of the interfacial water uptake.

Unlike the [C₄mim][Ace] IL, [C₂mim][BF₄] does not contain an oxygen species in its chemical structure to directly calculate the water mole fraction. Instead, an element close to O 1s is chosen as the comparison, in hopes to limit the effects of gas phase attenuation. As previously discussed, the N_{ring} species has a binding energy of 401.9 eV while the O_w component has a binding energy of 533.0 eV. The measured kinetic energies of N_{ring} and O_w are 950 and 1080 eV, respectively. At these high kinetic energies, the gas phase attenuation is similar due to a very small electron scattering cross section between these two elements.⁸⁹

The kinetic energy (KE) of electrons from an average of the O 1s and N 1s orbitals using the Al K_α X-ray source is ~1015 eV. At this average KE, the inelastic mean free path (λ) of electrons escaping the interfacial region of [C₂mim][BF₄] is calculating to be 3.2 nm using the NIST software¹¹ with the Gries predictive formula and a bulk density (ρ) of 1.24 g cm⁻³ for [C₂mim][BF₄]. The thickness of one monolayer of IL is approximated using⁷⁵ $\rho^{-1/3}$, which is 0.64 nm for [C₄mim][BF₄]. Defining the sampling depth to be $3\lambda\cos(20^\circ)$, the calculated sample depth is 9.06 nm, which accounts for 95% of the signal from unscattered photoelectrons.⁷⁶

Due to fact that both the O 1s and N 1s are used in the water mole fraction equation, a sensitivity factor needs to be established. This sensitivity factor is established by the O 1s and N 1s species of the [C₄mim][Ace] that was previous collected on the lab-based AP-XPS system, due to it containing both elements in its chemical structure. This sensitivity factor ($S_{O\ 1s}/S_{N\ 1s}$) was measured to be 1.87. Now the water mole fraction can be calculated using:

$$x_w = \frac{1}{1 + \left(\frac{I_{N_{ring}}}{2I_w}\right)\left(\frac{S_{O_{1s}}}{S_{N_{1s}}}\right)} \quad (\text{Eqn 2.2})$$

Where $I_{N_{ring}}$ and I_w are the peak area of the N_{ring} and O_w components at each water vapor pressure. The factor of 2 is from the two moles of nitrogen present in the imidazolium cation to the one mole of oxygen in the water molecules. Using Eqn 2.2, the water mole fraction versus water vapor pressure can be calculated and is shown in Figure 2.12 for both $[C_4mim][Ace]$ (that was previously collected in blue) and $[C_2mim][BF_4]$ (red).

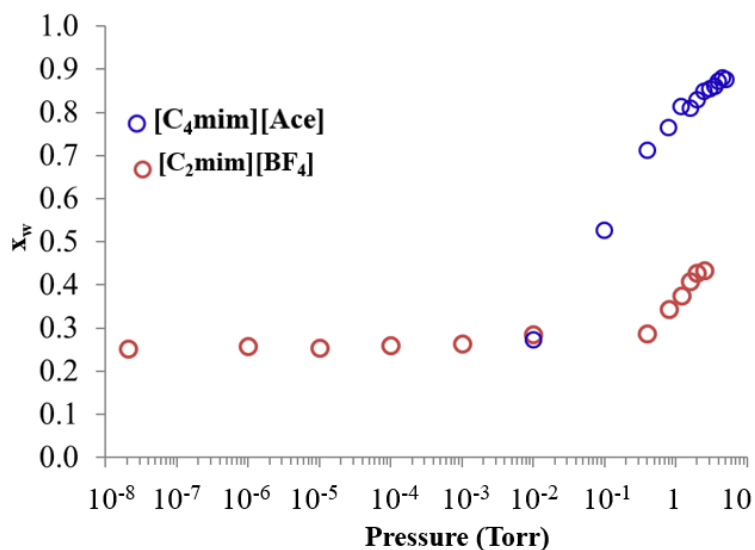


Figure 2.12: AP-XPS isotherm of water mole fraction (x_w) at the IL-vapor interface with water vapor pressure for $[C_4mim][Ace]$ (blue) and $[C_2mim][BF_4]$ (red).

In the $[C_2mim][BF_4]$ (red) isotherm, the initial contamination of water leads to a constant x_w of 0.26 from 10^{-8} Torr to 0.4 Torr. Then, the initial onset of water uptake for $[C_2mim][BF_4]$ is seen at 0.8 Torr, with an initial $x_w = 0.34$. This water

uptake continues to grow linearly, until a maximum $x_w = 0.44$ is reached at 2.5 Torr. As a comparison, the [C₄mim][Ace] isotherm is shown in blue. In this isotherm, the initial onset of water uptake occurs at 0.1 Torr, with $x_w = 0.53$. This isotherm also continues to increase linearly. At 2.5 Torr, the [C₄mim][Ace] isotherm reaches $x_w = 0.85$. This is more than double the amount of water uptake seen in the [C₂mim][BF₄].

This difference in water uptake has been seen in bulk water uptake studies with various anions and alkyl chain lengths on the imidazolium cation.^{85,90} Monitoring water uptake from ambient air, it was determined that an increase in the alkyl chain on the imidazolium cation leads to a decrease in water uptake.⁹⁰ Using gravimetric analysis, it has been shown that although the chain length does affect the water uptake, the biggest contributor to hydrophobicity is the anion.⁸⁵ In this comprehensive study, the [C₄mim]⁺ cation was studied with a variety of different anions including [Ace]⁻ and [BF₄]⁻. After exposure to water vapor with RH = 52% at room temperature, the water uptake decreased in the following order: [Ace] > [Cl] > [BF₄] > [NTf₂] > [PF₆]. With this, the [Ace]⁻ anion is known to be hydrophilic while the [BF₄]⁻ anion is considered hydrophobic. This agrees with our AP-XPS results and allows us to determine what ILs would be ideal candidates for water uptake via AP-XPS surface analysis.

Chapter 3

ENERGETICS OF INTERFACIAL WATER INTO ILS

3.1 Introduction

Ionic liquids (ILs) are molten salts with a melting point below 100°C. ILs are known as “designer solvents”, where different cations and anions can be combined to enhance their physical properties. For this reason, ILs are sparking interest in various applications including electrochemistry⁹¹, catalysis⁹², and gas absorption²¹. Both water and temperature can affect ionic liquid properties. All ILs are also hygroscopic and will absorb water over time.⁹³ Water absorption influences the physical properties of ionic liquids including density and viscosity.¹⁴ Varying the temperature of ionic liquids can lead to changes in IL bulk properties including conductivity, electrochemical window, viscosity, and density.⁹⁴⁻⁹⁶ As an example, AC impedance was used to measure the conductivity of 1-butyl-3-methylimidazolium bis(trifluoromethylsulfonyl)amide, [C₄mim][NTf₂], from 80-32 °C where an increase in temperature lead to a decrease in the ionic conductivity.⁹⁶ The density and viscosity as a function of temperature have been studied for various imidazolium based ionic liquids where both properties decreased with increasing temperature.^{94,95}

Surface sensitive techniques including temperature programmed desorption (TPD) and X-ray photoelectron spectroscopy (XPS) have been utilized to understand the effects of temperature on different IL properties.^{74,97-99} Using line of sight mass spectrometry (LOSMS) for TPD, the enthalpy of vaporization, ΔH_{vap} , has been measured for several ILs with imidazolium, pyrrolidinium, pyridinium and dicationic

cations between 138.85 - 294.85 °C. In addition, a model has been established to predict the enthalpies of other ILs.⁹⁷⁻¹⁰² The effect of temperature on surface enrichment of imidazolium ILs with varying chain length and anion have also been studied using AR-XPS demonstrating that increasing temperature from 26.85 °C to 126.85 °C leads to a decrease in surface enrichment of the imidazolium alkyl chain.⁷⁴ Krischok et al.¹⁰³ performed a comprehensive study examining structural changes of [C₂mim][NTf₂] from -173.15 to 346.85 °C using XPS, ultraviolet photoelectron spectroscopy (UPS), medium energy ion scattering spectroscopy (MIES), high resolution electron energy loss spectroscopy (HREELS) and density functional theory (DFT). At colder temperatures below -73.15 °C, the surface structure of the ionic liquid is drastically different than the bulk structure, where the molecules at the surface are more structured. The decomposition temperature under vacuum conditions was also determined. In addition, XPS of the C 1s spectra of [C₂mim][NTf₂] as a function of temperature shows a shift to higher binding energy at colder temperatures where surface charging is occurring.¹⁰⁴

Several studies have explored the effect of temperature on water sorption into ionic liquids. Using XPS, the heat of adsorption from -98.15 to 26.85 °C of water into 1-hexyl-3-methylimidazolium tetrafluoroborate, [C₆mim][BF₄], was determined.⁶ Additionally, heating the sample lead to a change in the N 1s spectra where an additional peak associated with x-ray damage appears at lower binding energy. Most studies have used a solution of ionic liquid and water to determine the enthalpy of mixing for a variety of ionic liquids.¹⁰⁵⁻¹⁰⁹ Only a few studies have looked at the enthalpy of absorption between water vapor and the ionic liquid.^{110,111} Anthony et al. used gravimetric analysis to study water uptake in three ionic liquids and found the

enthalpy of absorption (ΔH_{abs}) from 10 to 50 °C was similar to the enthalpy of absorption of water into polar solvents like 2-propanol.¹¹⁰ Takamuku et al. used gravimetric analysis to measure the absorption and desorption of water on [C₂mim][BF₄] from 9.85 to 29.85 °C.¹¹¹ Using differential scanning calorimetry (DSC), the number of water molecules per ion pair was determined to be 7:1, where the hydration number decreases at higher temperatures.¹¹² Water solubility in pyridinium-based ionic liquids found that solubility increases with temperature from 20.35 to 70.52 °C. It has been shown using gravimetric analysis that the water uptake in [C₄mim][BF₄] and [(allyl)mim][Cl] has a higher sorption capacity and rate at higher temperatures due to the change in viscosity.^{85,93}

In this section, we use ambient pressure X-ray photoelectron spectroscopy (AP-XPS) to study the influence of temperature on water uptake at the IL-gas interface of [C₄mim][Ace] and [C₄mim][Cl]. Using the Clausius-Clapeyron equation, the enthalpy of interfacial water uptake has been determined from $0.4 < x_w < 0.85$. Spectra changes are seen in the C 1s as a function of water vapor and with an earlier onset of these changes at warmer temperatures. In addition, binding energy shifts follow the same trend with each isotherm, with the largest shift occurring at colder temperatures (associated with most water uptake).

3.2 Experimental

1-butyl-3-methylimidazolium acetate [C₄mim][Ace] (Ioletic, 98%) has a melting point of -20 °C.⁷² 1-butyl-3-methylimidazolium chloride [C₄mim][Cl] (Fluka, 99%) has a melting point of 65 °C.¹¹³ It should be noted that the synthesis of [C₄mim][Cl] results in a viscous yellow liquid at room temperature and goes through a crystallization process using previous [C₄mim][Cl] microcrystals to obtain a solid

IL.¹¹³ It should also be noted that many experiments have used $[\text{C}_4\text{mim}][\text{Cl}]$ at room temperature in the liquid form.^{114,115} During our study, $[\text{C}_4\text{mim}][\text{Cl}]$ was a viscous liquid from 0 -20 °C. The commercial ILs were stored in a vacuum desiccator at room temperature and used as received without further purification. Samples were prepared for entry into the vacuum chamber under laboratory conditions by removing from the vacuum desiccator and spreading a small thin film of < 0.1 mm thick onto a 10 x 10 mm flame annealed Au foil (Alfa Aesar, 99.9975%, 0.25 mm thick) which was attached on the AP-XPS sample holder. The sample holder was mounted and the AP-XPS spectroscopy chamber was pumped down with a mechanical pump. The sample was then pumped overnight using a turbo pump. Figure 3.1 shows a picture of both samples $[\text{C}_4\text{mim}][\text{Ace}]$ (a) and $[\text{C}_4\text{mim}][\text{Cl}]$ (b) in the AP-XPS chamber at 10 °C prior to water exposure. Both IL droplets appear as viscous liquids and remain liquids during the duration of the experiment.

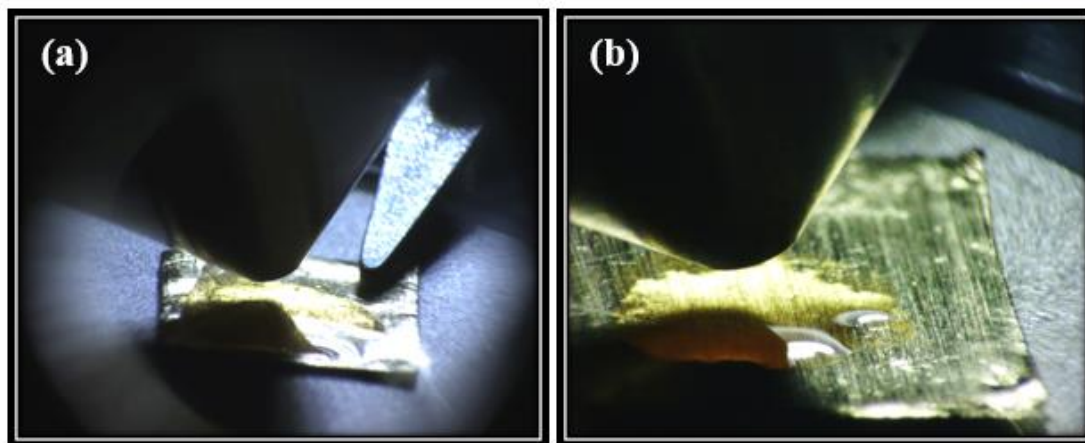


Figure 3.1: Images of $[\text{C}_4\text{mim}][\text{Ace}]$ (a) and $[\text{C}_4\text{mim}][\text{Cl}]$ (b) deposited on Au foil in the AP-XPS chamber under vacuum conditions at 10 °C prior to water exposure.

AP-XPS experiments of the IL-water vapor interface for both [C₄mim][Ace] and [C₄mim][Cl] were conducted using a lab-based system with a Scienta MX650 monochromatic Al anode X-ray source operating at 200 W (20 mA, 10 kV) and a Scienta HIPPI-2 differentially pumped electron energy analyzer. The details for this system have been described previously.¹³ Experiments were performed using a 0.5 mm aperture and acceleration capture lens mode. A glass bulb containing 18.2 MΩ-cm water (ELGA, MEDICA-R 7/15) and a variable leak valve were used to introduce water vapor into the chamber. Prior to experiments, the water was degassed via three freeze-pump-thaw cycles. The sample temperature was monitored using a type-K thermocouple near the Au foil. AP-XPS spectra for each isotherm were held at constant temperature using a circulating chiller (Reslab, RTE-140) and constant pressure ranging from 10⁻⁷ to 5.0 Torr. XPS spectra were analyzed using peak fitting software (CasaXPS 2.3.16 PR1.6) with linear background subtraction and Gaussian (70%) and Lorentzian (30%) peak fits. All spectra were referenced to the C 1s alkyl peak on the imidazolium cation with a binding energy of 285.0 eV.⁷³

In the initial experiment with [C₄mim][Ace] and water, survey spectra were captured at 200 eV pass energy while C 1s, N 1s, and O 1s were captured at 100 eV pass energy. The probing depth is defined as 3*IMFP*cos(20°), where our AP-XPS is probing ~ 12 layers of ionic liquid and electrons have an IMFP of ~ 3.026 nm for [C₄mim][Ace] based on the O 1s electrons.³⁷ The five isotherms were collected at 0.1 ± 0.4 °C, 10.2 ± 0.3 °C, 21.7 ± 0.1 °C, 32.2 ± 0.3 °C, and 42.4 ± 0.5 °C. The isotherms were collected in the following order: 22 °C, 32 °C, 42 °C, 10 °C, and 0 °C. Evidence of beam induced damage was noted in the N 1s spectra at the two coldest isotherms

and enhanced at the surface in the presence of water. The fittings of the C 1s, N 1s, and O 1s have been described previously.³⁷

In the second experiment with [C₄mim][Cl] and water, survey spectra were captured at 200 eV pass energy while C 1s, N 1s, Cl 2p, and O 1s were captured at 100 eV pass energy. The probing depth is defined as $3 \cdot \text{IMFP} \cdot \cos(20^\circ)$, where our AP-XPS is probing ~ 12 layers of ionic liquid and electrons have an IMFP of ~ 3.026 nm for [C₄mim][Ace] based on the O 1s electrons.³⁷ The four isotherms were collected at -0.1 ± 0.4 °C, 10.1 ± 0.2 °C, 20.4 ± 0.2 °C, and 30.5 ± 0.3 °C. The isotherms were collected in the following order: 0 °C, 10 °C, 20 °C, and 30 °C. The fittings of the C 1s, N 1s, Cl 2p, and O 1s will be discussed in Section 3.4.

The gravimetric data was collected using a Hiden Isochema IGA-sorp microbalance that can accurately perform sorption measurements through temperature and relative humidity control. This balance uses nitrogen as a carrier gas to create the necessary environment around the sample. Unlike the AP-XPS experiment that uses pure water vapor as the gas, the gravimetric analysis uses a nitrogen carrier gas with water vapor which requires the pressure data to be presented in partial pressure of water.

The [C₄mim][Ace] sample used for the gravimetric studies was purchased from Sigma Aldrich and has a purity of > 95%. Prior to analysis, the IL was dried under vacuum at 50 °C for 7 days. Using Karl Fischer analysis, the final water content in the sample was determined to be 0.22 wt%. Approximately ~56 mg of the IL was then loaded into a Pyrex bulb and set onto the IGA-sorp. The sample was then further dried in a stream of dry nitrogen at 250 mL/min for 15 hours at 75 °C. This pretreatment in the IGA-sorp was completed before each isotherm. Three isotherms

were collected at 21.7 ± 0.02 °C, 30.0 ± 0.01 °C, and 42 °C ± 0.02 . Lower isotherms at 0 and 10 °C could not be collected due to instrument limitations.

3.3 Energetics of Water Sorption at the 1-Butyl-3-Methylimidazolium Acetate–Gas Interface

3.3.1 Relative Humidity Dependent Interfacial Water Uptake

To confirm the purity of [C₄mim][Ace], a survey was taken before each isotherm. The survey spectra contained C 1s, N 1s, and O 1s which are present in the chemical structure of [C₄mim][Ace]. XPS spectra was collected for each element at every pressure from vacuum to 5.0 Torr. The isotherm at 0 °C could only be collected up to 2.5 Torr, due to instrumentation limitation.

The O 1s spectra at vacuum for each temperature is shown in Figure 3.2 (a). The spectra are color coded throughout accordingly: purple - 42 °C, green - 32 °C, blue - 22 °C, red - 10 °C and black - 0 °C. At vacuum, one component, O_{Ac}, is seen at 530.4 eV. The presence of one component in the O 1s spectra at the same binding energy for every temperature further confirms the purity of the sample at the start of each experiment. AP-XPS experiments were then conducted by exposing the IL to water vapor as a function of pressure. At water vapor pressures $< 10^{-2}$ Torr, only one component, O_{Ac}, is present in the O 1s spectra. At 10^{-2} Torr, a small peak, interfacial water (O_w), is seen at 531.6 eV. At 10^{-1} Torr, gas phase water above the sample (O_{gas}) appears at 535.6 eV. Both species continue to grow as more water is introduced into the chamber, up to a total pressure of 5.0 Torr. Figure 3.2 (b) shows the O 1s spectra at 2.5 Torr for each isotherm containing O_{Ac}, O_w, and O_{gas} components. To compare the spectra as a function of temperature, the spectra collected at 2.5 Torr were normalized

to the O_{gas} component. At 2.5 Torr, the O_{w} component shows qualitative growth with decreasing temperature from 42 °C to 0 °C. There is also a shift in the O_{w} and O_{gas} component to higher binding energy as function of decreasing temperature. The O_{Ac} component also shifts to higher binding energy as a function of decreasing temperature. In addition, the insert in Figure 3.2 (b) shows the O 1s spectra at 5.0 Torr zoomed in on the O_{Ac} and O_{w} components at temperatures of 10, 22, 32, and 42 °C. Here, one can see a small amount of water, O_{w} , at 42 °C while the spectra collected at 10 °C shows a more pronounced O_{w} . In addition, the O 1s spectra collected at 22 °C is only slightly enhanced compared to the spectra at 32 °C.

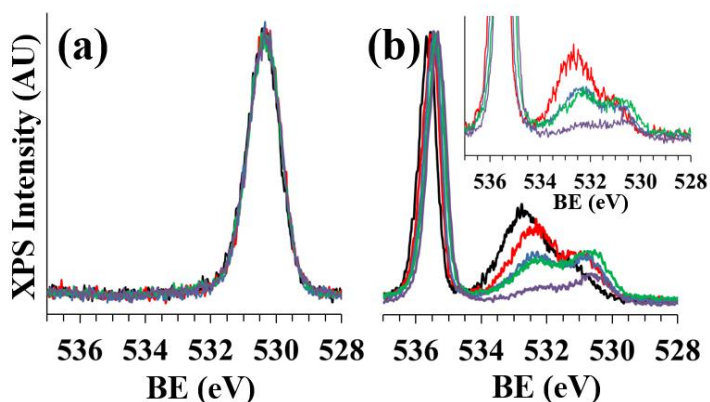


Figure 3.2: O 1s at (a) vacuum and (b) 2.5 Torr from 0-42 °C, where O_{gas} and O_{w} shift to higher binding energy as a function of decreasing temperature. Inset shows zoomed-in spectra collected at 5.0 Torr from 10-42 °C. Color Code: purple - 42 °C, green - 32 °C, blue - 22 °C, red - 10 °C, and black - 0 °C

Assuming the ionic liquid and interfacial water is a homogenous mixture, the water mole fraction (x_w) can be calculated from O 1s peak areas (I) of O_w and O_{Ac} by using the following equation:

$$x_w = \frac{n_w}{n_w + n_{IL}} = \frac{I_w}{I_w + \frac{I_{IL}}{2}} \quad (\text{Eqn 3.1})$$

Where n_w and n_{IL} are the moles of water and IL, respectively, $I_w \propto n_w$ (one mole of oxygen per water) and $I_{IL} \propto 2n_{IL}$ (two moles of oxygen per acetate anion).

The interfacial water uptake curves from 0 to 42 °C as a function of pressure are shown in Figure 3.3 (a). The room temperature uptake (blue) was collected previously.³⁷ The uptake curves show [C₄mim][Ace] uptakes more water at colder temperatures, which agrees with the qualitative assessment of the O 1s spectra as a function of water vapor pressure discussed in Figure 3.2. The dashed line through each isotherm represent an empirical fit with $R^2 > 0.99$ for all isotherms. For all isotherms, there is a steep onset of water uptake at pressures between 10^{-2} Torr and 10^{-1} Torr. Each isotherm continues to grow with increasing water vapor exposure. At the maximum water exposure of 2.5 Torr, the isotherm at 0 °C uptakes $x_w = 0.90$. The amount of water molecules per ionic liquid pair were also calculated by using the O 1s peak intensity of the acetate ion (O_{Ac}) and interfacial water (O_w). At the coldest isotherm of 0 °C and $x_w = 0.90$, there are ~ 10 water molecules per ionic liquid pair. As a comparison, the warmest temperature of 42 °C uptakes $x_w = 0.64$ at 2.5 Torr and $x_w = 0.72$ at the maximum water vapor pressure of 5.0 Torr. At the warmest isotherm of 42 °C, there are ~ 3 water molecules per ionic liquid pair.

The amount of water uptake as a function of temperature depends on two factors, the change in viscosity of the ionic liquid as a function of increasing temperature leading to faster diffusion of water and the thermodynamics of water

evaporation as a function of increasing temperature.^{85,93} In $[C_4mim][Ace]$, increasing temperature leads to less water uptake within the interfacial region. This infers that water evaporation with increasing temperature plays the largest role in water uptake into $[C_4mim][Ace]$.

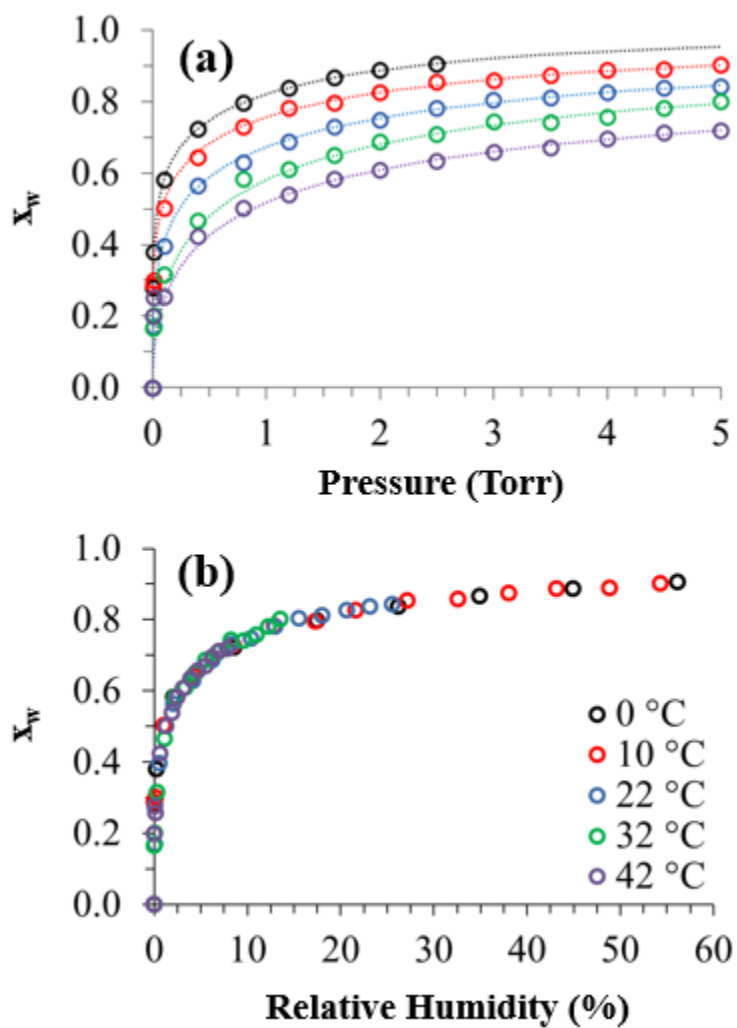


Figure 3.3: Isotherms from 0 - 42 °C of water uptake into $[C_4mim][Ace]$ as a function of pressure (a) and relative humidity (b).

The pressure was converted to percent relative humidity (%RH) for all temperatures in Figure 3.3 (b). There is a steep growth in RH between 0 - 6%. The RH continues to grow with increasing water mole fraction. The warmest isotherm at 42 °C reaches a maximum RH ~ 7.9 % at 5.0 Torr. In comparison, the coldest isotherm at 0 °C, reaches a maximum RH ~ 56.1 % at 2.5 Torr. Even with the drastic difference in water uptake as a function of temperature for all isotherms, the isotherms converge when converted to % RH to show one uptake curve. An overlap in relative humidity of all isotherms confirms that the interfacial water uptake only depends on the water vapor pressure from 0 - 42 °C. These results agree with previous results that measured the water absorption of [C₂mim][BF₄] from 283 - 303K.¹¹¹

Not only does water uptake change with temperature, but the kinetics of water uptake into the interfacial region is drastically different from the bulk absorption. Interfacial water uptake into [C₄mim][Ace] is rapid and reversible compared to bulk water uptake using gravimetric analysis.³⁷ Comparing [C₄mim]⁺ cation with a variety of anions, Cao et. al.⁸⁵ showed the bulk water uptake into [C₄mim][Ace] at RH = 52% reached a water sorption capacity (W) of 15.63 after 3 hours. Using a two-set model, the water sorption capacity of [C₄mim][Ace] was 24.24, proving that the saturation point of water into the bulk [C₄mim][Ace] regime, was not reached after three hours. On the other hand, AP-XPS O 1s spectra indicates water uptake is at equilibrium in the interfacial region after ~11 minutes. Additionally, the reversibility of water uptake into the interfacial region at all temperatures was investigated. After each isotherm, water was pumped out of the chamber and the O 1s spectra was immediately collected. Independent of temperature, the O_{Ac} is the only component present in the O 1s spectra, confirming the reversibility of the water uptake in the interfacial region regardless of

temperature. The reversibility of water uptake into [C₄mim][Ace] at room temperature has been previously discussed.³⁷

3.3.2 Water Induced Changes in the Electronic Environment

In our previous work, spectral shifts were observed as a function of increasing water vapor pressure. To assess the magnitude of the core level BE shifts relative to each other, we compared relative BE shifts (BE) given by $BE = BE_{amb} - BE_{vac}$, where BE_{amb} is the BE in the presence of water and BE_{vac} is the BE under vacuum. The C_{alkyl} component was chosen as the internal reference due to it being the most common reference in UHV XPS literature and it is the most hydrophobic species within the ionic liquid and should be the least sensitive to a water induced chemical shift.³⁷

Figure 3.4 shows a plot of binding energy shifts relative to the C_{alkyl} component at 0 °C (closed circles) and 42 °C (open circles). Each component is represented by a different color where O_w is purple, O_{Ac} is black, C_{ox} is green, C_{ring} is red, and N_{ring} is gray. Both isotherms in Figure 3.4 show the same trend in components with shift from largest to smallest in the following: O_w > O_{Ac} ≈ C_{ox} > C_{ring} > N_{ring}. At low water vapor pressures > 10⁻¹ Torr, minimal shifting is seen in each component. The magnitude of the shift is drastically different when comparing cold and warm temperatures. At the colder isotherm of 0 °C (open circles), there are large component shifts as a function of water vapor. The 42 °C isotherm (open circles) shows a smaller magnitude in the component shift. As an example, the O_w component at 0 °C shifts ~ 1.18 eV and at 42 °C shifts ~ 0.56 eV. Meanwhile, the N_{ring} component at 0 °C shifts ~ 0.09 eV and at 42 °C shifts ~ 0.01 eV. In summary, the warmest isotherm at 42 °C shows relatively small shifts compared to the coldest isotherm at 0 °C.

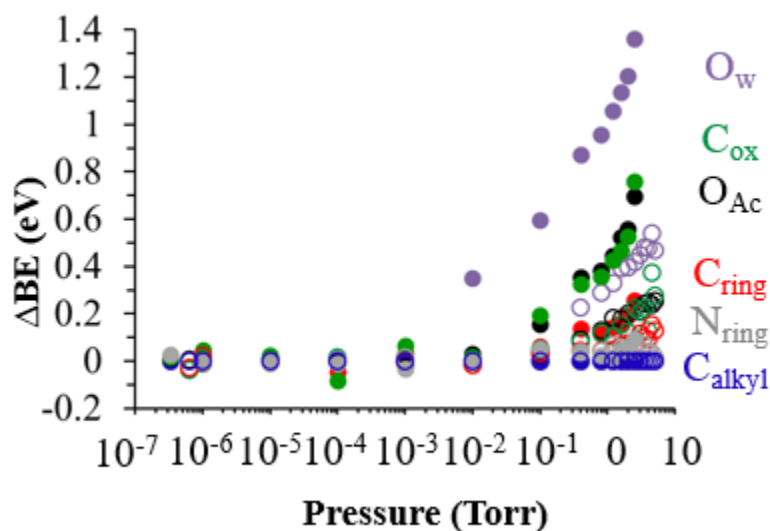


Figure 3.4: Binding energy shifts relative to C_{alkyl} for all components as a function of pressure at 0 °C (closed circles) and 42 °C (open circles). All components follow same shifting trend at both temperatures.

As discussed in our previous publication, the observed BE changes show water is significantly influencing the electronic environment of both the cation and anion at the IL-vapor interface. The difference in binding energy shift with temperature is due to the amount of water present at the interfacial region. As in Figure 3.3 (a), there is less interfacial water uptake at warmer temperature leading to a smaller shift in the components, as shown in Figure 3.4.

The shift of all components relative to the C_{alkyl} component as a function of % RH are shown in Figure 3.5. Each shape represents a different temperature where diamond is 0 °C, triangle is 10 °C, circle is 22 °C, square is 32 °C, and square with X is 42 °C. A congregation between each component (color) regardless of the temperature is seen where the trend from largest to smallest shift is the following: O_w

$> O_{Ac} \approx C_{ox} > C_{ring} > N_{ring}$. This congregation is further evidence that the shifting is due to water uptake into the ionic liquid. The order of the shift also agrees with our previous room temperature data.³⁷

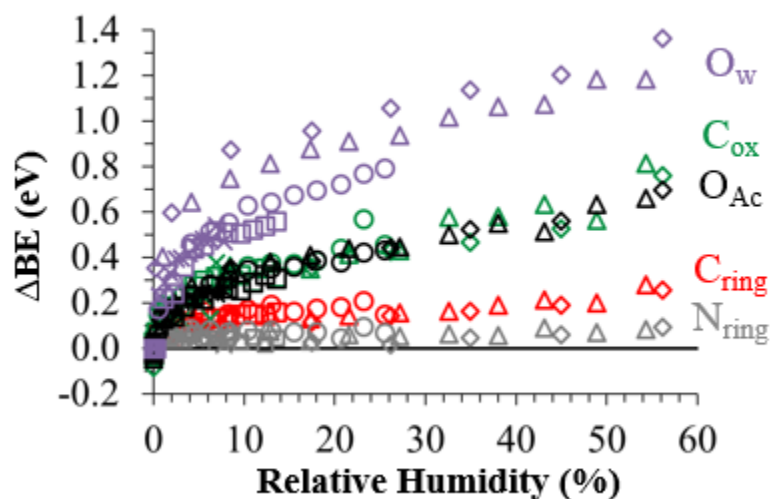


Figure 3.5: Binding energy shift relative to C_{alkyl} for all components and temperature. Color Code: blue= O_w , green= C_{ox} , black= O_{Ac} , red= C_{ring} , gray= N_{ring} ; Symbol Code: diamond= 0 °C, triangle= 10 °C, circle= 22 °C, square= 32 °C, square with cross= 42 °C.

As discussed previously, it has been shown using density functional theory (DFT) that water significantly impacts the electronic environment of each moiety⁷⁷ and have been calculated for pure ionic liquids.¹¹⁶ To understand the magnitude of these shifts as a function of water vapor pressure as well as temperature, DFT core level shift studies are strongly needed.

3.3.3 Water Induced Structural Changes

In addition to quantitatively assessing the interfacial water uptake as a function of temperature, we assessed other elemental changes as a function of temperature. An overlay of the C 1s spectra prior to water exposure at each temperature is shown in Figure 3.6. The C 1s spectra shows a peak that contains three components C_{alkyl} , C_{ring} , and C_{ox} at 285.0, 286.2, and 287.3 eV, respectively. The fitting of the C 1s spectra has been previously discussed.³⁷ The C_{alkyl} and C_{ox} components contain carbon atoms on both the cation and anion. The C_{ring} component only contains atoms on the imidazolium ring. At vacuum in Figure 3.6 (a), all C 1s spectrum overlap regardless of temperature, showing a peak ratio analysis of 4:4:2 for $C_{\text{alkyl}}:C_{\text{ring}}:C_{\text{ox}}$. Along with the initial survey spectrum and O 1s spectra of the ionic liquid, the ratio is further confirmation of the purity of [C₄mim][Ace] at the beginning of each experiment.

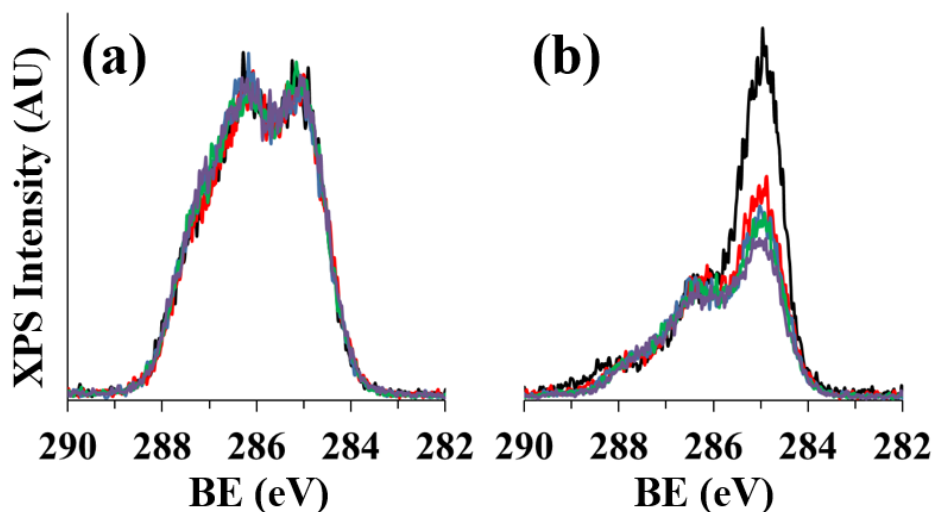


Figure 3.6: C 1s at (a) vacuum and (b) 2.5 Torr from 0 - 42 °C, normalized to C_{ring} component and calibrated to C_{alkyl} at 285 eV. Color Code: purple – 42 °C, green – 32 °C, blue – 22 °C, red – 10 °C, and black – 0 °C.

The C 1s collected at 2.5 Torr is shown in Figure 3.6 (b). To make a visible comparison, all spectra were normalized to the C_{ring} component (center component). The C_{ox} component (highest binding energy) shows a small shift to higher binding energy at colder temperatures (black spectrum). There is also a drastic change in the C_{alkyl} component as a function of temperature. The C_{alkyl} component grows with decreasing temperature. This change in the carbon spectra as a function of temperature is due to a difference in %RH at each temperature with the smallest RH ~ 3.9% at 42 °C and largest RH ~ 56.1% at 0 °C. At larger %RH, more interfacial water is present in the [C₄mim][Ace]. This qualitatively change in the AP-XPS spectra as a function of water shows water is effecting the carbon atoms of [C₄mim][Ace].

Further assessment of growth in C_{alkyl} as a function of temperature yields interesting results. An assessment of the C_{alkyl} peak intensity (I_{alkyl}) to the total C 1s signal (I_{C1s}) as a function of number of water molecules per ionic liquid pair (n_w/n_{IL}) is shown in Figure 3.7. The C_{alkyl} growth has a sudden onset at 2.0 water molecules per IL pair for isotherms < 22 °C which is equivalent to x_w ~ 0.6. The C_{alkyl} growth occurs sooner at ~ 1 n_w/n_{IL} for isotherms warmer than 22 °C, beginning at x_w ≈ 0.5 for 32 °C and x_w ≈ 0.4 for 42 °C. After the sudden onset, the C_{alkyl} growth continues to grow with increasing water molecules. This onset continues to grow to a maximum of I_{alkyl}:I_{C 1s} ~0.70 at x_w = 0.9 for both 0 °C and 10 °C, or 10 water molecules per IL pair.

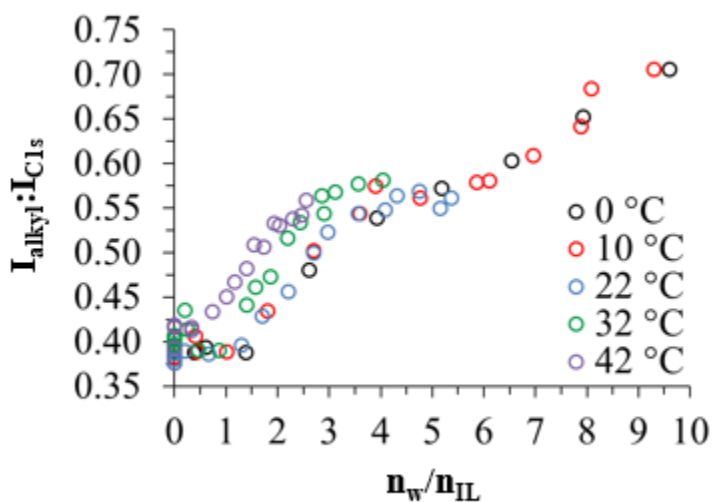


Figure 3.7: Ratio of C_{alkyl} intensity to total C 1s intensity as a function of water mole fraction (x_w) for each isotherm

The sudden onset of C_{alkyl} growth is indication of water induced nanostructuring or the possibility of adventitious carbon with water vapor pressure, although the latter case is unlikely.¹¹⁷ The nanostructuring within the interfacial region leads to a network of polar regions (water, acetate, and imidazolium ring) and nonpolar regions (imidazolium alkyl chain) as evidenced from MD simulations and neutron scattering of IL-water bulk mixtures.⁸²⁻⁸⁴ Literature has also shown long range ordering in ionic liquids with a thickness up to $\sim 2 \mu\text{m}$.^{118,119}

Small-angle neutron scattering (SANS) has been used to study $[\text{C}_4\text{mim}][\text{BF}_4]$ - H_2O mixtures at different water mole fractions.⁸³ At low x_w , the water dissolves homogeneously into the ionic liquid. At $x_w > 0.7$, water begins to form nanometer-sized clusters. These results were further confirmed from a Molecular Dynamic (MD) simulation of $[\text{C}_4\text{mim}][\text{BF}_4]$ and water mixtures, where large water clusters are formed

at $x_w > 0.8$.⁸⁴ Recently, a MD simulation study of imidazolium acetate-water mixtures observed similar nanostructuring phenomenon. For the [C₄mim][Ace], a sudden IL density change was seen at $x_w \sim 0.7$. This change is due to nanostructuring of polar and nonpolar regions. Both studies confirm the unique nanostructuring in imidazolium ionic in the presence of water. To the best of our knowledge, we are the first to assess the nanostructuring between IL and water as a function of temperature.

Based on the previous discussion, we believe the enhancement of C_{alkyl} as a function of water is due to nanostructuring within the interfacial region. Within our probing depth of a few nanometers, we are seeing nanostructuring of hydrophobic nanometer size structures at $x_w > 0.6$ for temperatures < 22 °C. Our results also suggest that above room temperature, as the IL temperature increases, the nanostructuring will begin at a lower water mole fraction. This interfacial nanostructuring has significant implications for the uptake of other gases including CO₂ and SO₂, where the gas molecules must pass through the IL-vapor interface. MD simulations investigating this nanostructuring as a function of temperature are needed to assess these observed deviations at warmer temperatures.

3.3.4 Energetics of Interfacial Water Uptake

An empirical fit was generated for the uptake curves in Figure 3.3 (a). The empirical fit used is given by: $p = (x_w)^a/(1-x_w)^b$, where p is the pressure, x_w is the water mole fraction, and a, b are variables that change for each isotherm. To determine the enthalpy of interfacial water uptake, ΔH , for this process, we used the Clausius-Clapeyron equation where relates temperature and vapor pressure of water:

$$\Delta H = \bar{h}_1 - h_1^{ig} = RT \left(\frac{\delta \ln x_1}{\delta \ln T} \right)_p \left(\frac{\delta \ln \alpha_1}{\delta \ln x_1} \right)_{p,T} \quad (\text{Eqn 3.1})$$

Where ΔH is the enthalpy of interfacial water uptake, \bar{h}_1 is the partial molar enthalpy, h_1^{ig} is the enthalpy of pure water in the ideal gas phase, and α_1 is the activity of water in the solution.¹¹⁰

The enthalpy of interfacial water uptake into [C₄mim][Ace] from $0.40 < x_w < 0.75$, along with a dashed line for the enthalpy of vaporization for bulk water at 20 °C are shown in Figure 3.8. The generated plot shows a change in the slope of enthalpy of interfacial water uptake (ΔH) that can be related to interfacial water uptake into [C₄mim][Ace]. First, the enthalpy of interfacial water uptake shows a linear relation up to $x_w \sim 0.7$. When interfacial water uptake first occurs into the ionic liquid, the enthalpy of interfacial water uptake is most favorable and below the enthalpy of vaporization for bulk water. At these low water concentrations, water is interacting strongly with the acetate and most acidic carbon of the imidazolium ring. At $x_w > 0.7$, the enthalpy of interfacial water uptake begins to converge to the enthalpy of vaporization for bulk water at 20 °C ($\Delta H_{\text{vap}} = -43.99 \text{ kJ.mol}$). The initial change in slope at $x_w \sim 0.7$ is likely related to a phase transition, from water-anion interactions to water-water interactions. It may also be evidence of nanostructuring within the interfacial region of polar and nonpolar regions which will be discussed in the latter sections.

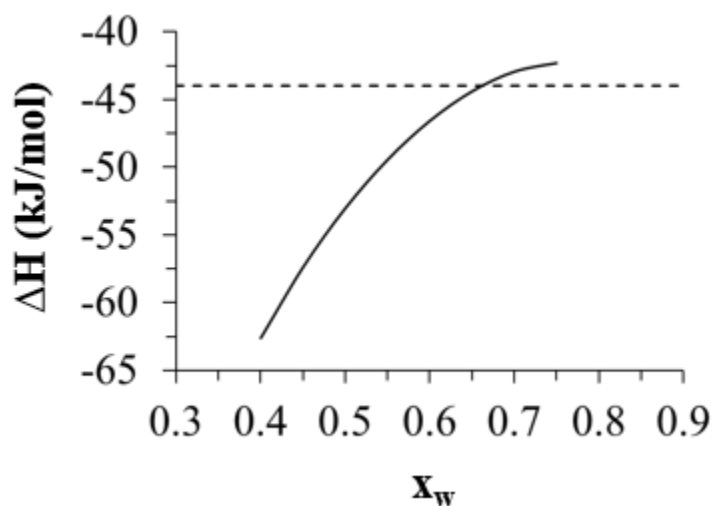


Figure 3.8: Enthalpy of interfacial water uptake from $0.4 < x_w < 0.75$.

There is a lot of literature on the enthalpy of mixing, ΔH_{mix} , of water and ionic liquids (liquid-liquid)^{106,120-122} and very little on the enthalpy of vaporization of water vapor and ionic liquid (liquid-gas)^{6,110,111}. The enthalpy of mixing has been determined for a range of cations and anions including imidazolium, pyridinium, and piperidinium cations with anions of various hydrophilicities. On the contrary, the liquid-gas energetics between water and ionic liquids have been explored for imidazolium cations with the $[\text{PF}_6]$ and $[\text{BF}_4]$ anions.^{24,25} In addition, UHV XPS has shown different energetics between the heat of adsorption compared to the heat of absorption of water on a solid ionic liquid surface.⁶ More data is needed to generate a better understanding about the energetics at the gas-liquid interface of ionic liquids.

3.3.5 Interfacial Versus Bulk Energetics of Water Sorption

While the initial assessment of the energetics at the interfacial region is very valuable, we wanted to be able to compare our results to the bulk region. To do so, we

worked with the Dr. Mark Shifflet's research group from the University of Kansas. The group was able to do a bulk water uptake experiment on [C₄mim][Ace] within the same temperature and relative humidity range as the AP-XPS data. With this, a direct comparison between the interfacial and bulk region can be processed.

One thing worth noting is the longevity of each gravimetric isotherm. Table 3.1 shows an example of each data point collected to form the isotherm at 21.7 °C. The initial data point at RH = 0 % took the longest to collect at ~ 7 days. This is due to the initial drying of the IL, to obtain a small water concentration determined by Karl Fischer to be 0.22 % wt. After this initial data point, all points collected took approximately 1 – 2.5 days to equilibrate. Using gravimetric analysis, one complete uptake isotherm takes approximately 11 days to collect. The desorption time at the same % RH took slightly longer. For example, the water uptake at RH = 15 % took 1 day to equilibrate while the desorption at this RH took 1.3 days. In total, one absorption and desorption experiment could take several weeks to complete. On the contrary, an AP-XPS experiment can be completed within 1 day depending on the amount of data collected.

Table 3.1: Longevity of Each Gravimetric Data Point for Isotherm at 21.7 °C

% RH	Equilibration Time (days)
0	7
1	2.6
5	2
10	1
15	1
20	1.4
25	1

Both bulk water absorption and desorption curves are shown in Figure 3.9 (a). The overlapping of the results confirms the water-ionic liquid interactions are purely physical. The bulk uptake depicts a similar behavior as the interfacial absorption, where the highest water concentration is observed at the lowest isotherm in the system, 21.7 °C. An empirical equation ($R^2 > 0.99$) is fit to the gravimetric data, as depicted by the dashed lines at each isotherm. The higher temperature curves appear to plateau at lower partial pressures of water, therefore suggesting a lower bulk water sorption capacity at higher temperatures for the 21.7 °C to 42 °C range. Partial pressures higher than 5.0 Torr are achieved with the gravimetric balance. This is possible as the IGA sorp operates at ambient pressure (~760 Torr) and is set to reach 25 % RH for all isotherms, where the partial pressure of water at 25 % RH and 42°C is ~ 15.4 Torr. At 21.7 °C, the maximum water partial pressure is 4.87 Torr and the system achieves its highest water uptake: $x_w = 0.78$. The ratio of water molecules to IL pair molecules at 21.7 °C and $x_w = 0.78$ is about 3.5, whereas at 42 °C and a water partial pressure of 4.87 Torr, the ratio is ~ 1.77. However, at the 42 °C isotherm and its highest water exposure (~ 15.4 Torr), the molecule ratio is ~ 3.4, which indicates that hydration capacities at differing temperatures are similar at equal relative humidities.

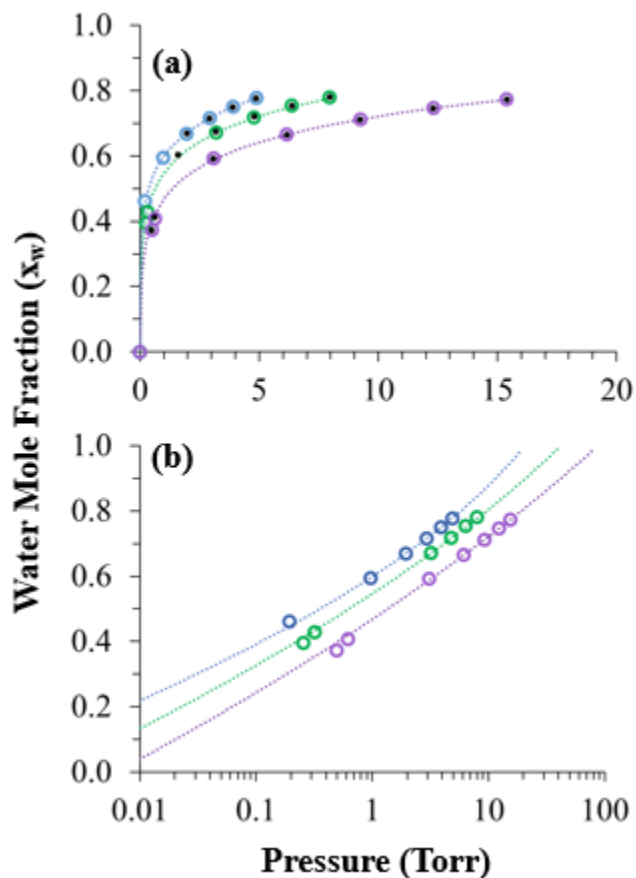


Figure 3.9: Isotherm of bulk water uptake into [C₄mim][Ace] using gravimetric analysis on a linear scale (a) and log scale (b).

Figure 3.9 (b) shows the data points on a log scale to exploit the data collected at lower water vapor pressures. As one can note, the empirical fit used for this data set fits the lower water vapor pressures well for all three isotherms. A slight change in the empirical fit would lead to drastic changes in the thermodynamic data. For this reason, it is crucial to obtain an empirical fit that fits the lower water vapor pressures due to the data set being heavily influenced by the higher water vapor pressures.

The pressure was converted to % RH for all interfacial (circles) and bulk (crosses) isotherms in Figure 3.10. There is a steep increase in water uptake between 0 – 5 % RH, and the RH continues to grow with increasing water mole fraction for both regions. In the interfacial region, the warmest isotherm at 42 °C reaches a maximum RH ~ 7.9 % at 5.0 Torr. In comparison, the coldest isotherm at 0 °C, reaches a maximum RH ~ 56.1 % at 2.5 Torr. Within the bulk ionic liquid, the final relative humidity of 25 % led to $x_w = 0.776 \pm 0.003$, as mentioned previously.

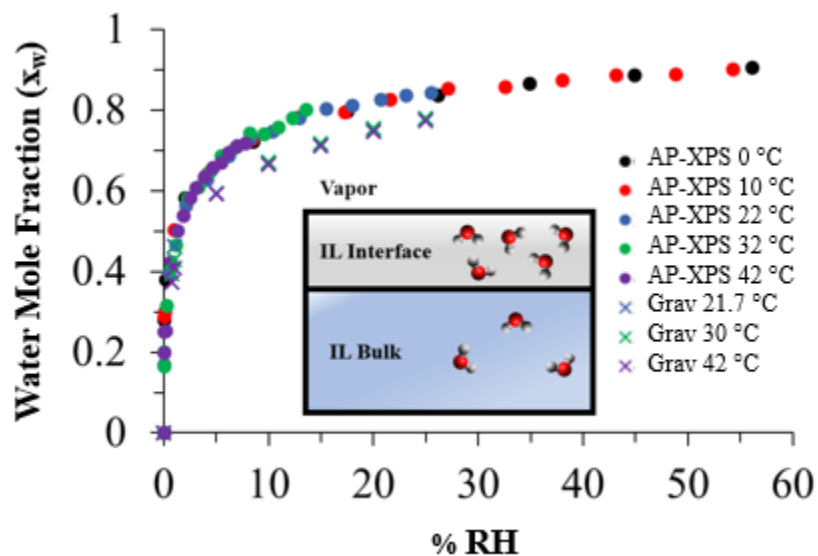


Figure 3.10: Relative humidity plot of water uptake into the interfacial region (circles) and bulk region (crosses).

Even with the drastic difference in water uptake as a function of temperature for all isotherms, the isotherms converge when converted to % RH to show two uptake curves, one for the interfacial region (circles) and the other for the bulk region

(crosses). An overlap in relative humidity of all isotherms confirms that the interfacial water uptake only depends on the water vapor pressure from 0 - 42 °C. These results agree with previous results that measured bulk water absorption of [C₂mim][BF₄] from 283 - 303K.¹¹¹

A comparison of both sets of isotherms shows that at equilibrium there is a higher concentration of water in the interfacial region than in the bulk ionic liquid between 5 < % RH < 25. This behavior of water enhancement at the ionic liquid interface relative to the bulk has been noted in molecular dynamic (MD) studies of the IL-vacuum interface for [C₁mim][Cl].^{54,57}

The enhanced concentration of water at the interfacial region could have implications in gas absorption (i.e CO₂). An experimental study, combined with MD, has shown that the presence of water causes a decrease in CO₂ solubility in acetate ILs, due to the two gases competing for the same solvation sites.⁶⁹ In addition, MD occupancy profiles of water and CO₂ at the ionic liquid-gas interface have revealed the formation of a CO₂ adsorption layer at the interface and a water inner layer right below.⁶⁰ The effect of water on CO₂ absorption has also been described experimentally. Using the 2-cyano-pyrrolide anion, gravimetric experiments studying bulk absorption of CO₂ found the CO₂ absorption decreased in the presence of water for imidazolium based ionic liquids,¹²³ while the CO₂ absorption increased in the presence of water for phosphonium based ionic liquids.¹²⁴ Gas absorption requires a gas molecule to pass the IL interface, which suggests the discrepancy may be due to changes at the interface which are not measured during bulk absorption studies. For this reason, more studies comparing water effects at the ionic liquid interface and bulk are needed.

The reversible reaction of water (W) into an ionic liquid (IL) is shown below:



For the case of water vapor sorption into [C₄mim][Ace], the final solution is a mixture of water and [C₄mim][Ace], IL(mix), where the amount of water present in the mixture may be different within the interfacial region and bulk ionic liquid. The Gibbs free energy (ΔG) equation for this type of reaction in terms of coverage has been previously discussed in detail and is shown below:

$$\Delta G = \Delta G^\circ + RT \ln Q \quad (\text{Eqn 3.3})$$

Where Q is defined as a unitless quotient of the concentration of products over reactants at standard state.¹²⁵ For water uptake in units of pressure and water mole fraction, Q is represented by:

$$Q = \frac{(x_w/x_w^\circ)^n}{\left(\frac{p}{p^\circ}\right)[(1-x_w)/(1-x_w^\circ)]^m} \quad (\text{Eqn 3.4})$$

At equilibrium, Q is equal to the equilibrium constant (K_{eq}), which can then be defined at equilibrium as the following in terms of water mole fraction (x_w) and pressure (p):

$$K_{eq} = \frac{(x_w)^n}{K^\circ p(1-x_w)^m} = e^{\Delta S^\circ/R} e^{-\Delta H^\circ/RT} \quad (\text{Eqn 3.5})$$

Where K° is the standard state constant, R is the ideal gas constant, and T is the temperature in Kelvin. ΔH° and ΔS° are the standard state enthalpy and entropy for the overall reaction (Eqn 3.2), respectively. It should also be noted that the empirical fits of the isotherms are independent of m and n, and for that reason both are set to equal one.

$$K^\circ = \frac{(x_w^\circ)^n}{p^\circ(1-x_w^\circ)^m} = \frac{1}{760} \text{ Torr}^{-1} \quad (\text{Eqn 3.6})$$

The enthalpy of water sorption at both the interfacial region and bulk ionic liquid is determined by the Clausius-Clapeyron analysis. Solving Eqn 2 for $\ln P$ gives the following:

$$\ln P = \frac{\Delta H^\circ}{RT} - \frac{\Delta S^\circ}{R} + \ln \left(\frac{(x_w)^n}{K^\circ (1-x_w)^m} \right) \quad (\text{Eqn 3.7})$$

Thus, a plot of $\ln P$ vs. $1/T$ will yield a straight line with slope of $\Delta H/R$ as shown by this equation:

$$\Delta H^\circ = R \left(\frac{\partial \ln P}{\partial \left(\frac{1}{T} \right)} \right)_{x_w} \quad (\text{Eqn 3.8})$$

The data generated from this Clausius-Clapeyron Relation (Eqn 3.8) for interfacial (a) and bulk (b) regions is shown Figure 3.11. Both plots show eight linear lines, representing water mole fractions at $0.4 < x_w < 0.75$ in 0.5 increments. The interfacial plot (a) has five points per line, representing the five temperatures (0, 10, 22, 32, 42 °C) used to collect the AP-XPS isotherms. The bulk plot (b) shows three points per linear line representing the three temperatures (21.7, 30, and 42 °C) used to collect the gravimetric isotherms. All eight water mole fraction lines collecting for the interfacial and bulk regions had an $R^2 > 0.9938$ and > 0.9984 , respectively.

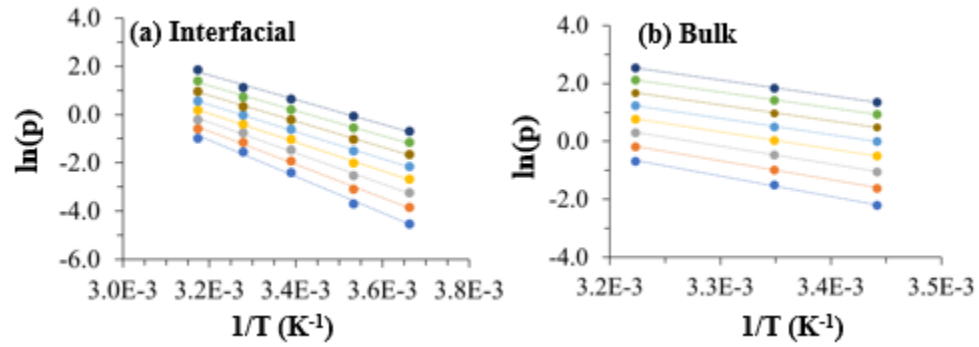


Figure 3.11: Clausius-Clapeyron relation plots from $0.4 < x_w < 0.75$ for both the interfacial (a) and bulk (b) regions.

Using Eqn. 4, the entropy of water sorption can also be determined from a plot of $T \cdot \ln P$ vs. T as defined below:

$$\Delta S^\circ = -R \left(\left(\frac{\partial T \ln P}{\partial T} \right)_{x_w} - \ln \left(\frac{(x_w)^n}{K^\circ (1-x_w)^m} \right) \right) = -R \left(\left(\frac{\partial T \ln P}{\partial T} \right)_{x_w} - \ln(c) \right) \quad (\text{Eqn 3.9})$$

Where the slope of function will be $-\Delta S/R$, due to $\ln(c)$ being defined as a constant. The entropy plots ($T \cdot \ln(P)$ vs. T) for both the interfacial (a) and bulk (b) regions is shown in Figure 3.12. Both plots show eight linear lines, representing water mole fractions at $0.4 < x_w < 0.75$ in 0.5 increments. All eight water mole fraction lines collecting for the interfacial and bulk regions had an $R^2 > 0.9921$ and > 0.9982 , respectively.

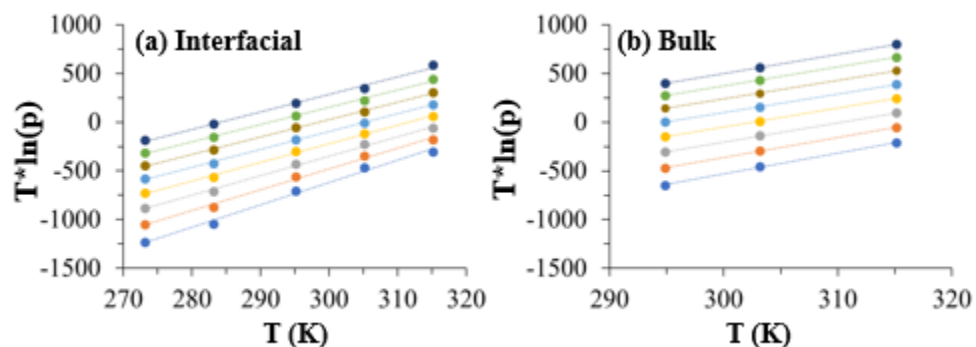


Figure 3.12: Entropy plots from $0.4 < x_w < 0.75$ for both the interfacial (a) and bulk (b) regions.

The enthalpy (a) and entropy (b) of water at the interfacial and bulk regions are shown in Figure 3.13 from $0.40 < x_w < 0.75$, along with dashed lines representing the enthalpy (-44 kJ/mol) and entropy (-147 J/mol-K) of vaporization of bulk water.¹¹⁰ The generated plot shows a change in the slope of enthalpy of interfacial water uptake (ΔH°) which can be related to water uptake into $[C_4mim][Ace]$ within both regions. Initially, at $x_w < 0.65$, the enthalpy of water in both regions is steadily increasing. When interfacial water uptake first occurs into the ionic liquid, the enthalpy of water uptake is most favorable and below the enthalpy of vaporization for bulk water. At these low water concentrations, water is interacting strongly with the acetate and most acidic carbon of the imidazolium ring. At low water mole fractions between $0.4 < x_w < 0.45$, water is also slightly more favorable in the interfacial region. However, at $x_w > 0.65$, the enthalpy of water uptake begins to converge on the enthalpy of vaporization for bulk water at 25 °C ($\Delta H_{vap} = -43.99$ kJ.mol).¹¹⁰ At these higher water mole fractions, both the interfacial and bulk regions are similar.

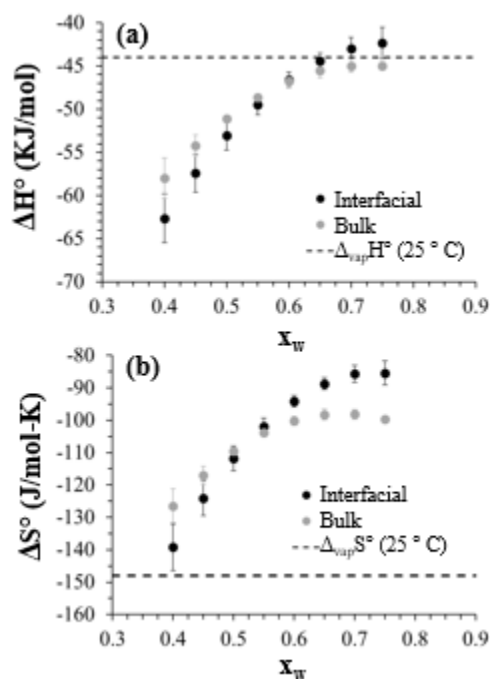


Figure 3.13: The enthalpy (a) and entropy (b) of water uptake from $0.4 < x_w < 0.75$ for both the interfacial and bulk regions. Dashed line represent the enthalpy (a) and entropy (b) of vaporization for bulk water at 25°C . Error bars represent 1σ .

There is plenty of literature on the enthalpy of mixing, ΔH_{mix} , of water and ionic liquids (liquid-liquid)^{106,120-122} and very little on the enthalpy of vaporization of water vapor and ionic liquid (liquid-gas)^{6,110,111}. The enthalpy of mixing has been determined for a range of cations and anions including imidazolium, pyridinium, and piperidinium cations with anions of various hydrophilicities. On the contrary, the liquid-gas energetics between water and ionic liquids have been explored for imidazolium cations with the $[\text{PF}_6]$ and $[\text{BF}_4]$ anions.^{24,25} In addition, UHV XPS has shown different energetics between the heat of adsorption compared to the heat of absorption of water on a solid ionic liquid surface.⁶ More data is needed to generate a

better understanding about the energetics at the gas-liquid interface of ionic liquids as well as a comparison of the energetics at both the interfacial and bulk regions.

Using line of sight mass spectrometry and ultra-high vacuum XPS, potential energy diagrams of enthalpy versus distance of gas phase water to bulk water absorption into two hydrophobic ionic liquids have been generated.²⁶ This experiment has illustrated water's tendency to reside at the ionic liquid under layer below the imidazolium alkyl chain and has also shown an energy barrier for the water to physisorb into the bulk ionic liquid. Our results indicate we may be observing the same phenomena, where water prefers the interface and must overcome an energy barrier to absorb into the bulk.

Using Eqn 3.9, a plot of entropy vs. water mole fraction is determined and shown in Figure 3.13 (b) for both interfacial and bulk water sorption into [C₄mim][Ace]. The largest difference between the interface and bulk region was seen in the entropy. The entropy of interfacial and bulk water sorption from $0.4 < x_w < 0.75$ increases with increasing water. At low $x_w < 0.55$, the entropy of interfacial and bulk water sorptions are similar. At $x_w > 0.55$, the entropy of water sorption changes, where the entropy of interfacial water continues to increase until reaching a plateau at $x_w > 0.7$. By averaging the last two data points contained in the plateau ($x_w = 0.7$ and 0.75), the calculated maximum interfacial entropy is -85.6 ± 0.2 J/mol-K. On the other hand, the bulk entropy plateaus at $x_w > 0.6$ with an average bulk entropy (last four data points) of -98.7 ± 0.7 J/mol-K. The entropy of bulk water is also shown on the plot as a dashed line at -147 J/mol-K. Both the interfacial and bulk entropy of water sorption in [C₄mim][Ace] is less favorable than the entropy of bulk water sorption within this x_w range.

Using the enthalpy and entropy at a specific temperature, the Gibbs free energy (ΔG°) can also be determined by the relation shown below:

$$\Delta G^\circ = \Delta H^\circ - T\Delta S^\circ \quad (\text{Eqn 3.10})$$

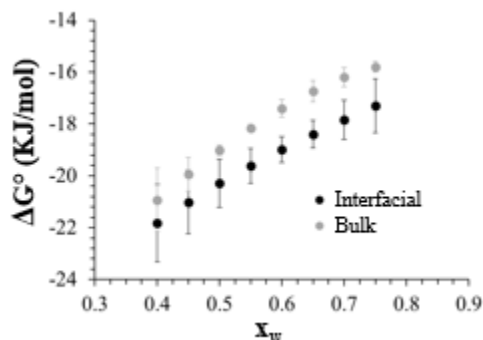


Figure 3.14: Gibbs Free Energy (ΔG°) of water sorption into $[\text{C}_4\text{mim}][\text{Ace}]$ at both the interfacial (black) and bulk (gray) regions at 20 °C. Error bars represent 1σ .

A plot of the Gibbs free energy at 20°C as a function of x_w is shown in Figure 3.14. At $x_w < 0.5$, the Gibbs free energy is relatively the same at both interfaces, whereas at $x_w > 0.5$, the interfacial Gibbs free energy is slightly more favorable than the bulk Gibbs free energy. As the water concentration increases, the calculated Gibbs free energy for both the interfacial and bulk sorption increases. At the maximum water mole fraction of 0.75, the Gibbs free energy for the interfacial and bulk sorption are -17.3 ± 1.0 kJ/mol and -15.8 ± 0.2 kJ/mol, respectively. Although both Gibbs free energies are negative, and not drastically different, the interfacial Gibbs free energy is slightly lower than that

of the bulk, which suggests that the hydration state of the interface is more spontaneous than the hydration of the bulk.

3.4 Energetics of Water at the 1-Butyl-3-Methylimidazolium Chloride–Gas Interface

Since the thermodynamics of water uptake into the interfacial region of an IL has only been explored once with the [C₄mim][Ace], we wanted to obtain thermodynamics for another hydrophilic IL. We chose the [C₄mim][Cl] due to it having the same cation and another highly hydroscopic anion.

1-butyl-3-methylimidazolium chloride, [C₄mim][Cl], is a white powder-like solid with a melting point of 338.15 K.(2001 Sheldon CC) This IL was purchased from Fluka with a purity of 99.0%. The sample was stored in a vacuum desiccation and used without further purification. The IL was deposited on a flame annealed Au foil with a T/C close to the sample. Once deposited, all of the ionic liquid deliquesced into a viscous liquid. The liquid sample was immediately transferred into the AP-XPS chamber. The temperature was controlled using a RKE chiller. Once the instrument was under vacuum, the chiller was turned on and the sample temperature was set. The sample was pumped in the chamber overnight at the temperature needed at each isotherm for AP-XPS analysis the following day. The IL remained a liquid throughout the entire experiment for all four isotherms. Four isotherms were collected at 0.0 ± 0.4 , 10.1 ± 0.2 , 20.4 ± 0.2 , and 30.5 ± 0.5 °C.

Using our lab-based AP-XPS system, electrons were captured at 20 relative to the surface normal. The survey spectrum was collected at a pass energy of 200 eV while the high resolution spectrum were collected at a pass energy of 100 eV. All XPS spectra were analysis using peak fitting software (CasaXPS, v2.3.1.6) with Gaussian-

Lorentzian (70-30%) peak fits and linear background subtraction. The spectra were references to the Calkyl component at 285.0 eV.

Water uptake into [C₄mim][Cl] for all four isotherms is shown in Figure 3.15 (a). Similarly to water uptake into [C₄mim][Ace], the coldest isotherm collected at 0 °C (black) uptakes the most water with $x_w = 0.83$ while the warmest isotherm at 30.5 °C uptakes the least amount of water, $x_w = 0.63$. In addition, the ratio of $n_w:n_{IL}$ were calculated for each isotherm. At the maximum water vapor pressure of 2.5 Torr, the isotherm collected at 0 °C has approximately 5 water molecules around 1 IL pair. When compared to the water uptake into [C₄mim][Ace], this IL has less water within the interfacial region, which has been shown for bulk water absorption previously.⁸⁵ The dashed line through each isotherm represents an empirical fit with $R^2 > 0.996$.

The same data is plotted in log scale in Figure 3.15 (b). As one can see in the log plot, data points collected below water vapor pressure of 0.5 Torr overlap drastically for the two warmest isotherms at 20.4 °C (blue) and 30.5 °C (green); therefore, $x_w < 0.4$ were not considered in the calculation of thermodynamics. In addition, $x_w > 0.6$ were also not considered in the thermodynamics due to the warmest isotherm only having a maximum $x_w = 0.63$. One can see the empirical fit models the isotherms well from $0.4 < x_w < 0.6$.

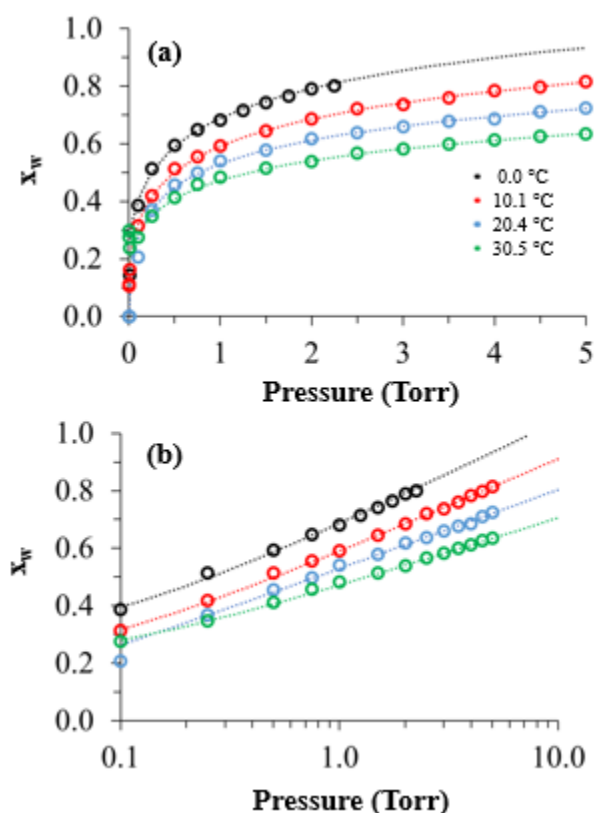


Figure 3.15: Isotherm of bulk water uptake into $[C_4mim][Cl]$ using AP-XPS on a linear scale (a) and log scale (b).

Similarly to the water uptake into $[C_4mim][Ace]$, the relative humidity plot for the isotherms of water uptake into $[C_4mim][Cl]$ were plotted in Figure 3.16. As expected, all four isotherms converge to form one uptake curve. This confirms that water uptake is the only factor contributing to the amount of water calculated in the interfacial region. In this experiment, the largest water mole fraction at 0.83 occurs at RH ~ 56.1 % (black isotherm). Each isotherm ends at a different % RH, where the isotherm at 30.5 °C, 20.4 °C, 10.1 °C, and 0.0 °C are exposed to a maximum % RH of 15.0 %, 28.0 %, 55.0 %, and 56.1 %, respectively.

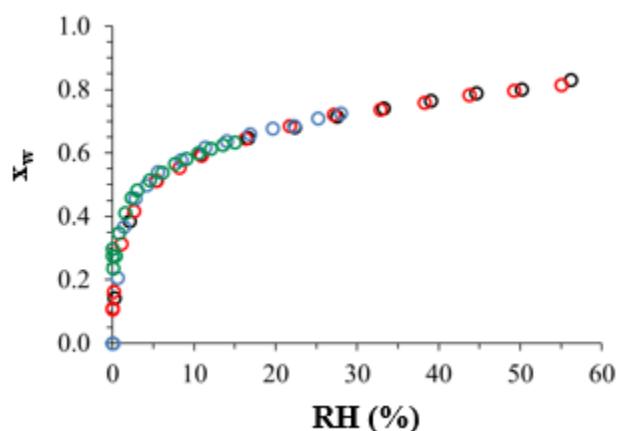


Figure 3.16: Water mole fraction vs. relative humidity (%) plot for all four isotherms showing one uptake curve.

Using all four isotherms between 0 – 30.5 °C, the energetics of water uptake into [C₄mim][Cl] can be determined. The enthalpy (a) and entropy (b) of this interaction at $0.4 < x_w < 0.6$ is shown in Figure 3.17. The enthalpy of bulk water at 25 °C is shown as a black dashed line. As one can see, the enthalpy of water into this IL is slightly less favorable than the enthalpy of bulk water. The enthalpy is also similar at all x_w within this range (error bars are large). In addition, the entropy of this process is also similar within this x_w range. In both cases, the error bars on the points at smaller x_w are larger due to the data being noisier at the smaller x_w , which is also apparent from the uptake curve shown in log scale.

Additionally, this IL was studied to compared the energetics to the energetics of water into [C₄mim][Ace]. A comparison shows drastically different trends. The [C₄mim][Ace] initially shows energetics that are more favorable than the enthalpy of bulk water and as more water is added to the system it becomes less favorable until it reaches the bulk enthalpy of water. This makes sense due to the initial strong

interaction between the anion – water that is then weakened as more water is absorbed into the interfacial region, leading to more water – water interactions. However, the [C₄mim][Cl] shows slightly less favorable energetics within this x_w range. While it is not clear why these energetics are less favorable and relatively unchanged, bulk energetics of this process may provide additional insight to this observed behavior. It is possible that the orientation of the anion and cation for [C₄mim][Cl] within the interface may be different than the orientation of these species for [C₄mim][Ace] causing very different energetic trends.

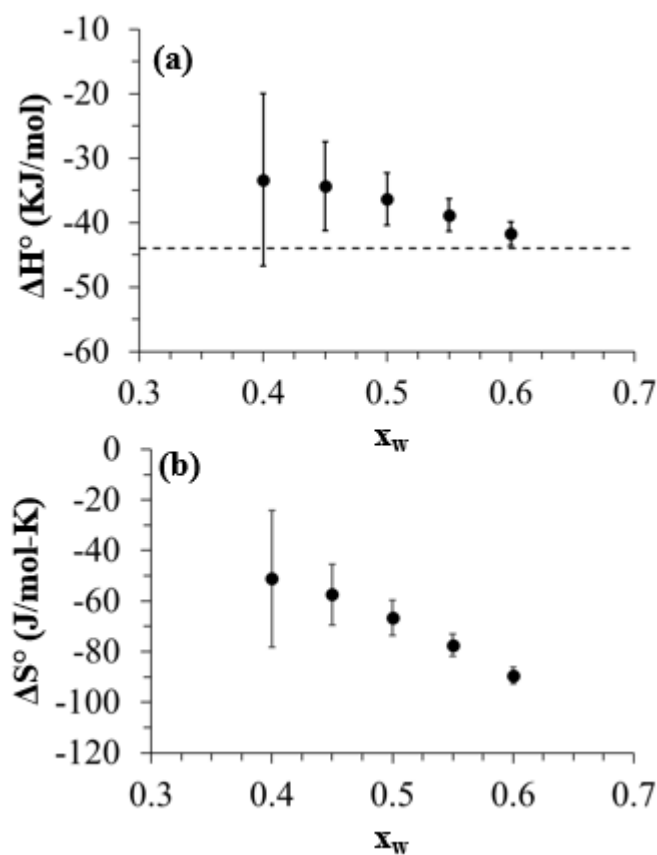


Figure 3.17: The enthalpy (a) and entropy (c) of water uptake from $0.4 < x_w < 0.60$ for [C₄mim][Cl] using AP-XPS. The dashed line represent the enthalpy (a) of vaporization for bulk water at 25 °C. Error bars represent 1σ .

The data generated from the Clausius-Clapeyron Relation (a) and entropy plot (b) for interfacial water uptake into [C₄mim][Cl] is shown Figure 3.18. Both plots show five linear lines, representing water mole fractions at $0.4 < x_w < 0.6$ in 0.5 increments. Each line is made up of four data, representing the four temperatures (0, 10.1, 20.4, 30.5 °C) used to collect the AP-XPS isotherms. All five water mole fraction lines collecting for the enthalpy (a) and entropy (b) had an $R^2 > 0.9717$ and > 0.9653 , respectively.

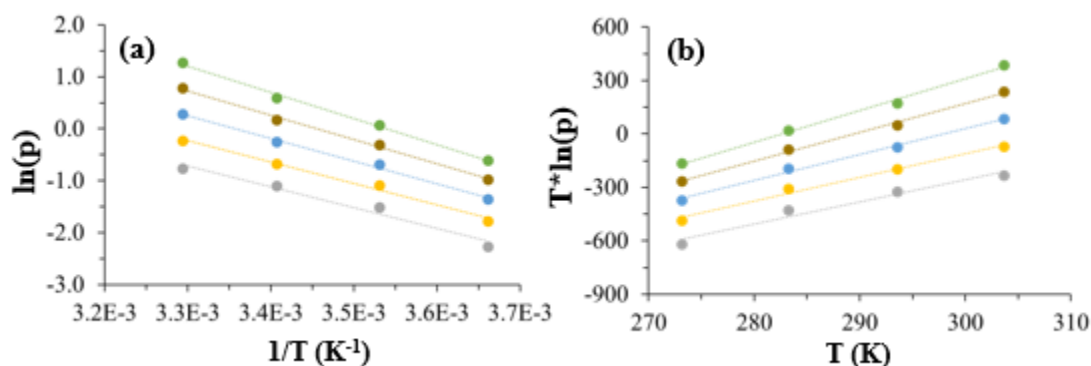


Figure 3.18: Clausius-Clapeyron relation (a) and entropy (b) plots from $0.4 < x_w < 0.6$ for interfacial water uptake into [C₄mim][Cl].

Using the enthalpy and entropy at 20 °C, the Gibbs Free Energy of water into [C₄mim][Cl] was also determined and shown in Figure 3.19. Between $0.4 < x_w < 0.6$, the Gibbs Free Energy is relatively the same within this temperature range. On average, $\Delta G \sim -16.9 \pm 1.0$ kJ/mol. In comparison to [C₄mim][Ace] where ΔG is less favorable as more water is added to the IL interfacial region, [C₄mim][Cl] shows a different trend in ΔG . Again, this different trend may be due to differences in the interfaces of these ILs.

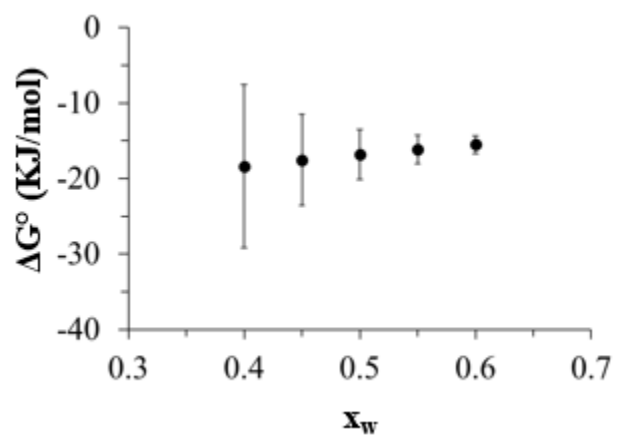


Figure 3.19: Gibbs Free Energy (ΔG°) of water sorption into [C₄mim][Cl] at the interfacial region at 20 °C. Error bars represent 1σ .

Chapter 4

DELIQUESCENT OF IONIC LIQUIDS

4.1 Introduction

Salts are known to be compounds that deliquesce, or have a high affinity to absorb water vapor out of the air to form aqueous solutions. The deliquescence process of sodium chloride, NaCl, is highlighted in Figure 4.1. When a salt crystal is initially exposed to the atmosphere, water will adsorb on the surface of this crystal, forming a layer of water around the crystal. Overtime, the deliquescence process will reach equilibrium, where a saturated aqueous salt solution will form. When the salt crystal is then dried (all water removed), the salt will return to its crystal form. Understanding this process for salt solutions is critical for use in laboratory setting as a desiccant to remove water for other samples and in industry to remove water from chemical reactions.

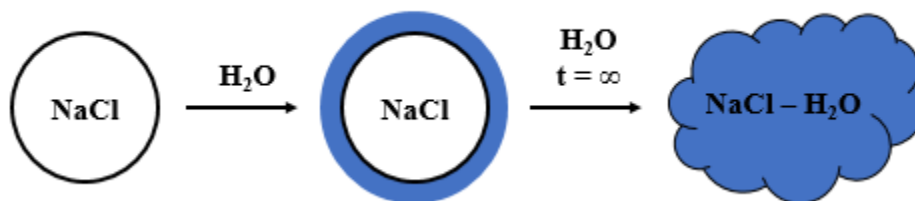


Figure 4.1: Deliquescence process of NaCl where initial water vapor adsorption occurs on the solid-gas interface and then over time will be absorbed to form an aqueous salt solution.

This process has been studied extensively for both the initial adsorption of water onto the surface of the salt crystal as well as the equilibrium process of forming an aqueous salt solution. Using surface sensitive analytical instrumentation (i.e. AP-XPS), the initial adsorption of water onto the surface of salt solutions has been studied to understand ion enhancement at the initial water film as well as the exact relative humidity needed to deliquesce the solid salt.¹²⁶

Using AP-XPS, the deliquescence of salts has been well studied. Using synchrotron based AP-XPS, the interaction of salt samples including NaCl, KI, and LiCl with water vapor at the ionic liquid-vapor interface have been explored.¹²⁷⁻¹²⁹ Depth profiles generated of the saturated NaCl showed an enhancement of the anion (Cl⁻) at the surface.¹³⁰ Similarly, in a pure KI-water solution, the anion is enhanced at the interface.¹²⁸ The question still remains if an ionic liquid will behave in a similar manner when exposed to enough water vapor to deliquesce.

While the deliquescence process of a traditional salt has been studied, solid ionic liquids have started to generate interest as well. To the best of our knowledge, there has only been one deliquescence study of water with an ionic liquid.¹³¹ In this study, the deliquescence of tetraethylphosphonium benzimidazolide, [P₂₂₂₂][BnIm], in the presence of water vapor from 0 to 80 mbar and temperatures from 53 °C to 80 °C was explored. The deliquescence process required more water vapor at higher temperatures. At 53 °C and 62 °C, the ionic liquid deliquescence process occurred at 7 and 12 mbar, respectively. At the warmer temperature of 80 °C, the deliquescence process occurred at water vapor partial pressure of 65 mbar. This data was used for developing pre-dryer systems for CO₂ capture, where water absorption can affect CO₂ uptake in ionic liquids.

In this chapter, the deliquescence of ionic liquids is explored. First, the bulk deliquescence of two ionic liquids, 1-methyl Piperizinium Acetate, [MP][Ace], and methylamine malate, [MA]₂[Mal], is attempted using a saturated potassium iodide salt solution with RH = 69% and in open lab air with RH = 48%. Then, the deliquescence of 1-butyl-3-methylimidazolium chloride, [C₄mim][Cl], is explored using AP-XPS from vacuum up to RH = 34.7 %.

4.2 Deliquescence using Lab Air and Salt Solutions

Prior to analysis in the AP-XPS chamber, the deliquescence process of solid ionic liquid in the presence of water vapor was explored. The goal was to find an ideal candidate for deliquescence that would deliquesce within the chambers relative humidity limits of $0 < \% RH < 55$. Also, the kinetics of the solid ionic liquid deliquescence process would be monitored.

4.2.1 Experimental Details

The deliquescence process of several ionic liquids was qualitatively assessed. 1-methylpiperazinium acetate, [MP][Ace], and methylamine malate, [MA]₂[Mal], were both synthesized in house with an acid base reaction. The final products were dried in a vacuum oven for several days and characterized using nuclear magnetic resonance (NMR). Prior to the deliquescence experiments, the samples were stored in a vacuum desiccator. During the deliquescence experiments, the samples were taken from the vial without any further characterization.

The two different deliquescence experiments were conducted where the sample was exposed to a saturated salt solution (a) and to lab air (b) are shown in Figure 4.2. To expose the sample to a saturated salt solution, a makeshift gas cell was designed

using sealed glass jar (a). The top of the jar had two ports for nitrogen gas. The first is to allow the gas to flow into the cell (removing any air and drying the sample) and the second is to allow the gas to leave. The glass slide was also Torr sealed to the top of the jar, allowing one to image the deliquescence process using a microscope and camera. Inside the jar, a saturated salt solution was placed close to the solid ionic liquid that was deposited on a white plastic dish. A black dot was placed on the white plastic dish to indicate where the sample should be placed for optimal imaging. After purging the cell with nitrogen for several minutes, both ports (gas in and gas out) were sealed with parafilm and the cell was left to saturate with the relative humidity provided by the saturated salt solution. Images of the deliquescence process were captured using a light microscope (AmScope SM-4TZZ) and a camera (info).

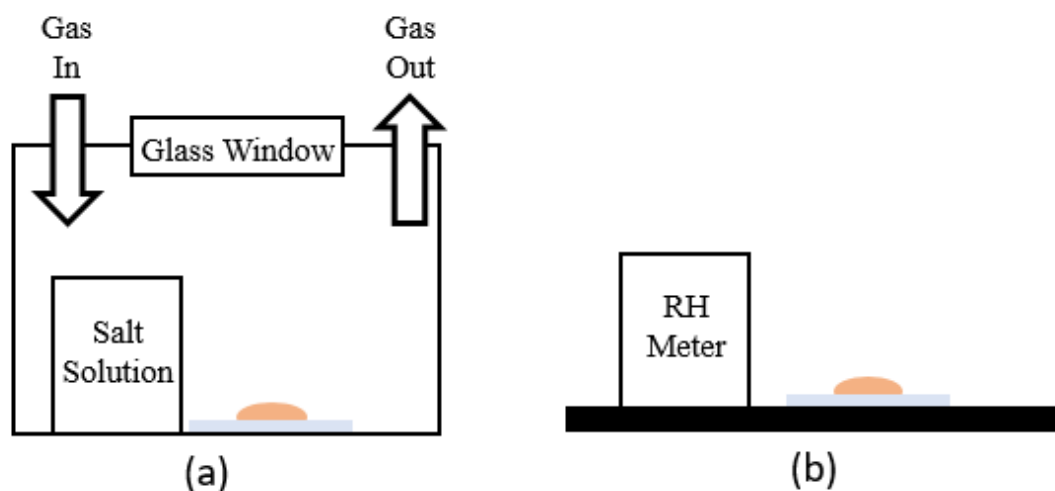


Figure 4.2: Experimental set-up for studying the deliquescence of ionic liquids with saturated salt solutions in a closed container (b) and in lab air (a).

The deliquescence process was also studied by exposing the ionic liquid to lab air shown in Figure 4.2 (b). In these experiments, a small amount of the solid ionic liquid was placed on a glass slide and the deliquescence process was captured using a light microscope (LM Olympus BX60). This light microscope could only be used with lab air deliquescence process due to the aperture being relatively close to the sample with no room to add a closed cell. A relative humidity meter was kept close to the sample to monitor the %RH of the air.

4.2.2 Qualitative Assessment of IL Deliquescence

Initially, the deliquescence process was monitored using a saturated salt solution with a known %RH. The qualitative deliquescence process of [MP][Ace] at RH = 69% is shown in Figure 4.3. The deliquescence process was relatively fast at this %RH, and images were captured in 20 second increments. Initially, at $t = 0$ secs, the [MP][Ace] sample is a white solid. Within the first 20 secs, the sample begins to liquefy around the edges, indicating the start of the deliquescence process. By 60 secs of exposure, the edges have fully liquefied, leaving a small solid in the center. In the final image of 100 secs, the sample has a small crystal in the center, but is mostly liquid.

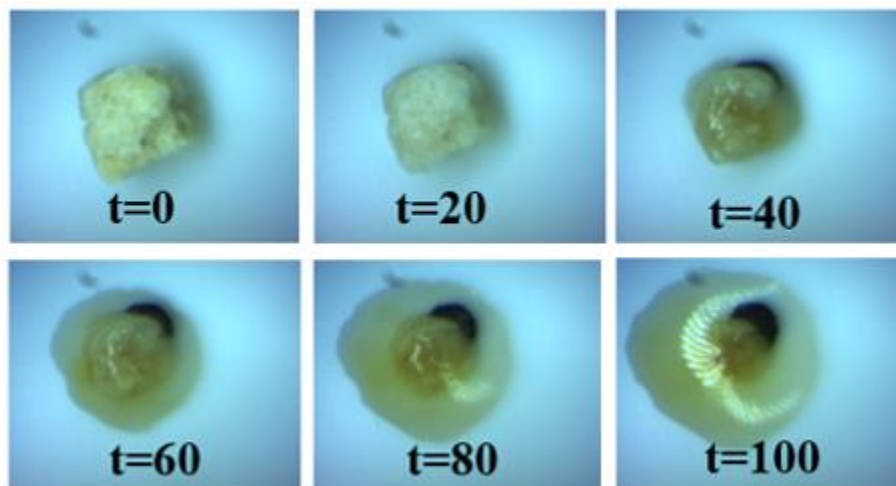


Figure 4.3: Images of deliquescence of [MP][Ace] versus time (sec) using a saturated solution of potassium iodide (RH = 69%) captured via light microscope.

Due to the fast kinetics of deliquescence with a salt solution (RH = 69%), the deliquescence of methylamine malate, [MA]₂[Mal], was monitored in lab air with RH = 48 %. At this lower relative humidity, the deliquescence process is slower which allowed us to capture the process on the orders of minutes rather than seconds. The deliquescence process, shown in Figure 4.4, was captured using a light microscope (LM Olympus BX60). Initially, at t = 0 minutes a white solid crystal with a liquid surface is seen. After 4 minutes of exposure to RH = 48 %, a liquid puddle (black) is around the white crystal. This liquid puddle continues to grow until a very small white crystal is seen at t = 16 minutes.

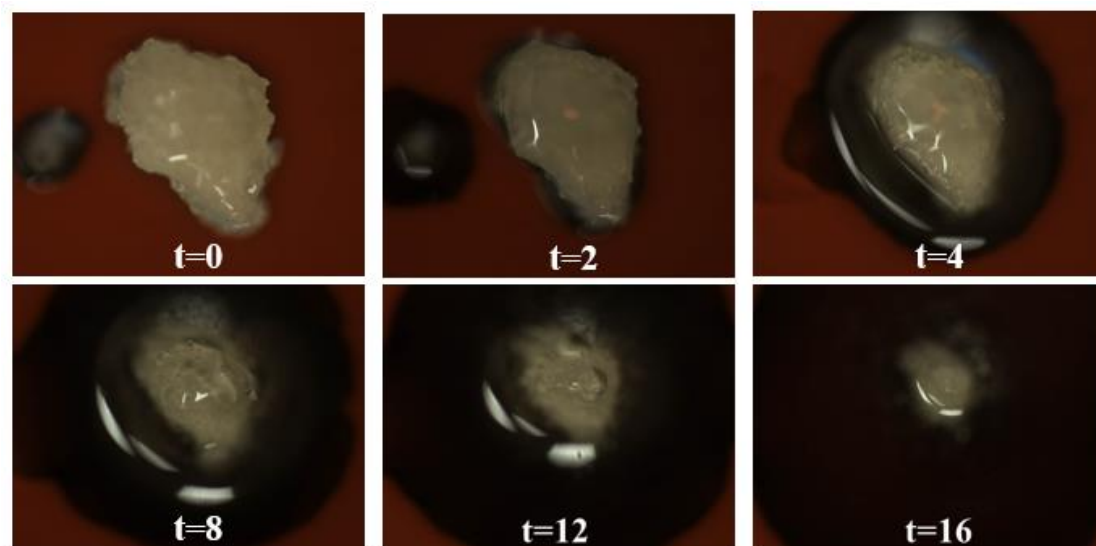


Figure 4.4: Images of deliquescence of $[\text{MA}]_2[\text{Mal}]$ versus time (min) under lab air (RH = 48%) captured via light microscope.

While the $[\text{MA}]_2[\text{Mal}]$ had slower kinetics at a lower RH = 48 % than the $[\text{MP}][\text{Ace}]$ at RH = 69 %, the relative humidity is still too high to conduct a detailed AP-XPS experiment, where the experiment should occur from $0 < \% \text{RH} < 55$. By exposing the $[\text{MA}]_2[\text{Mal}]$ and $[\text{MP}][\text{Ace}]$ to salt solutions with lower % RH, we would slow the kinetics, which is also not ideal.

The deliquescence process of other ionic liquids was also studied and a summary of these results is shown in Table 4.1. Both 1-ethyl-3-methylimidazolium chloride, $[\text{C}_2\text{mim}][\text{Cl}]$, and 1-butyl-3-methylimidazolium chloride, $[\text{C}_4\text{mim}][\text{Cl}]$, were purchased from Fluka with a purity of 99%. Bis(2-methoxyethyl)ammonium acetate, $[\text{Ch}][\text{Ace}]$, was purchased from Fluka with a purity of 90%. Tetramethylammonium acetate (95%), $[\text{TMA}][\text{Ace}]$, and 1-methylimidazolium tetrafluoroborate (purity 95%), $[\text{C}_1\text{mim}][\text{BF}_4]$, were purchased from Bioniqs and EMD Merck, respectively. All samples were stored in a dessicator.

Table 4.1: Ionic Liquid Deliquescence Summary

Ionic Liquid	RH	Deliquescence	Time
[MA] ₂ [Mal]	69%	Y	100 secs
[MP][Ace]	48%	Y	16 mins
[C ₂ mim][Cl]	48%	Y	< 1 sec
[C ₄ mim][Cl]	48%	Y	< 1 sec
[TMA][Ace]	48%	Y	< 1 sec
[Ch][Ace]	48%	Y	< 1 sec
[C ₁ mim][BF ₄]	48%	Y	< 1 sec

Although the deliquescence process was rapid for most of the ionic liquid samples studied, the % RH needed for the deliquescence process is relatively high. The AP-XPS system is capable of water exposures up to a RH ~ 60 %. In order to obtain a complete picture of where the deliquescence process occurs, an ideal relative humidity of a solid ionic liquid for AP-XPS analysis would occur around RH ~ 10%. This would allow the XPS spectra collection to capture the deliquescence process before, during, and after.

4.3 Deliquescence of 1-Butyl-3-Methylimidazolium Chloride via AP-XPS

The imidazolium based ionic liquids deliquescence immediately before being exposed to salt solutions with low % RH (RH < 20 %). For this reason, further XPS characterization of these samples was completed to determine the surface purity and vacuum compatibility. Based on the results, 1-butyl-3-methylimidazolium chloride, [C₄mim][Cl], was used as an initial test of ionic liquid deliquescence using AP-XPS.

4.3.1 Experimental

1-butyl-3-methylimidazolium chloride, [C₄mim][Cl], is a white powder-like solid with a melting point of 338.15 K.(2001 Sheldon CC) The sample was stored in a vacuum desiccation and used without further purification. The IL was deposited on a

flame annealed Au foil with a T/C close to the sample. Once deposited, most of the ionic liquid deliquesced, with only a small visible crystal seen in the droplet. The sample was immediately transferred into the AP-XPS chamber. The temperature was controlled using a RKE chiller. Once the instrument was under vacuum, the chiller was turned on and the sample temperature was set to -5.0 °C. The sample was pumped in the chamber overnight at this temperature for AP-XPS analysis the following day.

Our lab-based AP-XPS system was used to monitor the deliquescence of [C₄mim][Cl]. Electrons were captured at 20° relative to the surface normal. The survey spectrum was collected at a pass energy of 200 eV while the high resolution spectrum were collected at a pass energy of 100 eV. All XPS spectra were analysis using peak fitting software (CasaXPS, v2.3.1.6) with Gaussian-Lorentzian (70-30%) peak fits and linear background subtraction. The spectra were not referenced to any specific species to monitor the BE change from a charged solid sample to a liquid sample and then the effect of water on the BE.

Millipore water in a glass bulb was introduced into our chamber with a variable leak valve. Prior purification of the water was done with three freeze-degas cycles. The water vapor was increased from 10⁻⁷ Torr until reaching a maximum pressure of 1.15 Torr. Throughout the experiment, the sample temperature was held constant -5.0 °C. XPS spectra was collected in the following order: O 1s, C 1s, N 1s, Cl 2p, and O 1s. Two O 1s spectra were collected at each pressure to confirm the sample was at equilibrium. Between pressures, the x-ray source was shut off to limit the amount of beam exposure time. Based on the N 1s spectra, there was no apparent beam damage through ut the duration of the experiment.

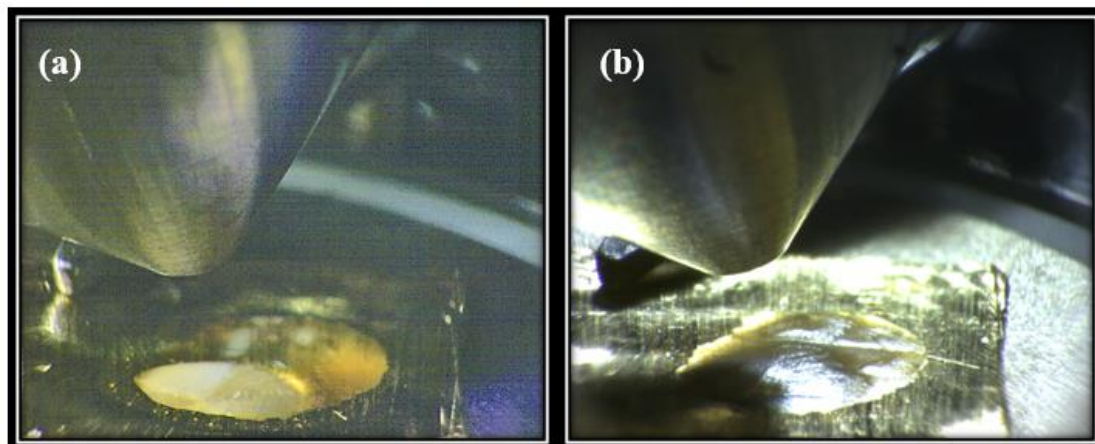


Figure 4.5: Images captured when [C₄mim][Cl] was first pumped down in AP-XPS chamber at 22 °C (a) and after pumping in AP-XPS chamber overnight at -5 °C (b).

Figure 4.5 shows the images captured of the [C₄mim][Cl] droplet when it was first pumped down in the chamber at 22 °C (a) and after pumping overnight at -5 °C (b). When the sample is first pumped down in the chamber at a base pressure of 6×10^{-8} Torr and 22 °C, [C₄mim][Cl] is both a solid (white) and liquid (yellow). The sample temperature was then set to -5 °C and left to pump in vacuum overnight. The following day, the sample was completely a solid which was confirmed by visibly looking at the sample and by collecting C 1s XPS spectra at multiple spots. When collecting XPS sample, the aliphatic carbon chain, C_{alkyl}, was seen at a charged BE of 295.6 eV.

4.3.2 Isotherm of Interfacial Water Sorption

After confirming [C₄mim][Cl] was a solid at 4.5×10^{-8} Torr and -5 °C, XPS spectra was collected. To confirm the purity of the sample, the survey spectrum was

captured at 4.5×10^{-8} Torr and is shown in Figure 4.6 along with the chemical structure. The survey spectrum contains Cl 2p, Cl 2s, C 1s, and N 1s, which are all present in the chemical structure of [C₄mim][Cl]. The survey spectrum also shows a large O 1s peak, which is a contamination with the interfacial region. This contamination may be due to physisorbed water within the IL that has risen to the surface when the sample was pumped down or water that has condensed onto the surface of the ionic liquid. The amount of O 1s present at the beginning of the experiment was noted and monitored, with no change in this species from 10^{-8} Torr to 0.10 Torr.

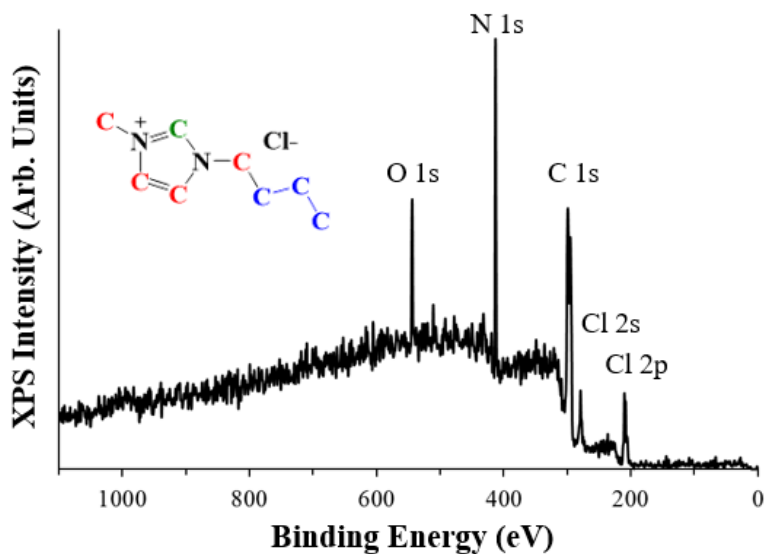


Figure 4.6: Survey spectrum of solid [C₄mim][Cl] collected at -5.0 °C and 4.5×10^{-8} Torr along with the chemical structure.

The high-resolution spectra of C 1s (a), N 1s (b), and Cl 2p (c) are shown in Figure 4.7. The C 1s spectrum was fit with three components that are color coded to

match the chemical structure. From low to high binding energy, the carbon species are C_{alkyl} (blue), C_{ring} (red), and C_{ox} (green) at 295.6, 296.8, and 297.7 eV, respectively. The peak area ratio of $C_{\text{alkyl}}:C_{\text{ring}}:C_{\text{ox}}$ is 3:4:1, confirming the purity of the solid IL. The N 1s spectrum shows one component at 412.4 eV which represents the nitrogen on the imidazolium ring. The Cl 2p spectrum shows a doublet for 2p(3/2) and 2p(1/2) spins with a separation of 1.6 eV. The Cl 2p(3/2) is seen at 207.8 eV for the solid $[\text{C}_4\text{mim}][\text{Cl}]$. In addition, a very small O 1s component was seen where the spectra had one main component and a small shoulder at lower binding energy. As noted previously, the size of these components did not change from pressures up to 0.1 Torr. At pressures > 1.1 Torr, the small shoulder is no longer present and growth is noted in the main O 1s peak, called O_w . This species is believed to be interfacial water, with growth seen as more water is introduced into the system. The width of the O 1s species O_w was constrained between $1.4 < \text{FWHM} < 1.5$ through the experiment. This constraint agrees with fittings used for our $[\text{C}_4\text{mim}][\text{Ace}]$ experiments.

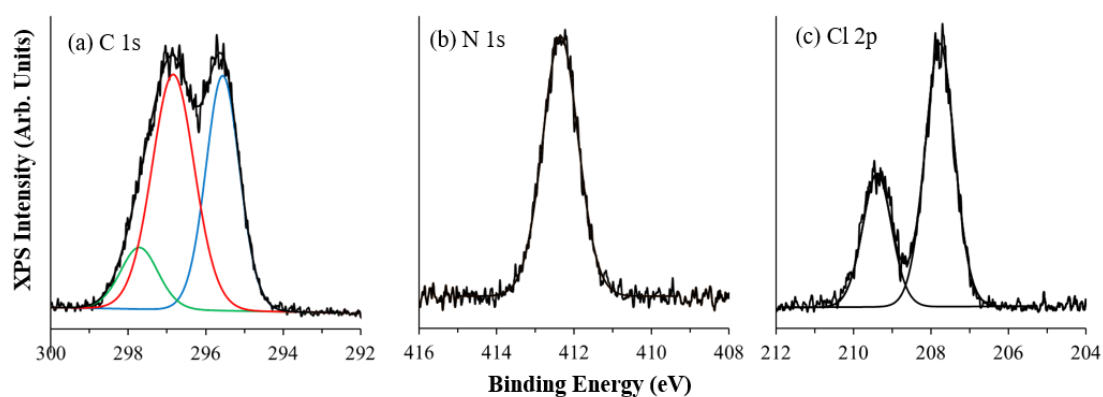


Figure 4.7: $[\text{C}_4\text{mim}][\text{Cl}]$ high resolution spectra of C 1s (a), N 1s (b), and Cl 2p (c).

After confirming the purity of [C₄mim][Cl], water was introduced into the chamber starting with 1.0 x 10⁻⁴ Torr. The water was systematically increased and XPS spectra was collected at each water vapor pressure, with the maximum water vapor pressure of 1.15 Torr. The isotherm of water uptake in [C₄mim][Cl] is shown in Figure 4.8 using both the initial O 1s spectrum (red) and the final O 1s spectrum (blue). The water mole fraction was calculated by using the N_{ring} and O_w peak areas at each water vapor pressure, as described in Chapter 3.

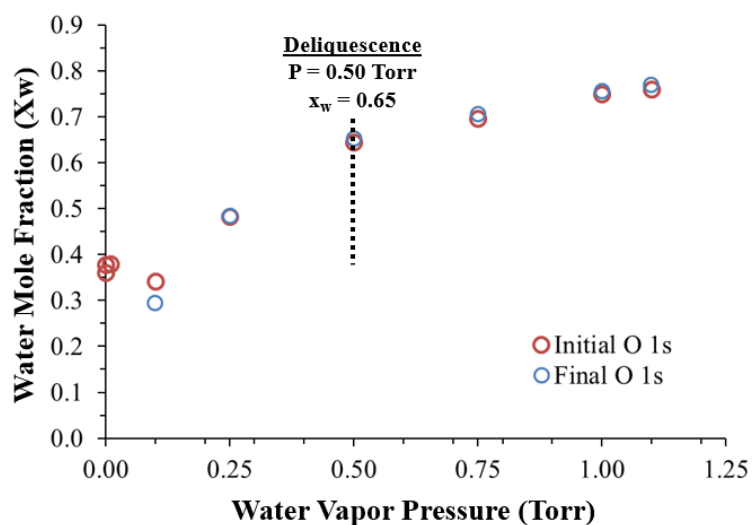


Figure 4.8: Isotherm of water uptake into [C₄mim][Cl] quantifying the initial O 1s spectrum (red) and the final O 1s spectrum (blue) at -5 °C.

Initially, there is a small amount of water, $x_w = 0.36$, present in the [C₄mim][Cl] at water vapor pressures > 0.1 Torr. At 0.25 Torr, the amount of water within the sample increases to $x_w = 0.48$; however, the IL is visibly still a solid. Immediately at a water vapor exposure of 0.5, the ionic liquid is a liquid with $x_w =$

0.65. This water vapor pressure is equivalent to a relative humidity of 17.1 % at -5 °C. As the IL is further exposed to higher water vapor pressure, the amount of water within the interfacial region continues to increase, with a maximum $x_w = 0.76$ at the maximum water vapor pressure of 1.1 Torr. Another point to note is the agreement between the initial and final O 1s spectra, the beginning and end O 1s spectrum were collected ~ 50 minutes apart from one another. At each water vapor pressure, the x_w overlaps when using the beginning or ending O 1s spectrum. This agreement shows that at each water vapor pressure, the system has reached equilibrium within the first 8 minutes O 1s spectra. Also, the deliquescence process at 0.5 Torr does not show any time dependence, indicating the rapid (within one 8 minute AP-XPS spectrum collection) deliquescence of [C₄mim][Cl] at RH = 17.1%.

The qualitative assessment of the deliquescence of [C₄mim][Cl] is shown in Figure 4.9. At a water vapor exposure of 0.25 Torr (RH = 8.53%) in Figure 4.9 (a), the IL is still a solid. This is apparent in the white reflective areas of the IL. Immediately after exposing the IL to 0.50 Torr (RH = 17.1%) in Figure 4.9 (b), the sample is completely a yellow liquid. The liquid appearance has been confirmed with other ILs in the AP-XPS chamber. This qualitative assessment further confirms that the deliquescence process of [C₄mim][Cl] occurs between $8.53 < \% RH < 17.1$.

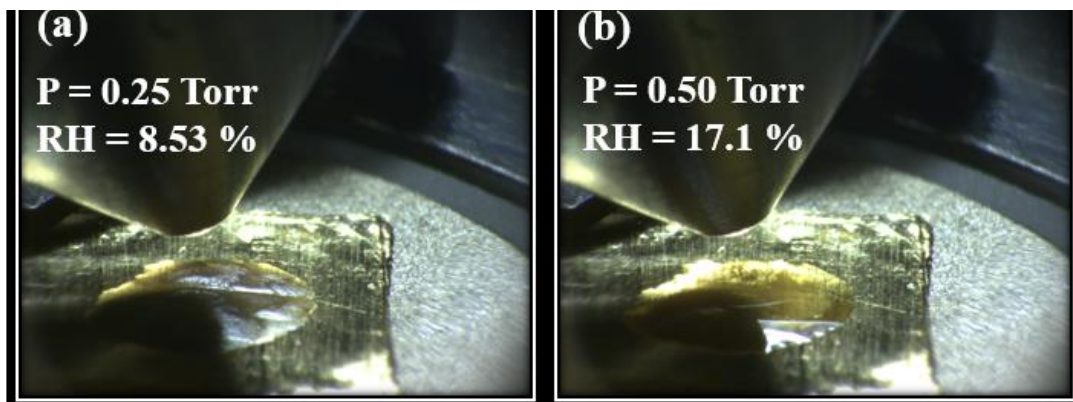


Figure 4.9: Images captured of [C₄mim][Cl] -water system as a solid in the lab-based AP-XPS at 0.25 Torr (a) and liquid at 0.50 Torr (b).

To better assess the exact deliquescence point of [C₄mim][Cl], the water vapor needs to be introduced into the AP-XPS chamber at smaller water vapor pressure increments between 0.25 and 0.5 Torr. While this task seems simple, the deliquescence process of this sample was not reversible when water was removed from the chamber. Due to this reason, the exact % RH need for deliquescence was not determined. As discussed in Chapter 3, to solidify this particular IL one must have a small seed present in the sample to have it return from a liquid to a solid. Once the IL deliquesced, the IL is completely a liquid, with no solid seed present in the droplet. For this reason, even with the removal of water from the AP-XPS chamber, the IL remains a liquid.

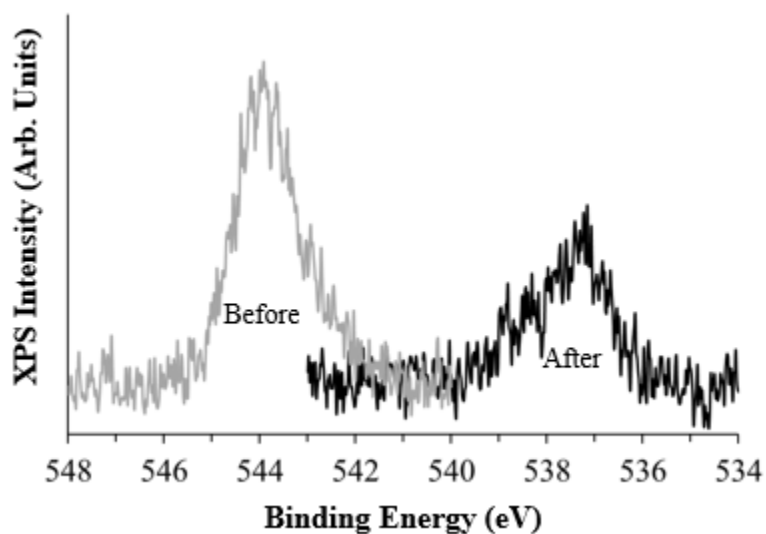


Figure 4.10: Vacuum O 1s spectrum before water exposure (gray) and after water exposure (black) of [C₄mim][Cl] at -5 °C.

At the end of the experiment when water is removed from the chamber, an O 1s spectrum is collected. A comparison of the vacuum O 1s spectrum before (gray) and after (black) water exposure is shown in Figure 4.10. The binding energy of both of these O 1s peaks are drastically different. As a solid IL (gray) the O 1s peak is at 543.9 eV while the liquid IL (black) shows a peak at 537.5 eV. As stated previously, this difference in binding energy is due to the phase change of the IL, where the solid IL will show a peak at higher binding energy. Also, the initial vacuum O 1s spectrum (gray) shows a larger peak than the O 1s spectrum collected after water exposure (black). This may be due to water's ability to easily escape the IL when it is a liquid rather than a solid. It has been stated that at the beginning of the water, it is believed the O 1s contamination is due to physisorbed water that is trapped within the interfacial region. At the end of the experiment, this physisorbed water is still trapped

but the phase change of the IL from solid to liquid allows some of that physisorbed water to escape.

Although the exact deliquescence point was not determined, other assessments within the data was determined including changing the other elements present in the sample as well as chemical shifting.

4.3.3 Chemical Shifts due to Charge Dissipation

Prior to deliquescence, changes in the AP-XPS were noted in all species (C 1s, N 1s, and Cl 2p) present in the IL. As an example, the C 1s spectrum collected as a function of increasing % RH is shown in Figure 4.11. The initial vacuum spectrum collected at 4.5×10^{-8} Torr, is shifted to higher binding energy. As the sample is exposed to increasing water vapor, the C 1s spectrum shifts to lower binding energy. While still a solid, the C 1s spectra shifts ~ 5.9 eV from vacuum to 0.25 Torr.

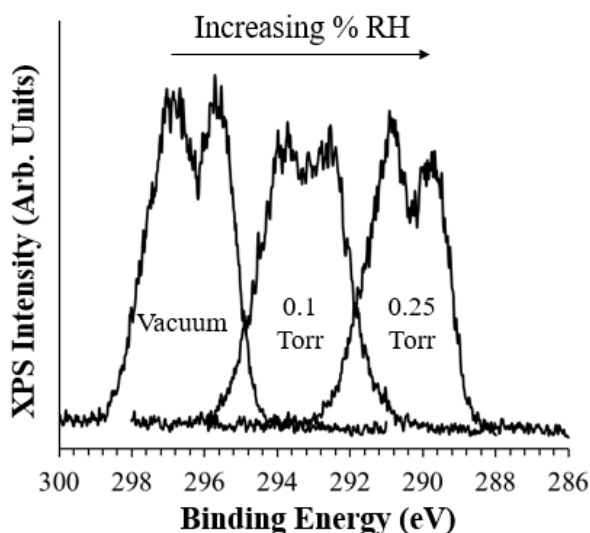


Figure 4.11: C 1s spectra of [C₄mim][Cl] showing chemical shift in the presence of water due to charge dissipation.

As noted above, this behavior is seen in all species (C 1s, N 1s, and Cl 2p) in Figure 4.12. At water vapor exposures > 0.25 Torr, the IL is still a solid. For the C 1s species (C_{alkyl} , C_{ring} , and C_{ox}), the average shift from vacuum to 0.25 Torr is 5.97 ± 0.06 eV. The shift in the N_{ring} and Cl 2p(3/2) component is 5.97 eV and 5.80 eV, respectively. As one can see, within this pressure regime when the IL is a solid, all species experience the same charging effect that shifts to lower binding energy with the addition of more water vapor.

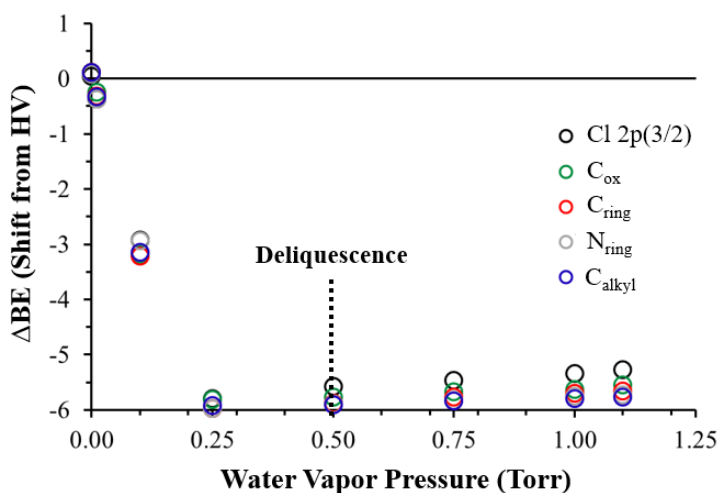


Figure 4.12: Binding energy shifts (ΔBE) relative to high vacuum spectrum of $[\text{C}_4\text{mim}][\text{Cl}]$ as a function of water vapor pressure.

This type of behavior has been noted heavily in literature for the deliquescence process of salts. The chemical shifting to lower binding energy in the presence of increasing water vapor is due to charge dissipation. When water is initially introduced to the ionic liquid environment, the water solvates the surface ions. This leads to a change in surface ion mobility, which is represented by a shift to lower binding energy

in the AP-XPS spectra as the relative humidity is increased. Once the surface ions are solvated, the addition of more water leads to the solvation of the bulk IL and is represented by the deliquescence point. At this point, the solid IL is now a liquid. While this phenomenon has been well studied for different salts, this is the first time it is being studied with a solid IL sample.

For [C₄mim][Cl], the deliquescence point is seen in the presence of a water vapor pressure of 0.5 Torr. However, the actual deliquescence point is somewhere in between $8.5 < \% \text{ RH} < 17.1$. A more diligent experiment at water vapor pressures between 0.25 and 0.5 Torr is needed to pinpoint the exact deliquescence point of this particular IL.

As will be discussed in the next section, an opposite trend in chemical shifts is seen for all species once the IL has passed its deliquescence point. After this transition from a solid to a liquid, the IL now has the ability to uptake water and behaviors like other liquid ILs in the presence of water vapor. A detailed discussion on this phenomenon is below.

4.3.4 Chemical Shifts due to Interfacial Water Sorption

Once the IL has deliquesced (liquefied), the BE shift of each species (C 1s, N 1s, and Cl 2p) is drastically different, where the shift now increases with increasing water vapor pressure. To assess the chemical shifting due to uptake of interfacial water, all chemical species were charge corrected to the C_{alkyl} peak at 285.0 eV. This correction was applied due to it being used as a reference in literature and the most hydrophobic species in the IL, meaning water will have the least effect on it.⁷⁰ Once charge corrected, the BE changes of all other species present in the C 1s, N 1s, Cl 2p, and O 1s were assessed as a function of water vapor.

A subset of XPS Cl 2p spectra between 0.25 to 1.15 Torr is shown in Figure 4.13. A dashed line is used to highlight the shift from 0.25 Torr to 1.15 Torr. At 0.25 Torr, the IL is solid and the Cl 2p (3/2) peak is at 197.3 eV. Immediately after deliquescence, the liquid IL shows a Cl 2p (3/2) peak position at 197.5 eV. This is a increase in BE of 0.2 eV. As the water vapor is increased, the BE shift of the Cl 2p (3/2) component continues to increase. At the maximum water vapor pressure of 1.15 Torr, the Cl 2p (3/2) peak position is at 197.7 eV. Overall, the BE shift in the Cl 2p (3/2) component due to water is ~ 0.5 eV.

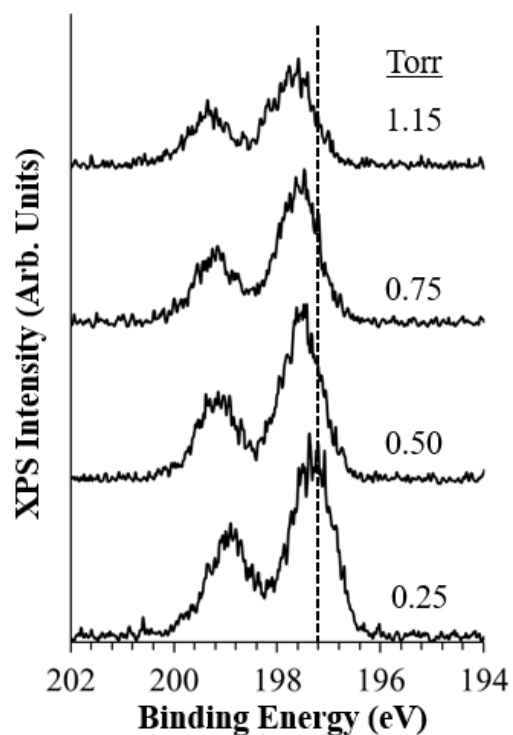


Figure 4.13: Cl 2p spectrum of [C₄mim][Cl] showing chemical shift due to interfacial water uptake.

In addition, the BE shift of all species as a function of water vapor pressure is shown in Figure 4.14. In this figure, all the chemical species experience different magnitude of shifting with water vapor pressure. The largest shift is seen in the Cl 2p (3/2) component. This component is the only representation of the chloride anion. All other species (C_{ox} , C_{ring} , N_{ring}) shift to similar magnitudes that are greater than the C_{alkyl} component. All three of these components represent the imidazolium cation. The O_w component represents the interfacial water within the interfacial region and shifts with the imidazolium cation species. Finally, the C_{alkyl} component (used as a reference), shifts the least. Again, this is expected due to it being the most hydrophobic portion of the imidazolium ionic liquid. Hence, the component to that is the least effected by the presence of water.

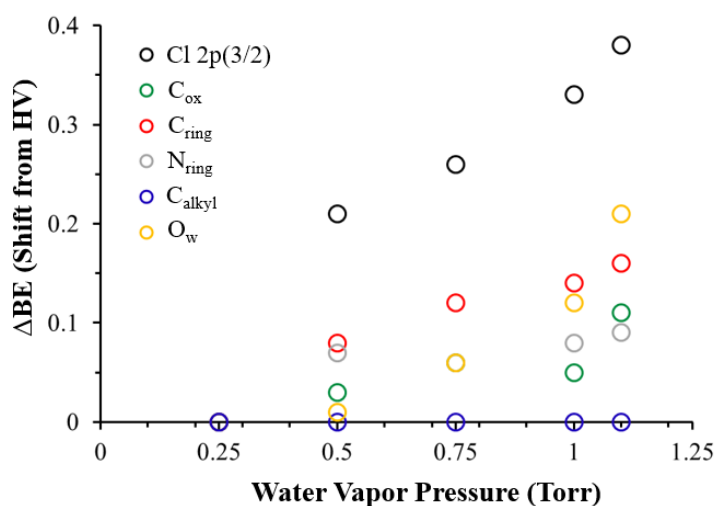


Figure 4.14: Binding energy shifts (ΔBE) of species in $[C_4mim][Cl]$ relative to the spectrum collected at 0.25 Torr as a function of water vapor pressure.

Now instead of the IL shifting due to charge compensation, the chemical species in the IL are shifting to higher binding energy due to its interaction with interfacial water molecules. This phenomenon has been seen in our previous studies of hydrophilic ionic liquid and water.¹¹⁷ Using AP-XPS, we found that the presence of water leads to large BE shifts in the acetate anion and smaller shifts in the imidazolium cation species. The same phenomenon is seen with this hydrophilic IL, [C₄mim][Cl]. Once a liquid, the species present in the IL shift differently with the largest shift in the anion species. The anion is the portion of the IL that interacts the strongest with water molecules. Therefore, it makes sense that this species would have the largest chemical shift as water is added to the system. In addition, the water molecules would then interact with the imidazolium cation. This is represented in shifts in the N_{ring}, C_{ox}, and C_{ring} components. Finally, the most hydrophobic species (C_{alkyl}), will be the species least affected by the presence of water.

In literature, ATR-IR and NMR studies of water and ionic liquid have shown that increasing water concentration leads to shifting in IL species.^{132,133} In these studies, IR well-defined spectral shifts were supported with density functional theory (DFT) calculations to show a direct correlation to hydrogen bond interactions between the IL and water. In an experimental and theoretical study of [C₂mim][Ace] and water, spectral shifts in the OH stretching vibration of water and COO⁻ band of [C₂mim][Ace] with increasing water were seen in experimental ATR-IR data.⁷⁸ To understand these shifts, DFT was used to calculate O-H frequencies of [C₂mim][Ace] and water in different optimized configurations. The DFT results showed that the shifts were larger when the interaction was between the anion-water instead of cation-water, verifying that the anion plays a major role in the IL-water interaction. The DFT

results also confirmed that the hydrogen bonding between acetate anion and water increases with water concentration. In a more recent study of [C₄mim][Ace] and water, DFT calculations were used to assign vibrational modes of the IL and obtain information about the experimental spectral shifts with increasing water concentration.¹³³ In a similarly manner to the previous study, the computational results showed the spectral shifts in the COO⁻ stretching vibrational modes were most likely due to strong hydrogen bond interaction between the acetate anion and water. Experimental IR studies that use DFT to understand spectral shift, as presented above, look at bulk water absorption. On the contrary, the APXPS data shows spectral shifts at the top few nanometers of the IL-vapor interface. In a similar manner to the IR studies, DFT will be used to correlate the APXPS spectral shifts to further confirm the shifting of different species is due to the strength of the interaction of water with both the anion and cation.

4.3.5 Changes in the C 1s Spectra

In addition to chemical shifts in all species as a function of increasing water, changes in the C 1s spectra as a function of increasing water was also apparent. The XPS spectra of a subset of C 1s is shown in Figure 4.15. The bottom spectra at 4.5×10^{-8} Torr shows the C 1s spectrum prior to water exposure while the sample is a solid. The shape of this spectra is expected and represents the 3:4:1 ratio of the C_{alkyl}, C_{ring}, and C_{ox}. The next spectra at 0.5 Torr, is the first C 1s spectrum after the sample deliquesces. In this spectrum, the carbon spectrum is relatively the same as the initial spectrum showing a 3:4:1 ratio of the carbon species in the IL. As the water vapor pressure increases, the carbon spectrum shows changes. At 0.75 Torr, the C_{alkyl} component at the lower binding energy grows. This behavior was seen in the

[C₄mim][Ace] IL with increasing water vapor pressure and has been attributed to structural changes at the interface. However, at the highest water vapor pressure of 1.15 Torr, the carbon spectrum returns back to the original shape.

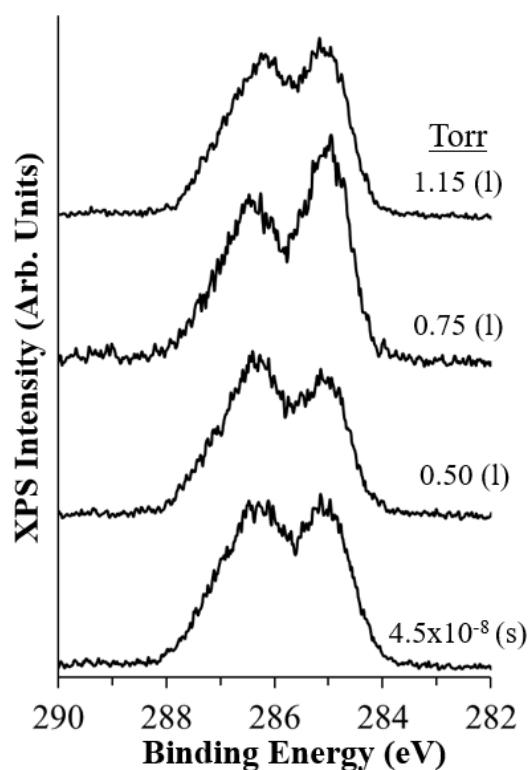


Figure 4.15: C 1s spectrum of [C₄mim][Cl] as a function of water vapor pressure.

To further investigate the change in the C 1s spectra as a function of increasing water, the ratio of aliphatic carbon component (C_{alkyl}) to the total carbon species (C_{Tot}) is plotted in Figure 4.16. While the IL is a solid at pressures from 4.5×10^{-8} Torr to 0.01 Torr, the $C_{\text{alkyl}}:C_{\text{Tot}} \sim 0.49$. Although the sample is still a solid, this ratio is slightly less at pressures of 0.1 and 0.25 Torr at $C_{\text{alkyl}}:C_{\text{Tot}} \sim 0.35$. This change in the

ratio may be due to initial carbon contamination on the surface of the IL while it is a solid. At the initial deliquesce pressure of 0.5 Torr or $n_w:n_{IL} \sim 2$, the $C_{alkyl}:C_{Tot} \sim 0.35$. As the water vapor continues to increase and the number of water molecules around each ionic liquid pair reaches ~ 4 , the ratio of $C_{alkyl}:C_{Tot}$ increases linearly. At the final water vapor pressure of 1.1 Torr, the $C_{alkyl}:C_{Tot} \sim 0.46$.

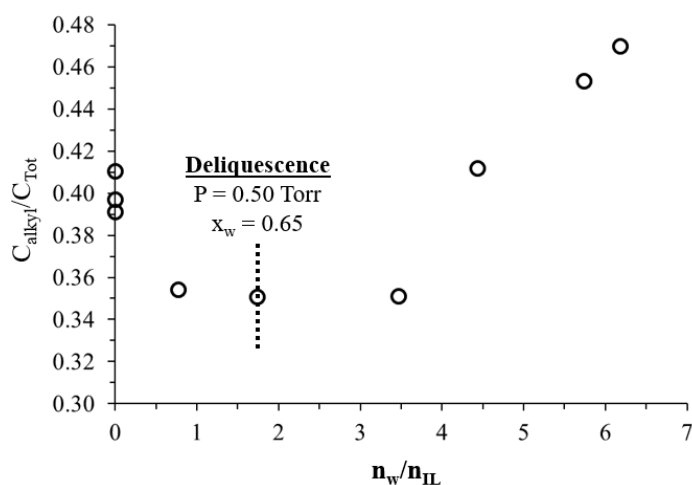


Figure 4.16: Ratio of C_{alkyl}/C_{Tot} as a function of n_w/n_{IL} for $[C_4mim][Cl]$.

This change in the C 1s spectrum has been seen in our previous experiments with $[C_4mim][Ace]$ as a liquid IL and water. The initial drop in the $C_{alkyl}:C_{Tot}$ ratio while the IL is a solid may be due to the desorption of carbon contamination that was on the surface of the solid IL. After deliquescence, the increase of this ratio may be due to restructuring at the IL interface. We believe this restructuring shows the hydrophobic alkyl chain at the outmost surface at the IL-vapor interface while the hydrophilic anion, imidazolium ring, and water molecules are within the interlayer of the interface. To further confirm this, molecular dynamic studies of the interfacial

region are needed. Experimentally, depth profiling of the [C₄mim][Cl] IL and water could also provide insight on the structural of the interface.

Chapter 5

SUMMARY AND FUTURE OUTLOOK

Several capabilities of our custom-built lab-based AP-XPS chamber were shown using both a solid and liquid sample. A solid silver foil was used to test the optimal sample-to-aperture distance to obtain highest XPS signal. In this initial experiment, all three collection modes (angular, transmission, and acceleration) obtained similar optimal sample-to-aperture distances of 560 μm . For all future solid samples, this distance is set by touching the aperture to the sample and moving away in the x direction 560 μm .

The horizontal position of the AP-XPS chamber (which sets it apart from other systems) allows one to study liquid samples including ionic liquids. An attempt at obtaining angle resolved data for water exposure on an IL sample was made. In these experiments, both the angular and acceleration modes were used to determine if an enhancement of water is recognized in the presence of 0.8 Torr at different collection angles. Using the angular collection mode, a flat Au foil with a IL droplet was used and showed no enhancement at either collection angle. The initial experiment using a flat Au foil collected in acceleration mode also showed that tilting the sample between $20^\circ < \Theta < 35^\circ$ did not lead to an enhancement in the water or carbon species. Finally, attempting to physically bend the Au foil along with tilting the sample holder to obtain a more surface sensitive angle of $\Theta = 64^\circ$ did not show an enhancement in the C_{alkyl} or O_w components. For future studies, one can further attempt to bend the Au foil to a

more upright position along with tilting the sample holder. A collection angle of $\Theta = 80^\circ$ is necessary to obtain surface sensitive angle-resolved XPS data.

A QMS MS was also attached to our instrument in two different positions: Stage 0 (high pressure zone) and Stage 2. The performance of this MS was studied in the presence of water vapor at both stages. When the MS is located at Stage 0, the MS reaches its maximum response at a water vapor pressure of 1.00×10^{-4} Torr. The mass spectrometers performance is much better when positioned at Stage 2. At the maximum water vapor pressure of 5.0 Torr, the mass spectrometer detects a maximum pressure of 2.64×10^{-6} Torr at $m/z = 17.94$. When positioned at Stage 2, the mass spectrometer can be used throughout an entire typical experiment conducted using water vapor. Using this mass spectrometer in the presence of water vapor will allow us to study any interesting chemistry that would occur on species with a m/z between 0 and 100 amu.

We studied water uptake of [C₄mim][Ace] using AP-XPS. Interfacial water uptake occurred within 11.0 minutes, which is the time it took to collect the O 1s spectra. Interfacial water uptake is instantaneous compared to gravimetric results that show absorption of water on the order of several hours. Other models have suggested bulk uptake occurs within several hours of exposure.⁸⁵ We also showed the uptake of water into [C₄mim][Ace] was reversible by collecting spectra immediately after pumping water vapor out of the AP-XPS chamber. The addition of water into the interfacial region leads to XPS spectral shifts to higher binding energies for all XPS peaks relative to C_{alkyl}. The magnitude of the binding energy shifts are consistent with stronger water-acetate interactions compared to water-imidazolium cation interactions, driven mainly by hydrogen bonding interactions at the IL-vapor interface. An increase

in the C_{alkyl} signal at $x_w > 0.6$ was observed and is attributed to a water induced structural change that leads to an enhanced concentration of hydrophobic nanostructures in the IL-gas interfacial region.

We have also studied the interfacial water uptake into $[\text{C}_2\text{mim}][\text{BF}_4]$, a more hydrophobic ionic liquid. This sample contained an oxygen contamination that was remained after heating cycles as well as pumping under vacuum for several days. In comparison to $[\text{C}_4\text{mim}][\text{Ace}]$, $[\text{C}_2\text{mim}][\text{BF}_4]$ uptakes approximately half the amount of water at 2.5 Torr. With support from literature, this confirms that this sample is a lot less hydrophilic than other anions. It also sets the standard, for XPS analysis of ILs with water in the lab-based AP-XPS system. The valence band collection of $[\text{C}_2\text{mim}][\text{BF}_4]$ was also collected with and without water. Both spectra showed similar results.

The liquid-vapor interface of water and $[\text{C}_4\text{mim}][\text{Ace}]$ as a function of temperature was studied using AP-XPS. The interfacial water uptake increased with decreasing temperature, with a maximum water mole fraction $x_w = 0.90$ at 0°C . The enthalpy of interfacial water uptake, ΔH , was determined between $0.4 < x_w < 0.85$. At $x_w < 0.7$, there is a favorable dipole-ion interaction between the water and acetate anion. At $x_w > 0.70$, the ΔH for interfacial water uptake approaches the enthalpy of vaporization for bulk water, leading to water-water interactions. Increasing water vapor pressure induced binding energy shifts for each component in all isotherms. A further assessment of the magnitude of these shifts is needed and can be evaluated with DFT core level shift studies. A growth in the C_{alkyl} component at $x_w > 0.6$ may be due to nanostructuring of hydrophilic and hydrophobic components within the interfacial region.

The water uptake into [C₄mim][Ace] using AP-XPS and gravimetric analysis from 0 - 42 °C within RH range of 0 – 56 % was explored. Five isotherms were collected using AP-XPS and three isotherms were collected using gravimetric analysis, where both showed water uptake increased with decreasing temperature. An overlap of RH plots for both AP-XPS and gravimetric isotherms confirmed that water sorption was the only factor contributing to the uptake and within this RH range, and that there is more water in the interfacial region. Further analysis of the thermodynamics of water uptake into IL at both regions showed the enthalpy of sorption, ΔH° was similar from $0.5 < x_w < 0.75$ and more favorable at the interfacial region at $x_w < 0.5$. Both the interfacial and bulk region were initially favorable at low water mole fraction and approached the enthalpy of bulk water as more water was introduced to the system.

The entropy of sorption, ΔS° at the interfacial and bulk regions was also similar at $x_w < 0.55$, and more favorable in the bulk region at $x_w > 0.55$. However, both calculated ΔS° values as a function of water mole fraction were greater than the entropy of bulk water. Using both ΔH° and ΔS° plots, the Gibbs free energy, ΔG° , was determined at 20 °C from $0.4 < x_w < 0.75$. Both the interfacial and bulk ΔG° followed the same trend, where the addition of water led to an increase in ΔG° . Within this x_w range, ΔG° was more favorable at the interfacial range.

The energetics of water uptake into the interfacial region of [C₄mim][Cl] was also determined and compared to the energetics of [C₄mim][Ace] within the interfacial region. While both ILs are considered hydrophilic and had similar uptake curves, the energetics were drastically different. The energetics (ΔH , ΔS , ΔG) were relatively unchanged within $0.4 < x_w < 0.6$ with $\Delta H \sim -36.9 \pm 3.0$ kJ/mol, $\Delta S \sim -68.4 \pm 13.7$

J/mol, $\Delta G \sim -16.9 \pm 1.0$ kJ/mol. The trend may be different due to structural differences at the interfacial regions for the two different ILs. Bulk energetics of water into [C₄mim][Cl] would be a nice compliment to this data and provide additional information on the different trend in energetics.

The deliquescence of several ILs was studied using a saturated salt solution in a controlled environment in order to determine an ideal IL for AP-XPS analysis with water vapor. Of the seven IL that were studied, most of the IL had deliquescence processes that were too rapid to monitor. While other IL studied has deliquescence points with % RH that were too high to monitor in the AP-XPS system. After several IL were studied, the [C₄mim][Cl] IL was chosen for further AP-XPS analysis.

The deliquescence of [C₄mim][Cl] with water vapor at -5 °C was monitored using lab-based AP-XPS. The deliquescence point was determined to be between 7.9 < % RH < 15.8. In order to determine the exact deliquescence point of this IL, more diligent collection of spectra between water pressures of 0.25 and 0.5 Torr are needed. After the deliquescence point, the amount of water uptake increases to a maximum $x_w \sim 0.77$. This water uptake was also reversible.

Similarly to other water uptake experiments, the species in [C₄mim][Cl] did shift with increased water vapor pressure, where the largest shift was seen in the hydrophilic Cl⁻ anion. We also observed changes in the carbon spectra as a function of increasing water vapor pressure. The initial changes in the C 1s spectra may be due to carbon contamination desorbing for the surface of the solid IL. The changes in the carbon spectra as a function of increasing water vapor may be due to restructuring at the interface. This can be confirmed with MD studies of the interfacial region as a

function of water vapor or by conducting depth profiling of the interfacial region using a synchrotron AP-XPS system.

REFERENCES

- (1) Alov, N. Fifty Years of X-Ray Photoelectron Spectroscopy. *Journal of Analytical Chemistry* **2005**, *60*, 297-300.
- (2) Salmeron, M.; Schlögl, R. Ambient Pressure Photoelectron Spectroscopy: A New Tool for Surface Science and Nanotechnology. *Surf. Sci. Rep.* **2008**, *63*, 169-199.
- (3) Watts, John F., Wolstenholme, John., *An Introduction to Surface Analysis by XPS and AES*; J. Wiley: Chichester, West Sussex, England; New York, **2003**, .
- (4) Lovelock, K. R. J.; Villar-Garcia, I. J.; Maier, F.; Steinrück, H. P.; Licence, P. Photoelectron Spectroscopy of Ionic Liquid-Based Interfaces. *Chem. Rev.* **2010**, *110*, 5158-5190.
- (5) Suga, S.; Sekiyama, A., *Photoelectron Spectroscopy*; Springer: **2016**, .
- (6) Lovelock, K. R. J.; Smith, E. F.; Deyko, A.; Villar-Garcia, I. J.; Licence, P.; Jones, R. G. Water Adsorption on a Liquid Surface. *Chem. Commun.* **2007**, *2007*, 4866-4868.
- (7) Arble, C.; Jia, M.; Newberg, J. T. Lab-Based Ambient Pressure X-Ray Photoelectron Spectroscopy from Past to Present. *Surf. Sci. Rep.* **2017**, *submitted*.
- (8) Tao, F. Design of an in-House Ambient Pressure AP-XPS using a Bench-Top X-Ray Source and the Surface Chemistry of Ceria Under Reaction Conditions. *Chem. Commun.* **2012**, *48*, 3812-3814.

- (9) Mangolini, F.; Ahlund, J.; Wabiszewski, G. E.; Adiga, V. P.; Egberts, P.; Streller, F.; Backlund, K.; Karlsson, P. G.; Wannberg, B.; Carpick, R. W. Angle-Resolved Environmental X-Ray Photoelectron Spectroscopy: A New Laboratory Setup for Photoemission Studies at Pressures Up to 0.4 Torr. *Rev. Sci. Instrum.* **2012**, *83*, 093112.
- (10) Moulder, J. F.; Stickle, W. F.; Sobol, P. E.; Bomben, K. D., *Handbook of X-Ray Photoelectron Spectroscopy*; Physical Electronics, Inc.: Eden Prairie, MN, **1995**, 261 pgs.
- (11) C. J. Powell, A. Jablonski NIST Electron Inelastic-Mean-Free-Path Database - Version 1.2, National Institute of Standards and Technology, Gaithersburg, MD, 2010.
- (12) Blundell, R. K.; Delorme, A. E.; Smith, E. F.; Licence, P. An ARXPS and ERXPS Study of Quaternary Ammonium and Phosphonium Ionic Liquids: Utilising a High Energy Ag $L\alpha'$ X-Ray Source. *Phys. Chem. Chem. Phys.* **2016**, *18*, 6122-6131.
- (13) Newberg, J. T.; Åhlund, J.; Arble, C.; Goodwin, C.; Khalifa, Y.; Broderick, A. A Lab-Based Ambient Pressure X-Ray Photoelectron Spectrometer with Exchangeable Analysis Chambers. *Rev. Sci. Instrum.* **2015**, *86*, 085113.
- (14) Andanson, J.; Meng, X.; Traikia, M.; Husson, P. Quantification of the Impact of Water as an Impurity on Standard Physico-Chemical Properties of Ionic Liquids. *J. Chem. Thermodyn.* **2016**, *94*, 169-176.
- (15) Yaghini, N.; Nordstierna, L.; Martinelli, A. Effect of Water on the Transport Properties of Protic and Aprotic Imidazolium Ionic Liquids—an Analysis of Self-Diffusivity, Conductivity, and Proton Exchange Mechanism. *Phys. Chem. Chem. Phys.* **2014**, *16*, 9266-9275.

- (16) Guan, W.; Ma, X.; Li, L.; Tong, J.; Fang, D.; Yang, J. Ionic Parachor and its Application in Acetic Acid Ionic Liquid Homologue 1-Alkyl-3-Methylimidazolium Acetate {[C(N)Mim][OAc](N=2,3,4,5,6)}. *J. Phys. Chem. B* **2011**, *115*, 12915-12920.
- (17) Herrera, C.; García, G.; Alcalde, R.; Atilhan, M.; Aparicio, S. Interfacial Properties of 1-Ethyl-3-Methylimidazolium Glycinate Ionic Liquid regarding CO₂, SO₂ and Water from Molecular Dynamics. *J. Mol. Liq.* **2016**, *220*, 910-917.
- (18) Plechkova, N.; Seddon, K., *Ionic Liquids Uncoiled-Critical Expert Overviews*. Wiley: Hoboken, NJ, **2013**, 413 pgs.
- (19) Gonfa, G.; Bustam, M.; Man, Z.; Mutalib, M. A. Unique Structure and Solute–solvent Interaction in Imidazolium Based Ionic Liquids: A Review. *Asian Trans. Eng.* **2011**, *1*, 24-34.
- (20) Andersson, G.; Ridings, C. Ion Scattering Studies of Molecular Structure at Liquid Surfaces with Applications in Industrial and Biological Systems. *Chem. Rev.* **2014**, *114*, 8361-8387.
- (21) Lei, Z.; Dai, C.; Chen, B. Gas Solubility in Ionic Liquids. *Chem. Rev.* **2014**, *114*, 1289-1326.
- (22) Bhargava, B.; Yasaka, Y.; Klein, M. L. Computational Studies of Room Temperature Ionic Liquid–water Mixtures. *Chem. Commun.* **2011**, *47*, 6228-6241.
- (23) Lovelock, K. R. J. Influence of the Ionic Liquid/Gas Surface on Ionic Liquid Chemistry. *Phys. Chem. Chem. Phys.* **2012**, *14*, 5071-5089.
- (24) Reichelt, M.; Hammer, T.; Morgner, H. Influence of Water on the Surface Structure of 1-Hexyl-3-Methylimidazolium Chloride. *Surf. Sci.* **2011**, *605*, 1402-1411.

- (25) Ridings, C.; Lockett, V.; Andersson, G. Significant Changes of the Charge Distribution at the Surface of an Ionic Liquid due to the Presence of Small Amounts of Water. *Phys. Chem. Chem. Phys.* **2011**, *13*, 21301-21307.
- (26) Deyko, A.; Jones, R. G. Adsorption, Absorption and Desorption of Gases at Liquid Surfaces: Water on [C₈C₁Im][BF₄] and [C₂C₁Im][Tf₂N]. *Faraday Discuss.* **2012**, *154*, 265-288.
- (27) Bubert, H.; Jenett, H., *Surface and Thin Film Analysis: Principles, Instrumentation, Applications*; Wiley-VCH: Weinheim, **2002**, xvii, 336 pgs.
- (28) Baldelli, S. Influence of Water on the Orientation of Cations at the Surface of a Room-Temperature Ionic Liquid: A Sum Frequency Generation Vibrational Spectroscopic Study. *J. Phys. Chem. B* **2003**, *107*, 6148-6152.
- (29) Rivera-Rubero, S.; Baldelli, S. Influence of Water on the Surface of Hydrophilic and Hydrophobic Room-Temperature Ionic Liquids. *J. Am. Chem. Soc.* **2004**, *126*, 11788-11789.
- (30) Sung, J.; Jeon, Y.; Kim, D.; Iwahashi, T.; Iimori, T.; Seki, K.; Ouchi, Y. Air-Liquid Interface of Ionic Liquid Plus H₂O Binary System Studied by Surface Tension Measurement and Sum-Frequency Generation Spectroscopy. *Chem. Phys. Lett.* **2005**, *406*, 495-500.
- (31) Rivera-Rubero, S.; Baldelli, S. Influence of Water on the Surface of the Water-Miscible Ionic Liquid 1-Butyl-3-Methylimidazolium Tetrafluoroborate: A Sum Frequency Generation Analysis. *J. Phys. Chem. B* **2006**, *110*, 15499-15505.
- (32) Deng, G.; Li, X.; Guo, Y.; Liu, S.; Lu, Z.; Guo, Y. Orientation and Structure of Ionic Liquid Cation at Air/[Bmim][BF₄] Aqueous Solution Interface. *Chin. J. Chem. Phys.* **2013**, *26*, 569-575.

(33) Deng, G.; Guo, Y.; Li, X.; Zhang, Z.; Liu, S.; Lu, Z.; Guo, Y. Surface of Room Temperature Ionic Liquid [Bmim][PF₆] Studied by Polarization- and Experimental Configuration-Dependent Sum Frequency Generation Vibrational Spectroscopy. *Sci China Chem.* **2015**, *58*, 439-447.

(34) Saha, A.; SenGupta, S.; Kumar, A.; Choudhury, S.; Naik, P. D. Vibrational Sum-frequency Generation Spectroscopy of Ionic Liquid 1-butyl-3-methylimidazolium Tris (Pentafluoroethyl) Trifluorophosphate at the Air-water Interface. *Chem. Phys.* **2016**, *475*, 14-22.

(35) Deng, G.; Li, X.; Liu, S.; Zhang, Z.; Lu, Z.; Guo, Y. Successive Adsorption of Cations and Anions of Water-1-Butyl-3-Methylimidazolium Methylsulfate Binary Mixtures at the Air-Liquid Interface Studied by Sum Frequency Generation Vibrational Spectroscopy and Surface Tension Measurements. *J. Phys. Chem. C* **2016**, *120*, 12032-12041.

(36) Lauw, Y.; Horne, M. D.; Rodopoulos, T.; Webster, N. A. S.; Minofar, B.; Nelson, A. X-Ray Reflectometry Studies on the Effect of Water on the Surface Structure of [C₄Mpyr][NTf₂] Ionic Liquid. *Phys. Chem. Chem. Phys.* **2009**, *11*, 11507-11514.

(37) Broderick, A.; Khalifa, Y.; Shiflett, M. B.; Newberg, J. T. Water at the Ionic Liquid-Gas Interface Examined by Ambient Pressure X-Ray Photoelectron Spectroscopy. *J. Phys. Chem. C* **2017**, *121*, 7337-7343.

(38) Sloutskin, E.; Lynden-Bell, R. M.; Balasubramanian, S.; Deutsch, M. The Surface Structure of Ionic Liquids: Comparing Simulations with X-Ray Measurements. *J. Chem. Phys.* **2006**, *125*, 174715.

- (39) Penfold, J.; Thomas, R. K. The Application of the Specular Reflection of Neutrons to the Study of Surfaces and Interfaces. *J. Phys. Condens. Matter* **1990**, *2*, 1369-1412.
- (40) Goodchild, I.; Collier, L.; Millar, S. L.; Prokes, I.; Lord, J. C. D.; Butts, C. P.; Bowers, J.; Webster, J. R. P.; Heenan, R. K. Structural Studies of the Phase, Aggregation and Surface Behaviour of 1-Alkyl-3-Methylimidazolium Halide Plus Water Mixtures. *J. Colloid Interface Sci.* **2007**, *307*, 455-468.
- (41) Ohoyama, H.; Teramoto, T. Initial Dissolution of D2O at the Gas-Liquid Interface of the Ionic Liquid C4min]NTf2] Associated with Hydrogen-Bond Network Formation. *Phys. Chem. Chem. Phys.* **2016**, *18*, 28061-28068.
- (42) Gong, X.; Kozbial, A.; Li, L. What Causes Extended Layering of Ionic Liquids on the Mica Surface? *Chem. Sci.* **2015**, *6*, 3478-3482.
- (43) Cui, T.; Lahiri, A.; Carstens, T.; Borisenko, N.; Pulletikurthi, G.; Kuhl, C.; Endres, F. Influence of Water on the Electrified Ionic Liquid/Solid Interface: A Direct Observation of the Transition from a Multilayered Structure to a Double-Layer Structure. *J. Phys. Chem. C* **2016**, *120*, 9341-9349.
- (44) Cheng, H. -.; Dienemann, J. -.; Stock, P.; Merola, C.; Chen, Y. -.; Valtiner, M. The Effect of Water and Confinement on Self-Assembly of Imidazolium Based Ionic Liquids at Mica Interfaces. *Sci. Rep.* **2016**, *6*, 30058.
- (45) Cheng, H.; Stock, P.; Moeremans, B.; Baimpos, T.; Banquy, X.; Renner, F. U.; Valtiner, M. Characterizing the Influence of Water on Charging and Layering at Electrified Ionic-Liquid/Solid Interfaces. *Adv. Mater. Interfaces* **2015**, *2*, 1500159.
- (46) Jurado, L. A.; Kim, H.; Rossi, A.; Arcifa, A.; Schuh, J. K.; Spencer, N. D.; Leal, C.; Ewoldt, R. H.; Espinosa-Marzal, R. M. Effect of the Environmental

Humidity on the Bulk, Interfacial and Nanoconfined Properties of an Ionic Liquid.

Phys. Chem. Chem Phys. **2016**, *18*, 22719-22730.

(47) Wang, Z.; Li, H.; Atkin, R.; Priest, C. Influence of Water on the Interfacial Nanostructure and Wetting of [Rmim][NTf₂] Ionic Liquids at Mica Surfaces. *Langmuir* **2016**, *32*, 8818-8825.

(48) Sakai, K.; Okada, K.; Uka, A.; Misono, T.; Endo, T.; Sasaki, S.; Abe, M.; Sakai, H. Effects of Water on Solvation Layers of Imidazolium-Type Room Temperature Ionic Liquids on Silica and Mica. *Langmuir* **2015**, *31*, 6085-6091.

(49) Begic, S.; Li, H.; Atkin, R.; Hollenkamp, A. F.; Howlett, P. C. A Comparative AFM Study of the Interfacial Nanostructure in Imidazolium Or Pyrrolidinium Ionic Liquid Electrolytes for Zinc Electrochemical Systems. *Phys. Chem. Chem. Phys.* **2016**, *18*, 29337-29347.

(50) Motobayashi, K.; Osawa, M. Potential-Dependent Condensation of Water at the Interface between Ionic Liquid [BMIM][TFSA] and an Au Electrode. *Electrochem. Commun.* **2016**, *65*, 14-17.

(51) Motobayashi, K.; Minami, K.; Nishi, N.; Sakka, T.; Osawa, M. Hysteresis of Potential-Dependent Changes in Ion Density and Structure of an Ionic Liquid on a Gold Electrode: In Situ Observation by Surface-Enhanced Infrared Absorption Spectroscopy. *J. Phys. Chem. Lett.* **2013**, *4*, 3110-3114.

(52) Osawa, M. Dynamic Processes in Electrochemical Reactions Studied by Surface-Enhanced Infrared Absorption Spectroscopy (SEIRAS). *Bull. Chem. Soc. Jpn.* **1997**, *70*, 2861-2880.

(53) Nanbu, N.; Kato, T.; Sasaki, Y.; Kitamura, F. In Situ SEIRAS Study of Room-Temperature Ionic Liquid Vertical Bar Gold Electrode Interphase.

Electrochemistry **2005**, *73*, 610-613.

(54) Lynden-Bell, R.; Kohanoff, J.; Del Popolo, M. Simulation of Interfaces between Room Temperature Ionic Liquids and Other Liquids. *Faraday Discuss.* **2005**, *129*, 57-67.

(55) Picalek, J.; Minofar, B.; Kolafa, J.; Jungwirth, P. Aqueous Solutions of Ionic Liquids: Study of the Solution/Vapor Interface using Molecular Dynamics Simulations. *Phys. Chem. Chem. Phys.* **2008**, *10*, 5765-5775.

(56) Chaban, V. V.; Prezhdo, O. V. Water Phase Diagram is significantly Altered by Imidazolium Ionic Liquid. *J. Phys. Chem. Lett.* **2014**, *5*, 1623-1627.

(57) Lynden-Bell, R. Gas-Liquid Interfaces of Room Temperature Ionic Liquids. *Mol. Phys.* **2003**, *101*, 2625-2633.

(58) Perez-Blanco, M. E.; Maginn, E. J. Molecular Dynamics Simulations of Carbon Dioxide and Water at an Ionic Liquid Interface. *J. Phys. Chem. B* **2011**, *115*, 10488-10499.

(59) Shah, J.; Maginn, E. Monte Carlo Simulations of Gas Solubility in the Ionic Liquid 1-N-Butyl-3-Methylimidazolium Hexafluorophosphate. *J. Phys. Chem. B* **2005**, *109*, 10395-10405.

(60) Aparicio, S.; Atilhan, M. On the Properties of CO₂ and Flue Gas at the Piperazinium-Based Ionic Liquids Interface: A Molecular Dynamics Study. *J. Phys. Chem. C* **2013**, *117*, 15061-15074.

(61) Herrera, C.; García, G.; Atilhan, M.; Aparicio, S. A Molecular Dynamics Study on Aminoacid-Based Ionic Liquids. *J. Mol. Liq.* **2016**, *213*, 201-212.

(62) Feng, G.; Jiang, X.; Qiao, R.; Kornyshev, A. A. Water in Ionic Liquids at Electrified Interfaces: The Anatomy of Electrosorption. *ACS Nano*. **2014**, *8*, 11685-11694.

(63) Dang, L. X.; Wick, C. D. Anion Effects on Interfacial Absorption of Gases in Ionic Liquids. A Molecular Dynamics Study. *J. Phys. Chem. B* **2011**, *115*, 6964-6970.

(64) Dang, L. X.; Chang, T. Molecular Mechanism of Gas Adsorption into Ionic Liquids: A Molecular Dynamics Study. *J. Phys. Chem. Lett.* **2012**, *3*, 175-181.

(65) Chen, Y.; Li, S.; Xue, Z.; Hao, M.; Mu, T. Quantifying the Hydrogen-Bonding Interaction between Cation and Anion of Pure [EMIM][Ac] and Evidencing the Ion Pairs Existence in its Extremely Diluted Water Solution: Via ^{13}C , ^1H , ^{15}N and 2D NMR. *J. Mol. Struct.* **2015**, *1079*, 120-129.

(66) Maki-Arvela, P.; Anugwom, I.; Virtanen, P.; Sjoholm, R.; Mikkola, J. P. Dissolution of Lignocellulosic Materials and its Constituents using Ionic Liquids-A Review. *Ind. Crops Prod.* **2010**, *32*, 175-201.

(67) Zhao, Y.; Liu, X.; Wang, J.; Zhang, S. Insight into the Cosolvent Effect of Cellulose Dissolution in Imidazolium-Based Ionic Liquid Systems. *J. Phys. Chem. B* **2013**, *117*, 9042-9049.

(68) Chen, Y.; Sun, X.; Yan, C.; Cao, Y.; Mu, T. The Dynamic Process of Atmospheric Water Sorption in [EMIM][Ac] and Mixtures of [EMIM][Ac] with Biopolymers and CO₂ capture in these Systems. *J. Phys. Chem. B* **2014**, *118*, 11523-11536.

(69) Stevanovic, S.; Podgorsek, A.; Padua, A. A. H.; Gomes, M. F. C. Effect of Water on the Carbon Dioxide Absorption by 1-Alkyl-3-Methylimidazolium Acetate Ionic Liquids. *J. Phys. Chem. B* **2012**, *116*, 14416-14425.

(70) Hurisso, B. B.; Lovelock, K. R. J.; Licence, P. Amino Acid-Based Ionic Liquids: Using XPS to Probe the Electronic Environment Via Binding Energies. *Phys. Chem. Chem. Phys.* **2011**, *13*, 17737-17748.

(71) Edwards, M. O.; Karlsson, P. G.; Eriksson, S. K.; Hahlin, M.; Siegbahn, H.; Rensmo, H.; Kahk, M.; Villar-Garcia, I. J.; Payne, D. J.; Åhlund, J. Increased Photoelectron Transmission in High-Pressure Photoelectron Spectrometers using "Swift Acceleration". *Nucl. Instrum. Methods Phys. Res. A* **2015**, *785*, 191-196.

(72) Zhang, S., *Ionic Liquids: Physicochemical Properties*; Elsevier: London, **2009**, 478 pgs.

(73) Santos, A. R.; Blundell, R. K.; Licence, P. XPS of Guanidinium Ionic Liquids: A Comparison of Charge Distribution in Nitrogenous Cations. *Phys. Chem. Chem. Phys.* **2015**, *17*, 11839-11847.

(74) Kolbeck, C.; Deyko, A.; Matsuda, T.; Kohler, F. T. U.; Wasserscheid, P.; Maier, F.; Steinrück, H. P. Temperature-Dependent Surface-Enrichment Effects of Imidazolium-Based Ionic Liquids. *Chem. Phys. Chem.* **2013**, *14*, 3726-3730.

(75) McLean, B.; Li, H.; Stefanovic, R.; Wood, R. J.; Webber, G. B.; Ueno, K.; Watanabe, M.; Warr, G. G.; Page, A.; Atkin, R. Nanostructure of [Li(G4)] TFSI and [Li(G4)] NO₃ Solvate Ionic Liquids at HOPG and Au(111) Electrode Interfaces as a Function of Potential. *Phys. Chem. Chem. Phys.* **2015**, *17*, 325-333.

(76) Paynter, R. W. An ARXPS Primer. *J. Electron. Spectrosc. Relat. Phenom.* **2009**, *169*, 1-9.

- (77) Gazitua, M.; Fuentealba, P.; Contreras, R.; Ormazabal-Toledo, R. Lewis Acidity/Basicity Changes in Imidazolium Based Ionic Liquids Brought about by Impurities. *J. Phys. Chem. B* **2015**, *119*, 13160-13166.
- (78) Ding, Z.; Chi, Z.; Gu, W.; Gu, S.; Wang, H. Theoretical and Experimental Investigation of the Interactions between [Emim]Ac and Water Molecules. *J. Mol. Struct.* **2012**, *1015*, 147-155.
- (79) Roohi, H.; Khyrkah, S. Quantum Chemical Studies on Nanostructures of the Hydrated Methylimidazolium-Based Ionic Liquids. *J. Mol. Model.* **2015**, *21*, 1.
- (80) Niazi, A. A.; Rabideau, B. D.; Ismail, A. E. Effects of Water Concentration on the Structural and Diffusion Properties of Imidazolium-Based Ionic Liquid–water Mixtures. *J. Phys. Chem. B* **2013**, *117*, 1378-1388.
- (81) Liu, H.; Sale, K. L.; Simmons, B. A.; Singh, S. Molecular Dynamics Study of Polysaccharides in Binary Solvent Mixtures of an Ionic Liquid and Water. *J. Phys. Chem. B* **2011**, *115*, 10251-10258.
- (82) Ghoshdastidar, D.; Senapati, S. Nanostructural Reorganization Manifests in Sui-Generis Density Trend of Lmidazolium Acetate/Water Binary Mixtures. *J. Phys. Chem. B* **2015**, *119*, 10911-10920.
- (83) Gao, J.; Wagner, N. J. Water Nanocluster Formation in the Ionic Liquid 1-Butyl-3-Methylimidazolium Tetrafluoroborate ([C(4)Mim][BF₄])-D₂O Mixtures. *Langmuir* **2016**, *32*, 5078-5084.
- (84) Zhong, X.; Fan, Z.; Liu, Z.; Cao, D. Local Structure Evolution and its Connection to Thermodynamic and Transport Properties of 1-Butyl-3-Methylimidazolium Tetrafluoroborate and Water Mixtures by Molecular Dynamics Simulations. *J. Phys. Chem. B* **2012**, *116*, 3249-3263.

- (85) Cao, Y.; Chen, Y.; Sun, X.; Zhang, Z.; Mu, T. Water Sorption in Ionic Liquids: Kinetics, Mechanisms and Hydrophilicity. *Phys. Chem. Chem. Phys.* **2012**, *14*, 12252-12262.
- (86) Di Francesco, F.; Calisi, N.; Creatini, M.; Melai, B.; Salvo, P.; Chiappe, C. Water Sorption by Anhydrous Ionic Liquids. *Green Chem.* **2011**, *13*, 1712-1717.
- (87) Chen, Y.; Cao, Y.; Yan, C.; Zhang, Y.; Mu, T. The Dynamic Process of Atmospheric Water Sorption in [BMIM][Ac]: Quantifying Bulk Versus Surface Sorption and Utilizing Atmospheric Water as a Structure Probe. *J. Phys. Chem. B* **2014**, *118*, 6896-6907.
- (88) Zhang, S., *Ionic Liquids : Physicochemical Properties*; Elsevier: Amsterdam, The Netherlands; Boston; London, **2009**, .
- (89) Khalifa, Y.; Broderick, A.; Newberg, J. T. Water Vapor Electron Scattering Cross-Section Measurements using a Hydrophobic Ionic Liquid. *J. Electron Spectrosc. Relat. Phenom.* **2017**, *222*, 162-166.
- (90) Seddon, K.; Stark, A.; Torres, M. Influence of Chloride, Water, and Organic Solvents on the Physical Properties of Ionic Liquids. *Pure Appl. Chem.* **2000**, *72*, 2275-2287.
- (91) Hapiot, P.; Lagrost, C. Electrochemical Reactivity in Room-Temperature Ionic Liquids. *Chem. Rev.* **2008**, *108*, 2238-2264.
- (92) Steinrück, H.; Wasserscheid, P. Ionic Liquids in Catalysis. *Catal. Lett.* **2015**, *145*, 380-397.
- (93) Cao, Y.; Chen, Y.; Lu, L.; Xue, Z.; Mu, T. Water Sorption in Functionalized Ionic Liquids: Kinetics and Intermolecular Interactions. *Ind. Eng. Chem. Res.* **2013**, *52*, 2073-2083.

- (94) Gómez, E.; González, B.; Domínguez, Á; Tojo, E.; Tojo, J. Dynamic Viscosities of a Series of 1-Alkyl-3-Methylimidazolium Chloride Ionic Liquids and their Binary Mixtures with Water at several Temperatures. *J. Chem. Eng. Data* **2006**, *51*, 696-701.
- (95) Jacquemin, J.; Husson, P.; Padua, A.; Majer, V. Density and Viscosity of several Pure and Water-Saturated Ionic Liquids. *Green Chem.* **2006**, *8*, 172-180.
- (96) Gelinas, B.; Rochefort, D. Synthesis and Characterization of an Electroactive Ionic Liquid Based on the Ferrocenylsulfonyl(Trifluoromethylsulfonyl) Imide Anion. *Electrochim. Acta* **2015**, *162*, 36-44.
- (97) Deyko, A.; Lovelock, K. R. J.; Licence, P.; Jones, R. G. The Vapour of Imidazolium-Based Ionic Liquids: A Mass Spectrometry Study. *Phys. Chem. Chem. Phys.* **2011**, *13*, 16841-16850.
- (98) Deyko, A.; Lovelock, K. R. J.; Corfield, J.; Taylor, A. W.; Gooden, P. N.; Villar-Garcia, I. J.; Licence, P.; Jones, R. G.; Krasovskiy, V. G.; Chernikova, E. A., et al., Measuring and Predicting Delta H-Vap(298) Values of Ionic Liquids. *Phys. Chem. Chem. Phys.* **2009**, *11*, 8544-8555.
- (99) Deyko, A.; Hessey, S. G.; Licence, P.; Chernikova, E. A.; Krasovskiy, V. G.; Kustov, L. M.; Jones, R. G. The Enthalpies of Vaporisation of Ionic Liquids: New Measurements and Predictions. *Phys. Chem. Chem. Phys.* **2012**, *14*, 3181-3193.
- (100) Emel'yanenko, V. N.; Verevkin, S. P.; Heintz, A.; Corfield, J.; Deyko, A.; Lovelock, K. R. J.; Licence, P.; Jones, R. G. Pyrrolidinium-Based Ionic Liquids. 1-Butyl-1-Methyl Pyrrolidinium Dicyanoamide: Thermochemical Measurement, Mass Spectrometry, and Ab Initio Calculations. *J. Phys. Chem. B* **2008**, *112*, 11734-11742.

(101) Armstrong, J. P.; Hurst, C.; Jones, R. G.; Licence, P.; Lovelock, K. R. J.; Satterley, C. J.; Villar-Garcia, I. J. Vapourisation of Ionic Liquids. *Phys. Chem. Chem. Phys.* **2007**, *9*, 982-990.

(102) Lovelock, K. R. J.; Armstrong, J. P.; Licence, P.; Jones, R. G. Vaporisation and Thermal Decomposition of Dialkylimidazolium Halide Ion Ionic Liquids. *Phys. Chem. Chem. Phys.* **2014**, *16*, 1339-1353.

(103) Krischok, S.; Eremtchenko, M.; Himmerlich, M.; Lorenz, P.; Uhlig, J.; Neumann, A.; Oettking, R.; Beenken, W. J. D.; Hoeffft, O.; Bahr, S., et al., Temperature-Dependent Electronic and Vibrational Structure of the 1-Ethyl-3-Methylimidazolium Bis(Trifluoromethylsulfonyl)Amide Room-Temperature Ionic Liquid Surface: A Study with XPS, UPS, MIES, and HREELS. *J. Phys. Chem. B* **2007**, *111*, 4801-4806.

(104) Smith, E. F.; Rutten, F. J. M.; Villar-Garcia, I. J.; Briggs, D.; Licence, P. Ionic Liquids in Vacuo: Analysis of Liquid Surfaces using Ultra-High-Vacuum Techniques. *Langmuir* **2006**, *22*, 9386-9392.

(105) Freire, M. G.; Carvalho, P. J.; Gardas, R. L.; Marrucho, I. M.; Santos, L. M. N. B. F.; Coutinho, J. A. P. Mutual Solubilities of Water and the [C(N)Mim][Tf(2)N] Hydrophobic Ionic Liquids. *J. Phys. Chem. B* **2008**, *112*, 1604-1610.

(106) Freire, M. G.; Neves, C. M. S. S.; Carvalho, P. J.; Gardas, R. L.; Fernandes, A. M.; Marrucho, I. M.; Santos, L. M. N. B. F.; Coutinho, J. A. P. Mutual Solubilities of Water and Hydrophobic Ionic Liquids. *J. Phys. Chem. B* **2007**, *111*, 13082-13089.

(107) Ficke, L. E.; Rodriguez, H.; Brennecke, J. F. Heat Capacities and Excess Enthalpies of 1-Ethyl-3-Methylimidazolium-Based Ionic Liquids and Water. *J. Chem. Eng. Data* **2008**, *53*, 2112-2119.

(108) Varfolomeev, M. A.; Khachatryan, A. A.; Akhmadeev, B. S.; Solomonov, B. N.; Yermalayeu, A. V.; Verevkin, S. P. Enthalpies of Solution and Enthalpies of Solvation in Water: The Anion Effect in Ionic Liquids with Common 1-Ethyl-3-Methyl-Imidazolium Cation. *J. Solut. Chem.* **2015**, *44*, 811-823.

(109) Archer, D.; Widegren, J.; Kirklin, D.; Magee, J. Enthalpy of Solution of 1-Octyl-3-Methylimidazolium Tetrafluoroborate in Water and in Aqueous Sodium Fluoride. *J. Chem. Eng. Data* **2005**, *50*, 1484-1491.

(110) Anthony, J.; Maginn, E.; Brennecke, J. Solution Thermodynamics of Imidazolium-Based Ionic Liquids and Water. *J. Phys. Chem. B* **2001**, *105*, 10942-10949.

(111) Takamuku, T.; Kyoshoin, Y.; Shimomura, T.; Kittaka, S.; Yamaguchi, T. Effect of Water on Structure of Hydrophilic Imidazolium-Based Ionic Liquid. *J. Phys. Chem. B* **2009**, *113*, 10817-10824.

(112) Ohno, H.; Fujita, K.; Kohno, Y. Is Seven the Minimum Number of Water Molecules Per Ion Pair for Assured Biological Activity in Ionic Liquid-Water Mixtures? *Phys. Chem. Chem. Phys.* **2015**, *17*, 14454-14460.

(113) Carda-Broch, S.; Berthod, A.; Armstrong, D. Solvent Properties of the 1-Butyl-3-Methylimidazolium Hexafluorophosphate Ionic Liquid. *Anal. Bioanal. Chem.* **2003**, *375*, 191-199.

- (114) Fredlake, C. P.; Crosthwaite, J. M.; Hert, D. G.; Aki, S. N.; Brennecke, J. F. Thermophysical Properties of Imidazolium-Based Ionic Liquids. *J. Chem. Eng. Data* **2004**, *49*, 954-964.
- (115) Yamamuro, O.; Minamimoto, Y.; Inamura, Y.; Hayashi, S.; Hamaguchi, H. Heat Capacity and Glass Transition of an Ionic Liquid 1-Butyl-3-Methylimidazolium Chloride. *Chemical physics letters* **2006**, *423*, 371-375.
- (116) Reinmöller, M.; Ulbrich, A.; Ikari, T.; Preis, J.; Höfft, O.; Endres, F.; Krischok, S.; Beenken, W. J. D. Theoretical Reconstruction and Elementwise Analysis of Photoelectron Spectra for Imidazolium-Based Ionic Liquids. *Phys. Chem. Chem. Phys.* **2011**, *13*, 19526-19533.
- (117) Broderick, A.; Khalifa, Y.; Shiflett, M. B.; Newberg, J. T. Water at the Ionic Liquid–Gas Interface Examined by Ambient Pressure X-Ray Photoelectron Spectroscopy. *J. Phys. Chem. C* **2017**, *121*, 7337-7343.
- (118) Anareddy, R. S.; Shaw, S. K. Long-Range Ordering of Ionic Liquid Fluid Films. *Langmuir* **2016**, *32*, 5147-5154.
- (119) Amith, W. D.; Hettige, J. J.; Castner Jr, E. W.; Margulis, C. J. Structures of Ionic Liquids having both Anionic and Cationic Octyl Tails: Lamellar Vacuum Interface Vs Sponge-Like Bulk Order. *Phys. Chem. Lett.* **2016**, *7*, 3785-3790.
- (120) Martins, M. A.; Neves, C. M.; Kurnia, K. A.; Luís, A.; Santos, L. M.; Freire, M. G.; Pinho, S. P.; Coutinho, J. A. Impact of the Cation Symmetry on the Mutual Solubilities between Water and Imidazolium-Based Ionic Liquids. *Fluid Phase Equilib.* **2014**, *375*, 161-167.
- (121) Freire, M. G.; Neves, C. M. S. S.; Shimizu, K.; Bernardes, C. E. S.; Marrucho, I. M.; Coutinho, J. A. P.; Lopes, J. N. C.; Rebelo, L. P. N. Mutual

Solubility of Water and Structural/Positional Isomers of N-Alkylpyridinium-Based Ionic Liquids. *J. Phys. Chem. B* **2010**, *114*, 15925-15934.

(122) Freire, M. G.; Neves, C. M.; Ventura, S. P.; Pratas, M. J.; Marrucho, I. M.; Oliveira, J.; Coutinho, J. A.; Fernandes, A. M. Solubility of Non-Aromatic Ionic Liquids in Water and Correlation using a QSPR Approach. *Fluid Phase Equilib.* **2010**, *294*, 234-240.

(123) Seo, S.; DeSilva, M. A.; Brennecke, J. F. Physical Properties and CO₂ Reaction Pathway of 1-Ethyl-3-Methylimidazolium Ionic Liquids with Aprotic Heterocyclic Anions. *The Journal of Physical Chemistry B* **2014**, *118*, 14870-14879.

(124) Seo, S.; Quiroz-Guzman, M.; DeSilva, M. A.; Lee, T. B.; Huang, Y.; Goodrich, B. F.; Schneider, W. F.; Brennecke, J. F. Chemically Tunable Ionic Liquids with Aprotic Heterocyclic Anion (AHA) for CO₂ Capture. *J. Phys. Chem. B* **2014**, *118*, 5740-5751.

(125) Newberg, J. T. Surface Thermodynamics and Kinetics of MgO (100) Terrace Site Hydroxylation. *J. Phys. Chem. C* **2014**, *118*, 29187-29195.

(126) Ghosal, S.; Hemminger, J.; Bluhm, H.; Mun, B.; Hebenstreit, E.; Ketteler, G.; Ogletree, D.; Requejo, F.; Salmeron, M. Electron Spectroscopy of Aqueous Solution Interfaces Reveals Surface Enhancement of Halides. *Science* **2005**, *307*, 563-566.

(127) Brown, M. A.; Abbas, Z.; Kleibert, A.; Green, R. G.; Goel, A.; May, S.; Squires, T. M. Determination of Surface Potential and Electrical Double-Layer Structure at the Aqueous Electrolyte-Nanoparticle Interface. *Physical Review X* **2016**, *6*, 011007.

(128) Krisch, M. J.; D'Auria, R.; Brown, M. A.; Tobias, D. J.; Hemminger, J. C.; Ammann, M.; Starr, D. E.; Bluhm, H. The Effect of an Organic Surfactant on the Liquid-Vapor Interface of an Electrolyte Solution. *J. Phys. Chem. C* **2007**, *111*, 13497-13509.

(129) Orlando, F.; Waldner, A.; Bartels-Rausch, T.; Birrer, M.; Kato, S.; Lee, M.; Proff, C.; Huthwelker, T.; Kleibert, A.; van Bokhoven, J. The Environmental Photochemistry of Oxide Surfaces and the Nature of Frozen Salt Solutions: A New in Situ XPS Approach. *Top. Catal.* **2016**, *59*, 591-604.

(130) Cheng, M. H.; Callahan, K. M.; Margarella, A. M.; Tobias, D. J.; Hemminger, J. C.; Bluhm, H.; Krisch, M. J. Ambient Pressure X-Ray Photoelectron Spectroscopy and Molecular Dynamics Simulation Studies of Liquid/Vapor Interfaces of Aqueous NaCl, RbCl, and RbBr Solutions. *J. Phys. Chem. C* **2012**, *116*, 4545-4555.

(131) Seo, S.; Simoni, L. D.; Ma, M.; DeSilva, M. A.; Huang, Y.; Stadtherr, M. A.; Brennecke, J. F. Phase-Change Ionic Liquids for Postcombustion CO₂ Capture. *Energy Fuels* **2014**, *28*, 5968-5977.

(132) MacMillan, A. C.; McIntire, T. M.; Freitas, J. A.; Tobias, D. J.; Nizkorodov, S. A. Interaction of Water Vapor with the Surfaces of Imidazolium-Based Ionic Liquid Nanoparticles and Thin Films. *J. Phys. Chem. B* **2012**, *116*, 11255-11265.

(133) Marekha, B. A.; Bria, M.; Moreau, M.; De Waele, I.; Miannay, F.; Smortsova, Y.; Takamuku, T.; Kalugin, O. N.; Kiselev, M.; Idrissi, A. Intermolecular Interactions in Mixtures of 1-N-Butyl-3-Methylimidazolium Acetate and Water: Insights from IR, Raman, NMR Spectroscopy and Quantum Chemistry Calculations. *J. Mol. Liq.* **2015**, *210*, 227-237.

Appendix A

PERMISSION FOR JOURNAL ARTICLE REPRINT



RightsLink®

Home

Account Info

Help



Title: A lab-based ambient pressure x-ray photoelectron spectrometer with exchangeable analysis chambers
Author: John T. Newberg, John Åhlund, Chris Arble, et al
Publication: Review of Scientific Instruments
Volume/Issue: 86/8
Publisher: AIP Publishing
Date: Aug 1, 2015
Page Count: 8
Rights managed by AIP Publishing.

Logged in as:
Alicia Broderick
University of Delaware

LOGOUT

Order Completed

Thank you for your order.

This Agreement between University of Delaware -- Alicia Broderick ("You") and AIP Publishing ("AIP Publishing") consists of your license details and the terms and conditions provided by AIP Publishing and Copyright Clearance Center.

Your confirmation email will contain your order number for future reference.

[printable details](#)

License Number	4384530871157
License date	Jul 08, 2018
Licensed Content Publisher	AIP Publishing
Licensed Content Publication	Review of Scientific Instruments
Licensed Content Title	A lab-based ambient pressure x-ray photoelectron spectrometer with exchangeable analysis chambers
Licensed Content Author	John T. Newberg, John Åhlund, Chris Arble, et al
Licensed Content Date	Aug 1, 2015
Licensed Content Volume	86
Licensed Content Issue	8
Requestor type	Author (original article)



Title: Water at the Ionic Liquid–Gas Interface Examined by Ambient Pressure X-ray Photoelectron Spectroscopy
Author: Alicia Broderick, Yehia Khalifa, Mark B. Shiflett, et al
Publication: The Journal of Physical Chemistry C
Publisher: American Chemical Society
Date: Apr 1, 2017
Copyright © 2017, American Chemical Society

[LOGIN](#)

If you're a [copyright.com](#) user, you can login to RightsLink using your [copyright.com](#) credentials. Already a [RightsLink](#) user or want to [learn more?](#)

PERMISSION/LICENSE IS GRANTED FOR YOUR ORDER AT NO CHARGE

This type of permission/license, instead of the standard Terms & Conditions, is sent to you because no fee is being charged for your order. Please note the following:

- Permission is granted for your request in both print and electronic formats, and translations.
- If figures and/or tables were requested, they may be adapted or used in part.
- Please print this page for your records and send a copy of it to your publisher/graduate school.
- Appropriate credit for the requested material should be given as follows: "Reprinted (adapted) with permission from (COMPLETE REFERENCE CITATION). Copyright (YEAR) American Chemical Society." Insert appropriate information in place of the capitalized words.
- One-time permission is granted only for the use specified in your request. No additional uses are granted (such as derivative works or other editions). For any other uses, please submit a new request.

[BACK](#)[CLOSE WINDOW](#)

**Book:** Ionic Liquids: Current State and
Future Directions**Chapter:** Water at Ionic Liquid Interfaces**Author:** Alicia Broderick, John T. Newberg**Publisher:** American Chemical Society**Date:** Jan 1, 2017

Copyright © 2017, American Chemical Society

LOGIN

If you're a [copyright.com](#) user, you can login to RightsLink using your [copyright.com](#) credentials. Already a [RightsLink user](#) or want to [learn more?](#)

PERMISSION/LICENSE IS GRANTED FOR YOUR ORDER AT NO CHARGE

This type of permission/license, instead of the standard Terms & Conditions, is sent to you because no fee is being charged for your order. Please note the following:

- Permission is granted for your request in both print and electronic formats, and translations.
- If figures and/or tables were requested, they may be adapted or used in part.
- Please print this page for your records and send a copy of it to your publisher/graduate school.
- Appropriate credit for the requested material should be given as follows: "Reprinted (adapted) with permission from (COMPLETE REFERENCE CITATION). Copyright (YEAR) American Chemical Society." Insert appropriate information in place of the capitalized words.
- One-time permission is granted only for the use specified in your request. No additional uses are granted (such as derivative works or other editions). For any other uses, please submit a new request.

BACK

CLOSE WINDOW